

Scaling laws in thruster physics

INAUGURALDISSERTATION

zur

Erlangung des akademischen Grades eines

doctor rerum naturalium (Dr. rer. nat.)

an der Mathematisch-Naturwissenschaftlichen Fakultät

der

Universität Greifswald

vorgelegt von

Paul Matthias

geboren am 15. Mai 1990

in Greifswald, Deutschland

Greifswald, 11. Januar 2021

Ort, Datum

Dekan:	Prof. Dr. Gerald Kerth
1. Gutachter:	Prof. Dr. Ralf Schneider
2. Gutachter:	Prof. Dr. Mario Merino Martinez
Tag der Disputation:	11. Juni 2021

Abstract

Modern space missions depend more and more on electric propulsion devices for in-space flights. The superior efficiency by ionizing the feedgas and propelling them using electric fields with regard to conventional chemical thrusters makes them a great alternative. To find optimized thruster designs is of high importance for industrial applications. Building new prototypes is very expensive and takes a lot of time. A cheaper alternative is to rely on computer simulations to get a deeper understanding of the underlying physics. In order to gain a realistic simulation the whole system has to be taken into account including the channel and the plume region. Because numerical models have to resolve the smallest time and spatial scales, simulations take up an unfeasible amount of time. Usually a self-similarity scaling scheme is used to greatly speed up these simulations. Until now the limits of this method have not been thoroughly discussed. Therefore, this thesis investigates the limits and the influence of the self-similarity scheme on simulations of ion thrusters. The aim is to validate the self-similarity scaling and to look for application oriented tools to use for thruster design optimization. As a test system the High-Efficiency-Multistage-Plasma thruster (HEMP-T) is considered.

To simulate the HEMP-T a fully kinetic method is necessary. For low-temperature plasmas, as found in the HEMP-T, the Particle-in-Cell (PIC) method has proven to be the best choice. Unfortunately, PIC requires high spatial and temporal resolution and is hence computationally costly. This limits the size of the devices PIC is able to simulate as well as limiting the exploration of a wider design space of different thrusters. The whole system is physically described using the Boltzmann and Maxwell equations. Using these system of equations invariants can be derived. In the past, these invariants were used to derive a self-similarity scaling law, maintaining the exact solution for the plasma volume, which is applicable to ion thrusters and other plasmas. With the aid of the self-similarity scaling scheme the computation cost can be reduced drastically. The drawback of the geometrical scaling of the system is, that the plasma density and therefore the Debye length does not scale. This expands the length at which charge separation occurs in respect to the system size. In this thesis the limits of this scaling are investigated and the influence of the scaling at higher scaling factors is studied. The specific HEMP-T design chosen for these studies is the DP1.

Because the application of scaling laws is limited by the increasing influence of charge separation with increased scaling, PIC simulations still are computationally costly. Another approach to explore a wider design space is given using Multi-Objective-Design-Optimization (MDO). MDO uses different tools to generate optimized thruster designs in a comparatively short amount of time. This new approach is validated using the PIC method. During this

validation the drawback of the MDO surfaces. The MDO calculations are not self-consistent and are based on empirical values of old thruster designs as input parameters, which not necessarily match the new optimized thruster design. By simulating the optimized thruster design with PIC and recalculate the former input parameters, a more realistic thruster design is achieved. This process can be repeated iteratively. The combination of self-consistent PIC simulations with the performance of MDO is a great way to generate optimized thruster designs in a comparatively short amount of time. The proof of concept of such a combination is the pinnacle of this thesis.

Contents

1	Motivation	1
2	Basics	5
2.1	Capacitively coupled radio frequency discharges	5
2.2	The HEMP-T	6
2.3	Scaling of the Boltzmann equation	9
2.4	The Particle-in-Cell Method	13
3	Application of PIC	19
3.1	Simulation of rf discharges	19
3.2	Simulation of HEMP-T	23
3.3	Subsummary	28
4	Similarity scaling-application and limits for HEMP-Ts in PIC	29
4.1	Motivation	29
4.2	Similarity studies in PIC	29
4.3	Subsummary	35
5	Optimization of HEMP-T with PIC and MDO	37
5.1	Multi-Objective-Design-Optimization (MDO)	37
5.2	Validation of optimized HEMP-T	38
5.3	Subsummary	40
6	Conclusions	41
7	Bibliography	43
8	Cumulative thesis articles	47
8.1	[P1] P. Matthias et.al. (2018), Journal of Plasma Physics, 82 (5)	51
8.2	[P2] P. Matthias et.al. (2019), Contributions to Plasma Physics	57
8.3	[P3] S. H. Yeo et.al. (2019), AIAA	77
8.4	[P4] P. Matthias et.al. (2019), Contribution to Plasma Physics	92

9 Declaration	105
10 Curriculum vitae	107
11 Acknowledgement	111

1 Motivation

The launch of the first satellite, the Sputnik I in 1957, was the beginning of a new era for mankind, resulting in outstanding development in the technological and scientific sector. Since then, more and more satellites are used to fulfill the needs of modern life, like GPS [1], TV [2] and telecommunication [3]. The requirements for the engines of the deployed satellites is a high lifetime and high efficiency using the provided fuel. The concept of electric propulsion serves both, representing nowadays the base for modern space missions [4]. To suit a wide variety of space mission profiles, different designs of ion thrusters were developed, such as the High-Efficiency-Multistage-Plasma thrusters (HEMP-T [5]–[7]).

The optimization of ion thrusters is a difficult process and revolves around experimental measurements [6]. Since the construction of new designs is expensive, cheaper methods for optimization are sought-after. Computer based simulations, especially Particle-in-Cell (PIC) models, have proven to be a cheap and useful alternative towards predictive modelling and optimization of ion thrusters [8]. PIC delivers self-consistent solutions for ion thrusters, but because it is a full kinetic model it is limited by the high amount of computing time required to study a specific system. Therefore, it is not suited to explore a wide design space. One of the main problems is that an ion thruster is a rather large system, considering that PIC has to resolve the Debye length, which is of magnitudes smaller than typical ion thruster channel sizes. This results in large computational domains with an unfeasible amount of particles, consuming a lot of computation time to simulate. To reduce the simulation time, different approaches were developed. One of them uses plasma invariants to apply a similarity scaling to the system [9], [10]. This scheme allows to scale down the thruster size while keeping physical properties like plasma density and Debye length equal to the original system. By scaling down the system size, but keeping the Debye length constant, the calculated domain shrinks and hence the computation time decreases significantly. To examine and to study the influence of the similarity scaling scheme on the solution of PIC simulations of ion thrusters is the main focus of this work. This leads to the first main question.

How predictive is PIC, taking into account the approximations that are used, in particular, under similarity scaling schemes? In this thesis the quality of the predictions of PIC simulations is shown by validating the simulation results against experimental measurements. The first part of the validation is done using PIC without the application

of a similarity scaling scheme to simulate a low density plasma in a radio-frequency (rf) discharge [P1]. The results show, that PIC is able to reproduce the high energy ions measured in the experiment, by including an additional surface effect at the electrodes. Like in rf discharges, ion thrusters operate with low density plasmas. Because of the similar plasma properties, the validation resulting from the rf discharge can be applied to ion thruster. Subsequently, PIC is used with the application of the similarity scaling to simulate an ion thruster, the HEMP-T [5], [11]. A qualitative evaluation of the used PIC model is obtained by comparing the development of the thrust in dependency of the applied electrical power with experimental measurements from ion thrusters. After assuring the quality of the used PIC simulation, the effect of the applied similarity scaling on ion thruster simulations is investigated. This is done by studying the simulation of one specific design, the DP1 [12], at different scaling factors. At the example of these simulations the influence of the self-similarity is shown and its limits are discussed [P2]. The results show, that the similarity scaling is a valid approach to reduce the computation time to simulate ion thrusters, but also demonstrate existing limits of this approach.

But even using the similarity scaling, PIC is still not suited to explore a larger design space in a short amount of time. For design optimization, other models have to be considered, leading to the second main question of this thesis.

Which application-oriented tools can be used for design optimization with very short run times? A new approach, using Multi-Objective-Design-Optimization (MDO) for ion thrusters [P4] is introduced, which solves the problem of exploring a wider design space. This approach uses parametric optimization for a simple power balance model with input data from experiment and simulation. Because of the use of a simplified power balance model [13], which contains empirical energy transfer coefficients, the results are not self-consistent. Hence, the speed of the MDO trades off with the physical accuracy due to the lack of self-consistency. This drawback is dampened by validating the optimized thruster design with PIC [P3]. PIC simulations enable the self consistent calculation of the energy transfer coefficients. These can then be fed back into MDO to get a more valid thruster design in terms of self-consistency. This process can then be repeated iteratively until the values of the energy transfer coefficients converge to the desired accuracy. The combination of self-consistent ab initio simulations with the optimization model promises to be a very attractive tool to create optimized thruster designs on a short time scale.

In this thesis these two main questions are answered. At first a short introduction to rf plasmas and HEMP-Ts is given, followed by the derivation of scaling laws in plasma physics, which will later be applied to the PIC simulation. Then, the used PIC method with the applied scaling scheme is described. The main part starts with answering the question, on how predictive PIC modelling is by comparing PIC simulations to two real world

applications. After the verification of the PIC method, the self-similarity scaling scheme is examined by studying its influence on ion thruster simulations using PIC. The second part of this thesis focuses on the presentation of a robust tool to optimize ion thruster designs - the MDO. The results obtained from MDO are then validated and improved using the previously validated PIC method. At last, a short summary of the findings is presented.

2 Basics

In this chapter the necessary basics for this thesis are discussed. First a short overview of radio frequency discharges is given, followed by the explanation of the general HEMP-T concept. The physical description of the processes in the plasma thruster follows. Plasma is mathematically described by the Boltzmann equation, which is here used to derive specific scaling laws. Afterwards the applied PIC method is explained in addition to the used self-similarity scaling scheme.

2.1 Capacitively coupled radio frequency discharges

In industrial plasma applications, for example in plasma coating [14], [15] often capacitively coupled rf (ccrf) discharges are used. The plasma chamber consists basically of a capacity, usually two parallel electrodes, in a vacuum vessel and an inlet for the feed gas. By applying a radio frequency (13.56 MHz) voltage to one of the electrodes and grounding the other, an electric field builds up between the electrodes. The free electrons in the plasma chamber are accelerated and ionize the feed gas, which results in a weakly ionized plasma between the electrodes, with an ionization degree of $10^{-6} - 10^{-4}$. Because of the heavy weight of the ions, they are not able to follow the rapid changes of the electric field and are only affected by the time averaged electric field. Between the electrodes the quasineutral plasma bulk builds up. At the electrodes the plasma sheath builds up, where the potential drops from plasma potential in the bulk to zero at the electrodes (averaged over one rf-cycle), like shown in figure 2.1. Positive ions are accelerated towards the electrode surface by the potential drop, leading to a current onto the electrode. Because the electrodes are capacitively coupled the total plasma current onto the electrodes has to be zero [16]. For symmetric discharges, where both electrodes are equally sized, this results in a total plasma current of zero.

If one of the electrodes has a larger surface than the other one, the total plasma current on the bigger electrode would increase and hence result into a non-zero plasma current. But because the total plasma current on the electrodes has to be zero, a so called self-bias voltage builds up at the smaller electrode [16]. There, an additional negative voltage leads to a raised ion current onto the smaller electrode balancing the plasma current on

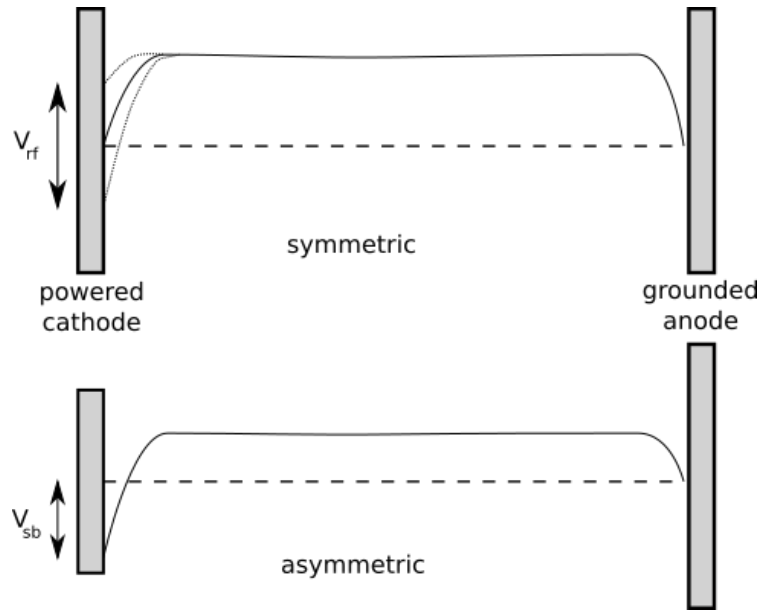


Figure 2.1: Schematic of the time averaged potential in a ccrf discharge at the center of the electrodes for symmetric (top) and asymmetric (bottom) discharges. The dashed lines show the amplitude of the rf power.

the two electrodes. Real experiments are mostly asymmetric because of the influence of the grounded metallic plasma chamber, which acts as an additional grounded electrode.

In the experiment, which will be discussed later in this thesis, an electronegative plasma is used, which occurs with a feed gas like oxygen. oxygen plasmas consist of negative ions in addition to electrons and positive ions. Negative ions are trapped in the plasma bulk like the electrons and usually do not hit the surface of the electrodes, because they are repelled by the sheath potential. These are the most important facts for the following topics about ccrf plasmas.

2.2 The HEMP-T

The High-Efficiency-Multistage-Plasma thruster (HEMP-T) is an electric propulsion device developed and patented by Thales Deutschland GmbH [7]. It belongs to the class of cusped field thrusters. The HEMP-T has the ability to operate at disparate operation points and thus generating different amounts of thrust depending on the mission profile. Due to its design, the thruster can operate efficiently with low erosion at the discharge channel walls, which increases its lifetime.

The nature of HEMP-Ts is sketched in figure 2.2. A HEMP-T consists of a cylindrical discharge chamber, surrounded by several permanent magnet rings with pairwise opposed poles. This induces a cusp-like magnetic field structure in the channel, acting like a magnetic

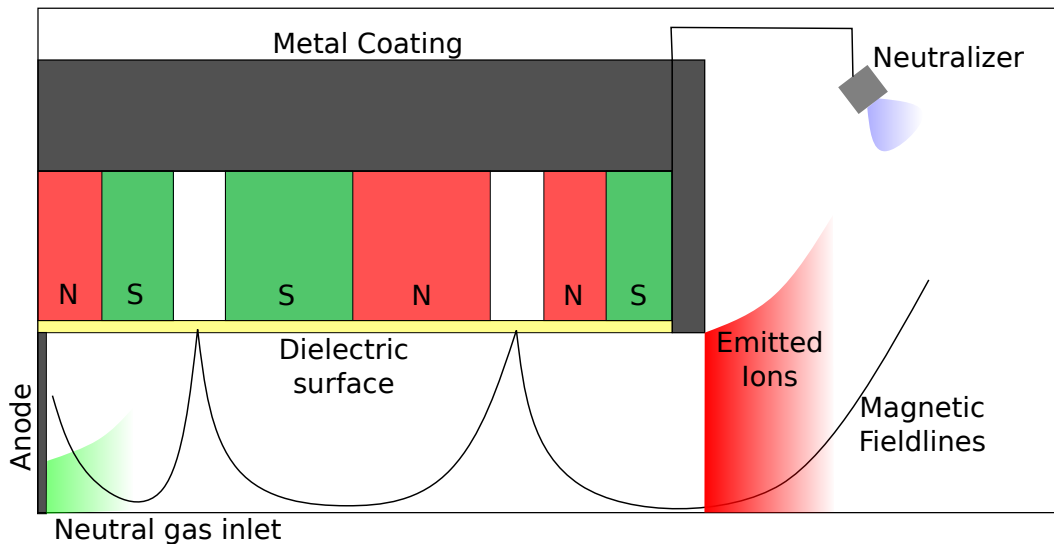


Figure 2.2: Schematic view of the HEMP-T. The cylinder is cut horizontally along the cylinder's axis of symmetry.

mirror. The inside of the chamber is coated with a dielectric with a high sputtering threshold to minimize erosion, for example boron nitride. The anode and the feed gas inlet is located at the bottom of the channel. Usually, xenon is used as feed gas, because of its high mass and its properties as a noble gas. An electron emitting cathode, the neutralizer, is located outside the channel exit, attached to the thruster. It feeds the discharge in the channel and neutralizes the plume. Neutralizing the positively charged exit stream of xenon ions keeps the satellite from charging up with positive charge. The positive potential at the anode leads to a plasma building up in the thruster channel. With sufficient electric conductivity of the plasma the potential drop is moved from the anode to the thruster exit, where the plasma density decreases. This results in an electric field in front of the thruster exit, accelerating the electrons towards the thruster. There, the electrons follow the magnetic field lines provided by the permanent magnets. The resulting gyro radius of the electrons is much smaller than the channel radius, leading to a magnetization of the electrons. As a result of the magnetic field structure, they stay trapped in the thruster channel. The confinement of the electrons leads to high ionization rates. Because of the magnetization of the electrons and the magnetic field line structure between the cusps, the electron transport parallel to the symmetry axis is strong inside the channel. The ions are not magnetized, because of their large mass and the magnetic field strength typical for such thrusters (200 mT), and drift with low energies through the thruster, following the distribution of the electrons. At the exit they are accelerated by the electric field resulting from the potential drop. They are emitted with high emission velocities, thus generating the thrust.

This mode of operation, with high ionization efficiency, high exit velocity of the ions and minimal erosion, makes the HEMP-T a very attractive electric propulsion device. It can generate thrust in a wide range from $1 \mu\text{N}$ – 100mN . The flexibility in providing thrust

in a wide range and the long lifetime as a result of minimal erosion of the thruster, make the HEMP-T a favorable concept for long-term space missions [13]. More information on HEMP-Ts can be found in [5]. What makes the HEMP-T special, is the distinguished magnetic configuration, combining different magnetic mirrors in the cusps. To understand the influence and the behaviour of charged particles in magnetic fields, the physical concepts are investigated.

Dynamics of charged particles in a magnetic field

When a charged particle with the charge q moves through an electromagnetic field, it is affected by the Lorentz force

$$\vec{F} = q\vec{E} + q \cdot \vec{v} \times \vec{B} , \quad (2.1)$$

with the electric field \vec{E} , the particle velocity \vec{v} and the magnetic field \vec{B} . Inside the thruster channel, where the electric field strength is very low, the electron movement is dominated by the magnetic field. In plasma volumes, external electric fields \vec{E} are negligible in comparison to \vec{B} , because of the electric shielding property of plasma. This reduces equation 2.1 to

$$\vec{F} = q \cdot \vec{v} \times \vec{B} , \quad (2.2)$$

which leads to a cycling motion of the particle. The resulting radius r_g is the gyro radius

$$r_g = \frac{mv_{\perp}}{|q|B} , \quad (2.3)$$

with the mass of the particle m and the perpendicular velocity component v_{\perp} in relation to the magnetic field line. The gyro motion depends on the mass of the charged particle, leading to a different gyro radius for electrons and ions. In thruster physics usually the gyro radius of the ions is several times bigger than the system size and therefore they can be assumed unaffected by the magnetic field inside the thruster channel. On the other hand the gyro motion of the electrons along the magnetic field lines is much smaller than the channel dimensions and consequently the electrons follow the magnetic field lines. This magnetization of the electrons is an important transport mechanism in the thruster. If the particle enters regions with higher magnetic fields, the perpendicular velocity increases because of the constant magnetic moment

$$\mu_m = \frac{mv_{\perp}^2}{2B} . \quad (2.4)$$

With no electric field, the particle is situated on the same electric potential, the total energy is constant. This implies that the parallel velocity component v_{\parallel} decreases. As long as the electrons meet the criteria

$$\frac{v_{\perp}}{v} > \sqrt{\frac{B_{min}}{B_{max}}}, \quad (2.5)$$

with the total velocity v and the minimum/maximum magnetic field $B_{min/max}$, they are reflected. This reflection is called the magnetic mirror effect [17].

Inside a HEMP-T the electrons are trapped in the channel between the cusps owing to the magnetic mirror effect. This reduces the wall contact to the regions at the cusps where the magnetic field lines hit the dielectrics. Additionally, it increases the ionization efficiency due to the trapping of the electrons between the cusps and the resulting pendulum motion.

2.3 Scaling of the Boltzmann equation

Numeric simulations of plasma thrusters are time consuming because of the big system size in comparison to the necessary resolution, as will be shown in chapter 2.4. To decrease the computation time it is important to derive scaling laws which allow smaller system sizes. This is done by looking for invariants of the distribution function of the full kinetic characterization of the plasma.

The distribution function of a plasma is given by $f_s(\mathbf{r}_s, \mathbf{v}_s, t)$ for each particles species s . The time evolution of these functions is given by the Boltzmann equation for each species

$$\frac{\partial f_s}{\partial t} + \mathbf{v}_s \frac{\partial f_s}{\partial \mathbf{r}_s} + \frac{\mathbf{F}_s}{m_s} \frac{\partial f_s}{\partial \mathbf{v}_s} = \frac{\partial f}{\partial t} \Big|_{coll}, \quad (2.6)$$

with the force \mathbf{F}_s acting on a particle with the mass m_s and the collision term $\frac{\partial f}{\partial t} \Big|_{coll}$ [18]. The force in electromagnetic systems is the Lorentz force as already described in equation 2.1. In a collisionless plasma, the Boltzmann equation simplifies to the Vlasov equation. The dynamics of a collisionless plasma are then fully described by the combination of the Vlasov and Maxwell equations. The aim is to find invariants of the given set of equations, which can then be used to find possible scaling schemes between two similar systems. System invariants are defined, if all physical parameters can be scaled into each other with corresponding scaling factors. In the case of the Vlasov-Maxwell system this leads to nine scaling constants

between system 1 and system 2 as

$$f_1 = c_f f_2, \quad t_1 = c_t t_2, \quad x_1 = c_x x_2, \quad v_1 = c_v v_2, \quad E_1 = c_E E_2 \quad (2.7)$$

$$B_1 = c_B B_2, \quad q_1 = c_q q_2, \quad m_1 = c_m m_2, \quad c_1 = c_c c_2, \quad (2.8)$$

with the speed of light $c_{1,2}$. The choice of the similarity constants can only be chosen in a way that keeps the equations of motion of the Vlasov-Maxwell system invariant. For example the second term of the Vlasov equation is invariant under scaling if the ratio of the scaling factors is

$$\frac{c_t c_v}{c_x} = 1. \quad (2.9)$$

In a similar fashion four other ratios can be derived as

$$\frac{c_q c_B c_x^2}{c_m c_c c_v |c_x|} = 1, \quad \frac{c_q c_e c_x}{c_m c_v^2} = 1, \quad \frac{c_E |c_v|}{c_q c_f c_v^4 c_x} = 1, \quad \frac{c_B c_c |c_v|}{c_q c_f c_v^5 |c_x|} = 1. \quad (2.10)$$

In the following a constant speed of light is assumed in both systems, setting the scaling constant of the speed of light to $c_c = 1$. The number of independent invariants, which can be derived now, equals the number of relations between the scaling constants. The invariants $C_{1..5}$ follow as

$$C_1 = \frac{qEx}{mv^2}, \quad C_2 = \frac{qBx}{mv}, \quad (2.11)$$

$$C_3 = \frac{mf v^5}{E^2}, \quad C_4 = \frac{mf v^5}{B^2}, \quad (2.12)$$

$$C_5 = \frac{x}{vt}, \quad (2.13)$$

as shown by Lacina et al. [9]. These invariants are applicable for collisionless plasmas. C_1 and C_2 are the invariants of trajectories in the electric and magnetic field. C_3 and C_4 are the invariants of the self induced electric and magnetic fields of the plasma. C_5 describes the similarity of a non stationary process.

When the influence of collisions on the particle distribution function is not negligible, it is necessary to add the collision term to the Boltzmann equation. In this case only binary collisions are considered and applied in the Boltzmann equation. This leads with the same scaling approach as above to another invariant

$$C_6 = \lambda/x, \quad (2.14)$$

with the mean free path λ .

In low temperature plasmas, such as in HEMP-Ts, the internal electric and magnetic fields

are small. The stationary fields lead to a reduction of the invariants, since C_3 and C_4 can be neglected [9]. Of special interest are the invariants C_2 and C_6 , also called the Hall parameter

$$\beta_{Hall} = \frac{r_g}{x} = \frac{m_e v_{e,\perp}}{eBL} = const. \quad (2.15)$$

relating the gyro motion r_g to the system dimensions L and the Knudsen number

$$Kn = \frac{\lambda_s}{x} = \frac{1}{n_n \sigma_{s,n} \langle v_s \rangle L} = const., \quad s \in \{e, i\}, \quad (2.16)$$

relating the mean free path λ_s for different species s to the system dimensions, where $\sigma_{s,n}$ is the collision cross section. Keeping these invariants constant allows the application of diverse scaling approaches.

Following [19], the simplest approach is the scaling of plasma density. The Boltzmann equation is linear in the charged particle densities. Hence, the equation is invariant if the distribution function f_s is divided by a constant factor ξ

$$\frac{\partial f_s / \xi}{\partial t} + \mathbf{v}_s \frac{\partial f_s / \xi}{\partial \mathbf{r}_s} + \frac{\mathbf{F}_s}{m_s} \frac{\partial f_s / \xi}{\partial \mathbf{v}_s} = \frac{\partial f / \xi}{\partial t} \Big|_{coll}. \quad (2.17)$$

As a result of equation 2.17 the solution of the distribution function remains similar for scaled plasma densities in quasineutral regions, because it is only divided with a constant factor. This ensures exact solutions for the plasma volume. With the scaling of the plasma density, the Debye length scales as

$$\lambda_{Db} \propto \sqrt{\xi / n_e}, \quad (2.18)$$

which leads to larger Debye lengths for higher scaling factors. This increases the ratio between Debye length and the constant system size, leading to an expanding charge separation in nonquasineutral regions, e.g., the sheath or the plume of ion thrusters. The expanded charge separation leads to artificial electric fields, which influence the plasma solution. Therefore, the invariance with the scaling of the plasma density is not given for the sheath or other areas with significant space charge. So it shows that the scaling of the plasma density is applicable, as long as the influence of these nonquasineutral areas on the overall solution of the system is negligible.

The scaling of the plasma density is equivalent to a scaling of the vacuum permittivity [20]. This can be easily seen, looking at the Poisson equation

$$\Delta \Phi = \frac{q(\vec{r})}{\epsilon_0 \epsilon_r}, \quad (2.19)$$

with the electrostatic potential Φ , the spatial charge distribution $q(\vec{r})$, the permittivity ϵ_r and the vacuum permittivity ϵ_0 . The scaling of the plasma density is achieved by dividing by the factor ξ

$$\Delta\tilde{\Phi} = \frac{q(\vec{r})}{\epsilon_0\epsilon_r\xi}, \quad (2.20)$$

which is the same as multiplying ϵ_0 with the chosen scaling factor. In later simulations the advantage of this approach is that the nonlinear collision terms do not have to be modified, because the plasma density is not scaled.

Another way to scale the system is by scaling the dimensions of the discharge. To keep particle velocities constant under the scaling law, the time has to be scaled as well. When time and the spatial dimensions are scaled, the magnetic field and the collision operator have to be scaled as well following equation 2.15 and equation 2.16

$$\beta_{Hall} = \frac{\tilde{r}_g}{x/\xi} = \frac{m_e v_{e,\perp}}{e (B\xi) (L/\xi)} = const. \quad (2.21)$$

$$Kn = \frac{\tilde{\lambda}_s}{x/\xi} = \frac{1}{n_n (\sigma_{s,n} \langle v_s \rangle \xi) (L/\xi)} = const., \quad s \in \{e, i\}. \quad (2.22)$$

The scaling on plasma density, vacuum permittivity and dimensions are equivalent, because they all conserve the Hall parameter and the Knudsen number. The various scaling approaches are all derived from the same set of invariants and the solution obtained will be the same. In later simulations the geometric scaling will be implemented, because it is able to reduce the computation time by scaling down the simulation domain.

As an addition it has to be mentioned, that the derived scaling schemes include only binary collisions. If other nonlinear collision terms (like Coulomb collisions) are important, they can be accounted for by modifying the real collision frequencies. But one important limit as shown later in detail is the scaling of the sheath, which is not invariant, because its width is defined by the ratio of Debye length and system size.

Now that the scaling laws are derived, the simulation method necessary to simulate ion thrusters has to be chosen. The electron mean-free paths in HEMP-Ts are of the same size as the system dimensions. Kinetic effects in the magnetic cusps create non-Maxwellian perturbations of the electron distribution function [21]. Hence, a kinetic simulation of the system is necessary for accurate analysis [22], [23]. Commonly, kinetic models like Particle-in-Cell (PIC) are used to simulate low temperature plasmas. PIC simulations deliver self-consistent ab initio solutions and are able to improve the physical insights concerning the physics in

thrusters which are not easily accessible by experiments. Therefore, in the following section the PIC method is described in detail.

2.4 The Particle-in-Cell Method

The Particle-in-Cell (PIC) method is a well-established powerful tool to simulate plasmas. It delivers the exact solution of the collisionless Boltzmann equation. The number of particles in a low temperature plasma is not feasible for computer simulations. In PIC simulations so called super-particles are used instead, each representing a large amount of real physical particles, but keeping the same charge to mass ratio which results in similar trajectories. The super-particle movement is simulated following the scheme in figure 2.3. It was proven that this still gives the exact solution for collisionless plasmas [22].

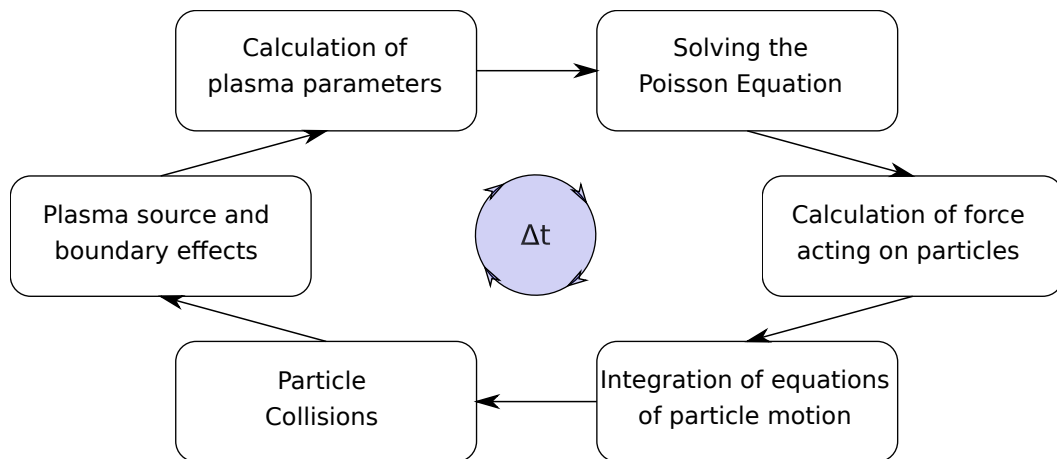


Figure 2.3: Schematic of the PIC cycle.

The electric force on the particle in molecular dynamics is calculated by adding up the interaction force with every other particle, which results in an N^2 problem, where N is the number of particles. This makes the force calculation not feasible for simulations and another approach is used. By putting a grid on the domain and solving the macrofield with the Poisson equation and the given charge distribution, the complexity reduces to $N \log N$ [8]. The calculation domain covers the region of interest. The charge of all super-particles is weighted onto the nearest grid points by applying a Cloud-in-Cell scheme [24], where the particle is given a shape, enabling the weighting according to overlapping areas to the nearest four grid points. In this thesis corrections from plasma currents can be neglected, as the external applied magnetic field in the case of the HEMP-T is of several orders of magnitude bigger than the internal fields, at least in the thruster channel. Hence, only the Poisson equation, as the only field equation in the electrostatic approximation, is solved by applying the five point finite difference scheme for the discrete charge distribution on the grid. The resulting linear equation system is then solved by using the "SuperLU" package

[25]. With the calculated potential the electric force is calculated by weighting the force from the grid points back to the single particles applying the same weighting scheme as before to conserve energy and momentum. Afterwards, the particles are moved using the Boris algorithm [26], an integrator which conserves the phase space volume and thereby provides long term stability. During the particle movement boundary conditions are applied, to simulate surface collisions. This is used to collect surface charge at dielectric boundaries and enabling secondary electron emission and neutral recycling.

The heavier particle species move slower than the electrons and so they do not have to be moved every timestep. Because of this sub-cycling for the ions, the electric field has to be summed up between ion movement steps for consistency. Practicing sub-cycling factors for the ions and neutrals reduces the computation time.

In low density plasmas, the mean free path of the tracked particles is smaller than the corresponding system size, due to additional collisions. The particle collisions, like ionization and elastic collisions, are realized with a Monte-Carlo-Collision model (MCC) [27], [28]. This includes elastic collisions between charged particle species and neutrals, ionization and elastic Coulomb collisions. The different collision processes and cross sections depend on the used feed gas. Additionally, electron-electron Coulomb collisions are included using a binary collision model [29]. All collision processes conserve energy and momentum [30].

With PIC-MCC a better understanding of the basic physics of various systems can be received on microscopic and macroscopic levels. For example, the electrostatic potential and the full distribution functions of all particle species are available. The PIC-MCC method is well discussed in the literature and can be found in several publications [8], [22].

The flip side of PIC is that it has to resolve the smallest scales of the dynamics of the system to be physically correct, namely the electron Debye length in space and the inverse electron plasma frequency in time. One can derive the stability criteria for spatial Δx [31]–[33] and time resolution Δt [22] as

$$\Delta x < \lambda_{Db} \tag{2.23}$$

$$\Delta t < 2\omega_{pe}^{-1}, \tag{2.24}$$

with the Debye length λ_{Db} and the electron plasma frequency ω_{pe} .

Because of the large difference of particle densities in the channel and the plume, the HEMP-T is a multi-scale system with microscopic scales in the discharge channel and macroscopic effects in the plume. This also implies that changes in the ion thruster particle, energy and momentum distributions happen on distinct time and length scales. The changes inside the thruster channel occur on the time scale of the plasma frequency, while the plume

distributions react slower to changes in the channel. If one is interested in the plume region, especially the ion beam characteristics, both channel and plume have to be resolved. These large computational domains increase the computing time. To change the resolution of the grid in the plume region is not applicable, because it would lead to the loss of momentum conservation and gives birth to artificial self forces. One viable solution is to shrink the simulation volume in terms of cell numbers by applying the former introduced scaling laws (equation 2.11) for low temperature plasmas. The reduction is obtained by shrinking the geometry of the thruster to a manageable level, keeping the plasma density constant and scaling the magnetic field strength and collision cross sections, accordingly, to keep the new system similar to the original. Because of the smaller system and the constant Debye length, the simulation domain reduces in terms of cell numbers to a fraction of the original system. In the next part a detailed description of the used implementation of the explained PIC method is given. Additionally, the application of the derived scaling laws to the presented PIC method is shown.

Code Description

The peculiar works of this thesis were all carried out with a 2-dimensional axially symmetric electrostatic PIC code with three dimensions in velocity space and a Monte-Carlo-Collision model [8]. In the case of symmetric ccrf discharges additional one dimensional PIC simulations were applied, with the same velocity space and MCC model. The simulations are electrostatic due to low internal currents, which induce negligible magnetic fields compared to the field applied by the ring magnets in the case of ion thrusters. In the case of the rf plasma the internal currents are even lower and do not influence the discharge. The feed gas for the rf plasma is oxygen and the particle species tracked in the simulation are e^- , O_2 , O^+ and O^- . Because of the extreme high number of neutral particles ($> 10^8$) and their low velocity, they are treated as a constant neutral background and are only considered as collision partners in the rf plasma simulations. The collisions included for oxygen are listed in table 2.1.

Elastic scattering	$e - e \rightarrow e - e$ $O^- + O^- \rightarrow O^- + O^-$ $O_2^+ + O_2^+ \rightarrow O_2^+ + O_2^+$ $e + O_2 \rightarrow e + O_2$ $O^- + O_2 \rightarrow O^- + O_2$ $O_2^+ + O_2 \rightarrow O_2^+ + O_2$
Electron/ion production/loss	
Dissociative recombination	$e + O_2^+ \rightarrow O + O$
Neutralization	$O^- + O_2^+ \rightarrow O + O_2$
Dissociative attachment	$e + O_2 \rightarrow O^- + O_2$
Direct detachment	$O^- + O_2 \rightarrow O + O_2 + e$
Impact ionization	$e + O_2 \rightarrow 2e + O_2^+$
Impact detachment	$e + O^- \rightarrow 2e + O$

Table 2.1: Implemented collisions for oxygen [28]. Cross sections are taken from [34].

For ion thrusters xenon is used as feed gas and the particle species e , Xe , Xe^+ and Xe^{2+} are tracked. The collisions included in this model are direct single and double $e - Xe$ impact ionization, single $e - Xe^+$ impact ionization, integral elastic $Xe^+ - Xe$ collisions (including charge exchange and momentum transfer), as well as integral elastic and inelastic $e - Xe$ collisions. $e - e$ Coulomb collisions are also included. The cross sections for xenon were taken from [35].

In addition to binary particle-particle collisions, boundary effects are applied in the model. Particles leaving the calculation domain are considered outside the region of interest and therefore removed from the simulation. At dielectric and metal walls neutrals are thermally reflected and ions are recycled as thermal neutrals. The charge from the impinging ion is then collected as local surface charge at the dielectric. Electrons are deleted when hitting a metal wall, while causing secondary electron emission (SEE) at dielectrics with a coefficient of 0.5.

In the simulation all variables are scaled with the shortest length scale, the Debye length λ_{Db} , and with time scale, the inverse plasma frequency ω_{pe}^{-1} , to be dimensionless. While providing physically accurate self-consistent solutions, the biggest drawback of PIC simulations are the extensive computing times. To resolve the dynamics from ab initio to an equilibrated state takes seconds in the experiment, but takes millions of time steps in the simulation because of the very small time step ($\approx 10^{-12}s$). To shorten computation time the code is parallelized, splitting the calculation domain in subdomains with respect to keep the particle number. Each subdomain contains the same number of particles and calculates the particle motion and collisions in parallel. This scales down the computing time nearly linear with

Table 2.2: The most important quantities in the PIC simulation with their applied scaling factors. A tilde indicates the quantities of the down scaled system. The similarity scaling factor is ξ .

Quantity	Scaling law
length scale	$\mathbf{x} = \tilde{\mathbf{x}} \xi$
time scale	$t = \tilde{t} \xi$
collision cross section	$\sigma = \tilde{\sigma} \xi^{-1}$
magnetic field strength	$B = \tilde{B} \xi^{-1}$
super particle factor	$N_{sp} = \tilde{N}_{sp} \xi^3$
number density	$n = \tilde{n}$

the number of parallel calculations. But one problem remains, the solution of the Poisson equation. Since the used package "SuperLU" solves the Poisson equation sequentially, it cannot be parallelized. The time for the solver scales linearly with the number of grid points [36], resulting in large computing times for large domains and hence making the simulation unfeasible. One approach to reduce the domain size, and thus the number of grid points, is to use the properties of the Boltzmann equation, especially the invariance under scaling.

Similarity Scaling in PIC

It was already shown in equation 2.17 that the solution of the Boltzmann equation is invariant under the scaling of the system dimensions. With downscaled length scales the computational domain reduces in size and the computation time needed for the simulation decreases. Because the Knudsen number and the Hall parameter have to stay constant, several properties of the simulation model have to be scaled according to table 2.2 [37]. To prove the validity and limits of this similarity scaling is one of the main focuses of this work.

3 Application of PIC

In the previous chapter the basic physics and the chosen simulation model to study low temperature plasmas were discussed. Here, the application of PIC is validated for two experiments. For one, a new occurrence of energetic negative ions in a capacitively coupled radio frequency discharge was measured experimentally, depending on the used anode material [P1]. The results obtained with PIC simulations of the ccrf discharge are used to investigate the behaviour of the high energetic peak in the ion energy distribution function (IEDF).

This is followed by an analysis of the influence of different anode voltages on HEMP-Ts, where similarity scaling is applied in the PIC simulation. All results of the rf study are reported in detail in [P1] and the HEMP-T simulation is given in [11].

3.1 Simulation of rf discharges

Experimental measurements have shown a high energetic peak in the energy distribution function of the negative ions arriving at the anode in an asymmetric electronegative ccrf oxygen discharge [P1]. The basics of the low temperature discharges at hand are discussed in chapter 2 and further details can be found in [16]. The already described PIC model, see section 2.4, in addition with an one dimensional PIC model, is applied to simulate the discharge. In figure 3.1 the simulation domain is shown.

For brevity only the setup of the two dimensional simulation is outlined. The symmetry axis of the cylindrical symmetry of the discharge represents the one dimensional PIC domain. At the left boundary the cathode with a diameter of 3 cm is located. A radio frequency potential is applied to the cathode with a frequency of 13.56 MHz and variable peak to peak potential in a range of 400...1600 V_{pp}. The rest of the domain boundaries are grounded, to resemble the experimental plasma discharge chamber. The grounded anode is located at $z = 6.5$ cm in the 1D simulation and at $z = 2.5$ cm in the 2D simulation with a diameter of 4.5 cm. Oxygen is used as feed gas and electrons, neutrals O_2 , positive ions O^+ and negative ions O^- are tracked.

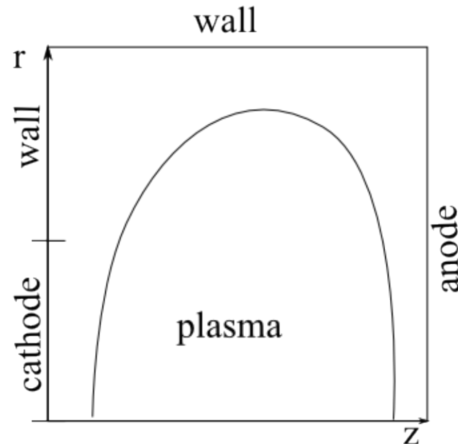


Figure 3.1: Simulation domain for the radio frequency discharge. The one dimensional PIC model represents the symmetry (z) axis of the two dimensional PIC model.

As already explained, a self-bias voltage builds up at the cathode of the experiment, because of the asymmetry of the electrodes. The self-bias potential is applied artificially in the simulation, because the time-scale for building up a self-consistent self-bias is not reasonable. In this low pressure discharge the ionization rate is very low, leading to the neutral gas density to be magnitudes higher (10^{15} cm^{-3}) than the charged particle densities (10^9 cm^{-3}). Hence, it can be assumed that the discharge has a negligible influence on the neutral gas distribution. To speed up the simulation the neutral dynamics were not resolved, but a constant neutral background distribution was applied. The other simulation parameters are stated in [P1].

The experiment predicts surface effects to be responsible for the high energy peak in the ion energy distribution function (IEDF) of the negative ions arriving at the anode. To support this idea, an additional surface material effect was added to the simulation, namely secondary ion emission (SIE). In theory the Saha equation for negative ions describes the emission probability of negative ions at a charged surface, when a neutral particle hits the surface. But there are no theoretical and experimental studies available for the reflection coefficients of negative ions, which are necessary for the Saha equation. It is assumed that the negative self bias voltage at the cathode enables the production of negative oxygen ions at the surface of the cathode. Because of the the missing data and the constant neutral background, no neutrals hit the surface of the anode and cannot produce negative ions. Instead a percentage of the positive ions hitting the anode are reemitted as thermal negative ions. This rate is determined empirically by varying the rate at which negative ions are emitted. Following this approach it is possible to simulate the effect of secondary ion emission.

For symmetric ccrf discharges it is sufficient to use one dimensional PIC simulations, which need less computing time than two dimensional simulations. Because of the axis symmetry

of a one dimensional simulation, there is no self-bias voltage at the anode. Nevertheless, to study the behaviour of negative ions, which might be produced at the anode, SIE is applied to the anode, despite the absence of a self-bias voltage. With the effect of secondary ion emission from the anode, additional structures in the IEDF occur, especially in the one dimensional PIC simulation, as shown in figure 3.2. There, the energy distribution of the negative oxygen ions O^- is shown, where negative energies represent negative velocities (in $-x(z)$ direction). It can be seen, that the emitted ions are accelerated by the sheath potential until they reach the energy equivalent to the plasma potential. They cross the bulk and are then reflected by the sheath at the anode. This leads to the high density peak of the high energy ions in the plasma bulk. Additionally, lower energy levels of the energy distribution of O^- are filled because of the cooling urging from elastic collisions of O^- with neutral molecules O_2 [P1].

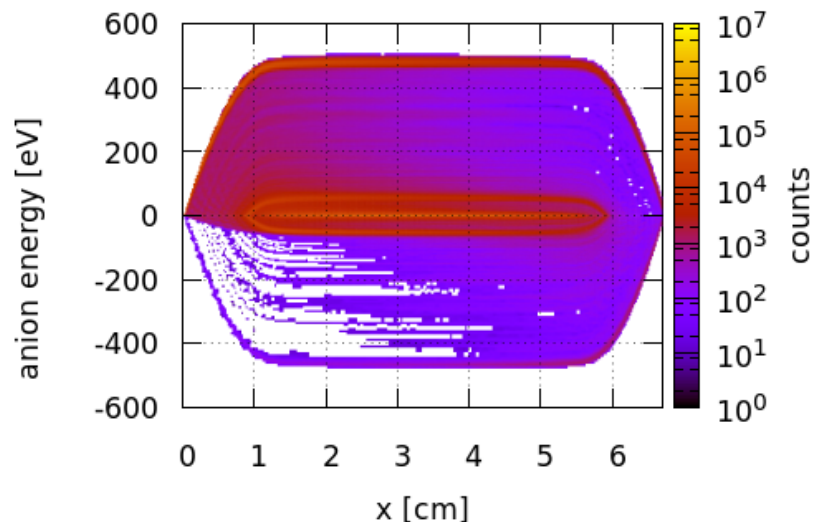


Figure 3.2: Negative ion axial energy distribution function of oxygen at 5 Pa and a driver voltage of 800 V_{pp} in a 1D PIC simulation [P1].

However, no negative ions impinge at the anode surface in the one dimensional simulation because the negative ions are trapped in the symmetric potential. In the experiment a self-bias voltage builds up at the cathode, due to the asymmetry of the electrodes and the capacitive coupling. This cannot be realized in a one dimensional simulation, because the electrodes are zero dimensional objects and therefore by definition the simulation is symmetric. To realize different sized electrodes, at least two dimensional simulations are needed. The asymmetry would then enable to collect charge on the cathode and the self-consistent build up of a self-bias voltage. This is artificially done by subtracting an estimated self-bias voltage of the applied rf potential.

Further simulations with a two dimensional simulation lead to measurable IEDFs at the

anode. Comparing these at various driver voltages with experimental measured IEDFs, as shown in figure 3.3, the same qualitative behaviour can be found. The applied secondary ion emission leads to comparable high energy peaks in the IEDF of the negative ions O^- . Additionally, the density plateau at lower energies can be reproduced by the simulation. It can be shown that this plateau consists of secondary ions and negative ions, which are born in the sheath. After elastic collisions with the neutral background, they populate the lower energy levels. This was also shown in [P1].

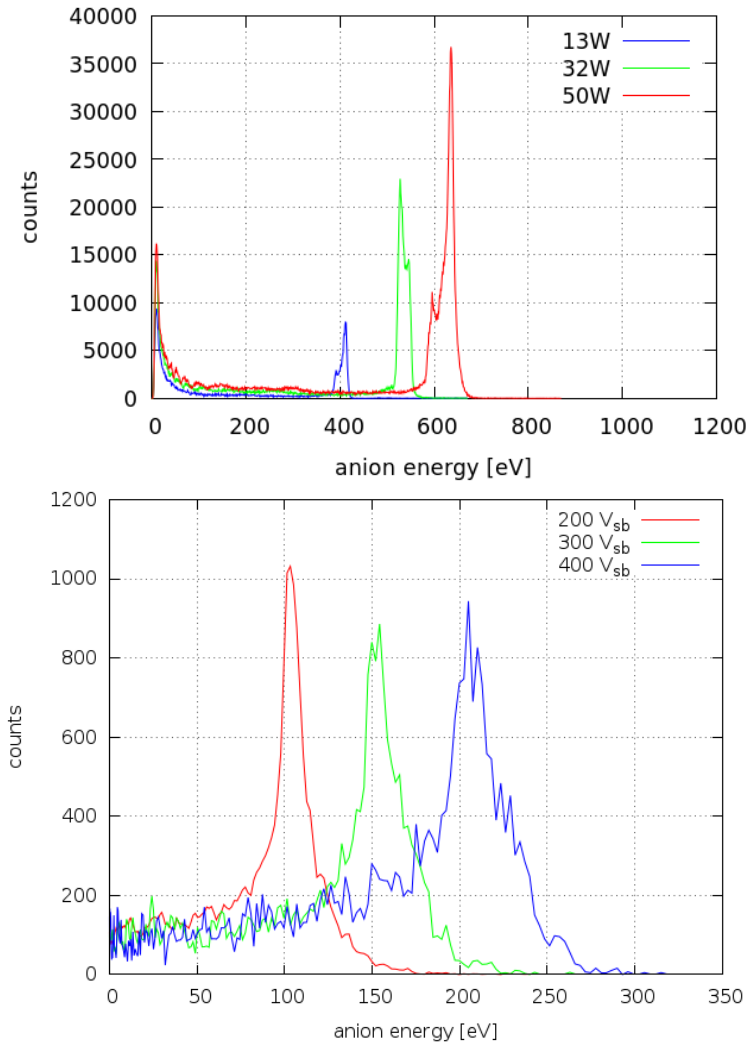


Figure 3.3: Comparison of (bottom) 2D PIC simulation IEDFs of negative oxygen ions with (top) the experiment [P1].

But the simulated and experimentally measured data also differ. One explanation is the applied SIE. With the correct application of the Saha equation, using experimentally measured reaction rates, the amount of high energy ions would be closer to experimental measurements. Another approximation used here is the constant neutral background. By simulating the full kinetics of the neutrals changes in the neutral distribution generated by the elastic collisions with the high energy negative ions might lead to additional effects, which could not be observed in this simulation. The problem is the relatively large system size, which

leads to a large number of particles which have to be simulated. This increases the computation time extensively. Another problem is the non self-consistent application of the self-bias potential. Because PIC has to resolve the plasma frequency for physical stability the self-consistent build up of the self-bias voltage would take extensive computation time, too. Despite these errors, PIC is able to simulate the ccrf discharge given by the experiment and deliver a better understanding of how the high energy ions behave in the discharge. The hypothesis of surface ions being responsible for the high energy peak in the negative IEDF could be supported by the distribution functions obtained by the PIC simulation. This shows that PIC is a robust tool to simulate low temperature plasmas to provide in depth physics information.

3.2 Simulation of HEMP-T

PIC simulations are also applied to simulate electric propulsion devices, see [8], [37]. One ion thruster, the DM3a, constructed by THALES Deutschland GmbH [5], [6], provides several data to compare the simulation results with. The validity of the simulation is supported by a scan of operation parameters of the DM3a. The results are compared to the experiment and show computing limits of the PIC simulation.

First, the implementation of the HEMP-T in the PIC model is presented. Because of the cylindrical symmetry of the HEMP-T, the simulation uses cylindrical coordinates (r, z) . The simulation domain covers the channel and the near exit region. The dynamics of electrons e^- , neutrals Xe, singly charged ions Xe^+ and doubly charged ions Xe^{2+} are resolved. In HEMP-Ts the density of doubly charged ions is only a small fraction ($\approx 10\%$) of the singly charged ions. The density of higher charged xenon ions is only $< 1\%$ [6] of the singly charged ions and are hence neglected in the simulation. In this model direct single and double e^- -Xe impact ionization, single e^- - Xe^+ impact ionization, integral elastic Xe^+ -Xe collisions (including charge exchange and momentum transfer), and integral elastic and inelastic e^- -Xe collisions [21] are included. In figure 3.4 the applied boundaries can be seen. At the left domain boundary ($z=0$) the anode potential is applied. The top domain boundary is at ground potential and the right domain boundary is set to a fixed electric field gradient of 0 to simulate an open boundary towards the vacuum. The grey box in the left upper corner is the dielectric, which covers the magnets. At the thruster exit a grounded metal pole piece is applied, visualized by the red box in the figure. Further details about the applied boundary conditions can be extracted from the respective publications [11].

One of the big advantages of the HEMP-T is the wide operational range. The lower limit of the anode voltage is given by the necessary energy to sustain the ionization for the

discharge. Accordingly, the upper limit is given by technical constraints, such as the limit of the power supplies and insulation limits to avoid arcs. To understand the physical processes in thrusters mainly PIC simulations are used [38]. Because the DM3a thruster is the subject to plenty of experimental studies [6], [39]–[43], it is a good system to validate PIC. The aim here is to validate the application of PIC, by analyzing the development of the thrust with the applied anode voltage.

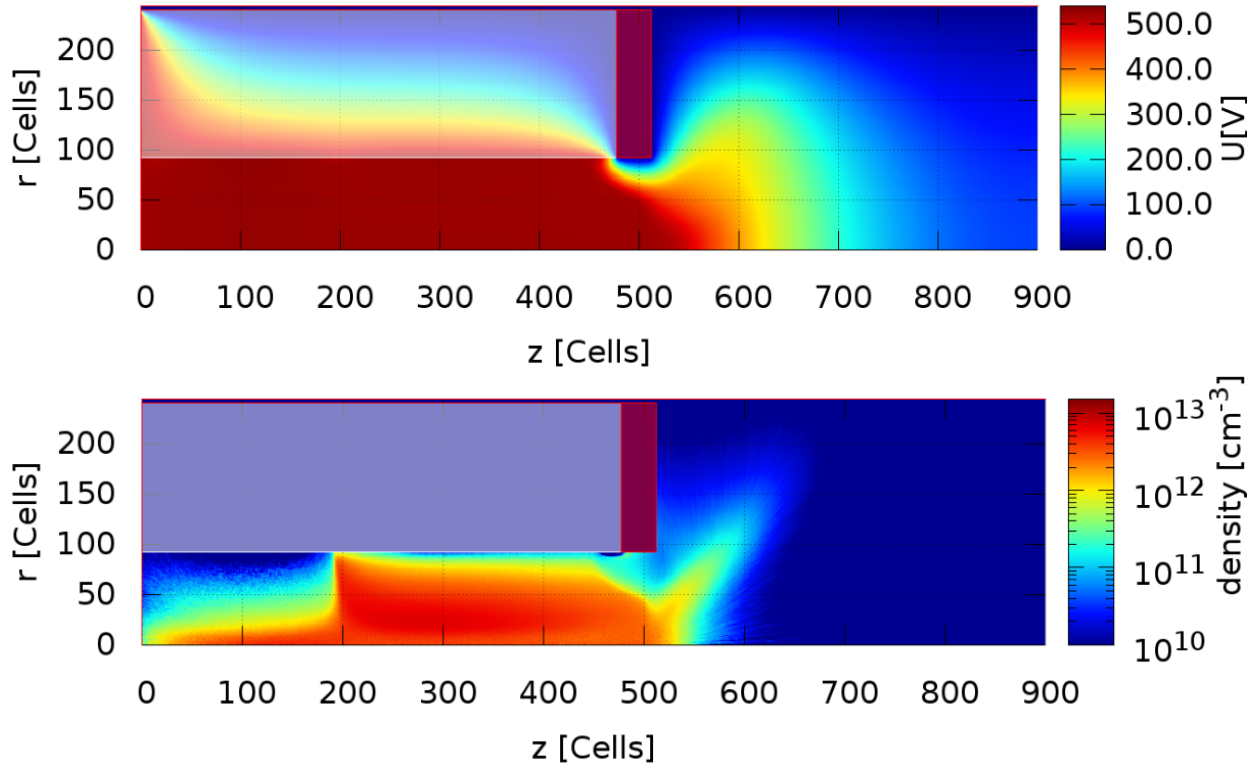


Figure 3.4: (Top) Potential and (bottom) Xe^+ density distribution in the Dm3a thruster with an applied anode voltage of 500 V [11].

In figure 3.4 the potential and the ion density distribution in the simulation is shown. In this case the applied cathode voltage was 500 V. The neutral gas inlet at the anode center inserts xenon with a flow rate of 12 sccm. The electrons for the plasma discharge are supplied by the neutralizer electron source located in the exit area at $r = 2$ cm and $z = 7$ cm. They are then magnetized by the strong magnetic field in the thruster channel and ionize the neutrals. The strong axial transport of the electrons along the magnetic field lines in between the cusps leads to a flat potential in the channel. At the exit the potential drops to vacuum potential, generating a high electric field. The drifting ions are accelerated at the exit by the electric field to the energy of the anode potential and emitted from the thruster, see figure 3.4, generating the thrust.

Diverse operation states are realized by varying the anode voltage and keeping the rest of the parameters constant. The position of the electron source influences the solution of the plasma [44], which limits the applicable range of anode voltages, before the system gets

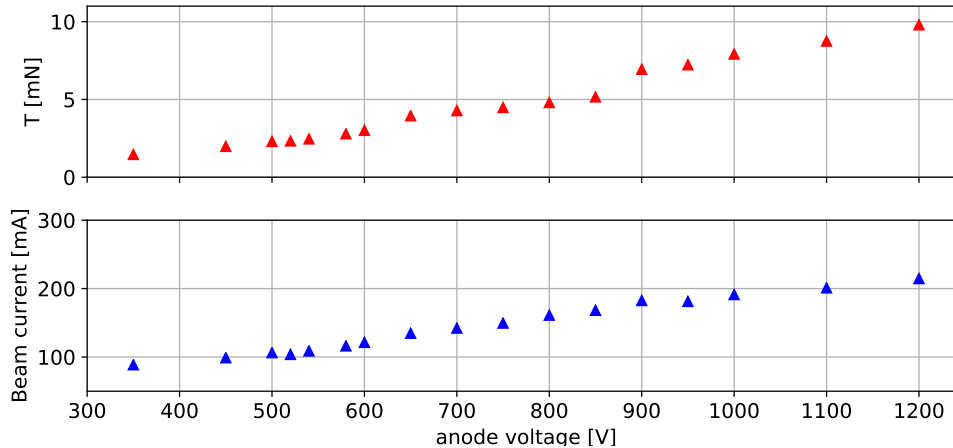


Figure 3.5: Development of the (top) thrust and the (bottom) beam current of the Dm3a in dependency of the anode voltage.

numerically unstable. In [11] the voltage was varied in a range of 350-520 V. To extend the upper limit of the applicable anode voltage the electron source is relocated to the axis near the exit at $r = 0 - 0.5$ cm and $z = 6$ cm. By putting the electron source closer to the channel, the energy of the electrons reaching the thruster channel is reduced. This leads to less ionization, but now it is possible to apply higher anode voltages without producing numerical instabilities. The anode voltage was varied in the range from 350...1200 V with the new electron source.

In figure 3.5 it is shown, that the thrust rises with increasing anode voltage. This is explained by looking at the thrust calculation

$$T = v \cdot \dot{m} \cdot \cos(\alpha_{emission}) , \quad (3.1)$$

with the mass flow \dot{m} , the ion velocity v and the mean emission angle $\alpha_{emission}$. Assuming the energy of the ions is at anode voltage potential when they leave the thruster, the velocity can be replaced with $v^2 = 2q_i U / m_i$. To take into account the beam divergence, the velocity is reduced to its axial component by multiplying with $\cos(\alpha_{emission})$. The emission angle is assumed constant over the variation of the voltage. This is only an approximation, because higher voltages lead to stronger ionization and a larger plasma bulk, which extends toward the exit of the thruster. As a consequence the radial potential gradient increases, which accelerates ions in radial direction and hence increasing the emission angle. Here, the focus is on the influence of the anode voltage onto the thrust. The mass flow for small timesteps is dM_i/dt , with $M_i = \sum_n m_i$ the total ion mass leaving the thruster. The number of ions leaving the thruster n is also given by the beam current $n = I_B * dt / q_i$. Inserting these

terms into equation 3.1 leads to

$$T = \underbrace{\sqrt{\frac{2m_i}{q_i}} \cos(\alpha_{emission})}_{const.} \cdot I_B \sqrt{U_a} , \quad (3.2)$$

$$T \sim I_B \sqrt{U_a} . \quad (3.3)$$

This leads to a square root dependency of the thrust to the anode voltage, which is different to the linear dependency shown in figure 3.5. The linear dependency can be explained by taking the increasing beam current, like shown in figure 3.5, into account. Rescaling equation 3.3 to the product $I_B \sqrt{U_a}$ leads to the expected linear dependency.

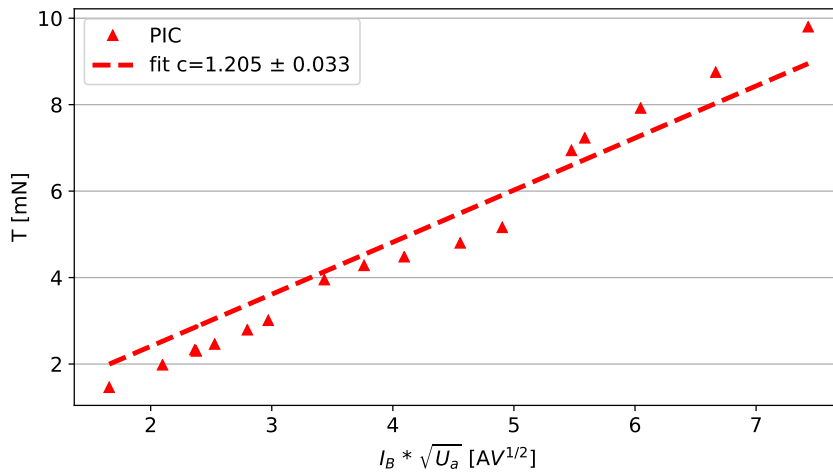


Figure 3.6: Development of the thrust of the Dm3a in dependency of the product of anode voltage and beam current. The dashed line represents the linear fit.

The according data and fit function is shown in figure 3.6. The higher beam current is explained as a result of a higher potential drop at the exit. The electrons get more energy by the electric field and this leads to higher ionization and to higher plasma densities in the channel, even if the electron source is located close to the channel. Together with the higher electric field to accelerate the ions, the thrust rises. A similar behaviour can be observed in the experiments [42]. It is shown for three HEMP models that the thrust efficiency increases with rising anode voltage. Because the mass flow rate of the neutral inlet was constant with the rising anode voltage in [42], this is the same statement as the thrust increases with rising anode voltage.

The full kinetic information of PIC enables detailed studies of distribution functions of the plasma species. In [11] the ratio of doubly to singly charged ions and their respective contribution to the thrust were also analyzed. The contribution of the doubly charged ions raises nonlinear with rising anode voltage.

This behaviour is explained by calculating the radial mean values $r_{mean}(z)$ and moments

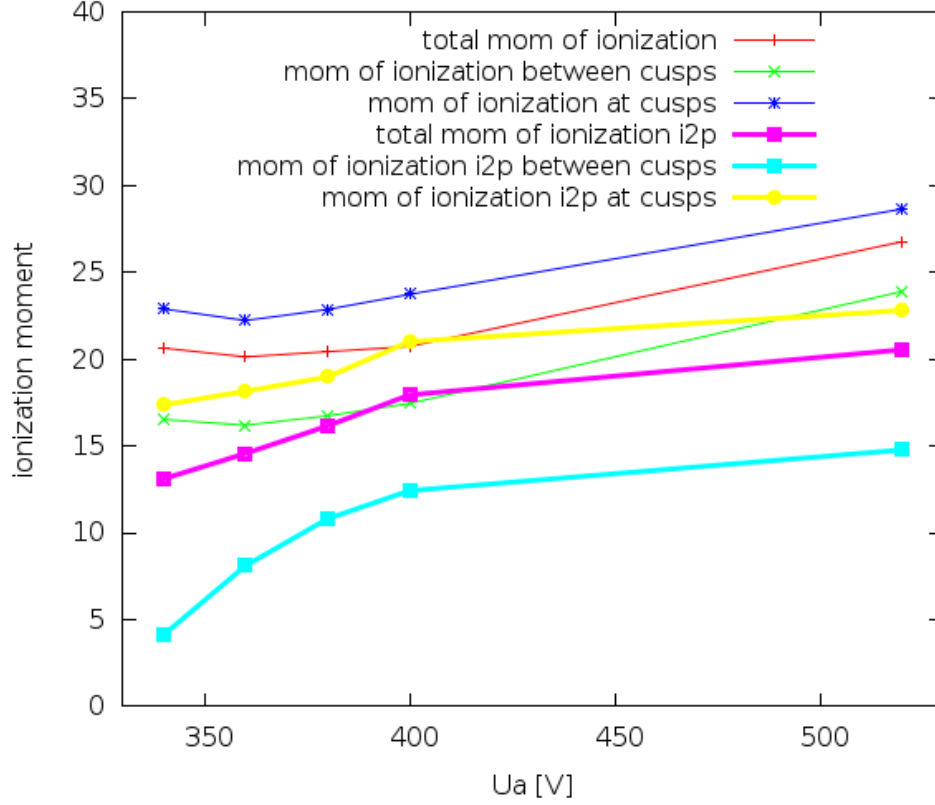


Figure 3.7: Ionization weighted mean values as defined in equation 3.5 for distinct areas inside the thruster channel for single and double ionization processes over the applied anode voltage [11].

$r_{mean,total}$ of ionization as

$$r_{mean}(z) = \frac{\int r * n_{ionization}(r, z) dr}{\int n_{ionization}(r, z) dr}, \quad (3.4)$$

$$r_{mean,total} = \frac{\int r_{mean}(z) * (\int n_{ionization}(r, z) dr) dz}{\int \int n_{ionization}(r, z) dr dz}, \quad (3.5)$$

where $n_{ionization}(r, z)$ is the number of ionization processes. The results in figure 3.7 show, that the mean ionization areas of doubly charged ions are closer to the axis then the ones from the singly charged ions. Ions produced further away from the axis receive a higher radial velocity due to the potential structure at the exit. As a result their contribution to the thrust is lower.

In this simulation the lower limit of applicable anode voltages is 350 V. Below this anode voltage the energy is not sufficient to maintain a stable plasma in the channel. Applying a higher voltage, the charged particle numbers grow due to higher ionization. The surging amount of particles, which have to be tracked for charge deposition and collisions, extend the computation time of the simulation. Above 1200 V the computation time grows considerably, which is the reason for the limited range of the applied anode voltage. By practicing methods

to reduce the system size, like self-similarity scaling, the computation time can be reduced, enabling the studies of higher anode voltages. In this simulation, similarity scaling has already been applied, with the scaling factor $\xi = 10$.

3.3 Subsummary

In this chapter PIC simulations were carried out for two distinct systems (ccrf discharge and ion thruster) and then partially compared to experimental measurements. The PIC simulation of the ccrf discharge was able to expand the understanding of the secondary ion emission in asymmetric discharges. Additionally, the results obtained for simulating the HEMP-T using PIC at different anode voltages showed the expected increase in thrust. The simulations have shown the same qualitative behaviour, like the responding real life systems, while providing a deep physical insight into the systems with the full kinetic information obtained. This shows that PIC simulations are a consistent and robust tool to investigate low temperature plasmas. Still, the PIC model is limited by its large amount of computing time it takes to reach a steady state in the simulated systems. As the system size expands the computation time grows massively. By applying scaling laws this computing time can be reduced to a fraction. The limits of the application of the similarity scaling are discussed in the next chapter.

4 Similarity scaling-application and limits for HEMP-Ts in PIC

In the previous chapter the used PIC model was validated. It has been shown that it is a valuable tool to deliver physically accurate descriptions of ion thrusters. Here, the application of the self-similarity scaling scheme, as discussed in section 2.3, will be investigated. First the scaling scheme will be validated at the example of one specific HEMP-T design, by applying small scaling factors and studying the influence of the scaling. After the validation, an in-depth study will be shown for larger scaling factors. The appearing changes are then explained with the influences of the similarity scaling and at last the limits of the scheme are shown.

4.1 Motivation

To speed up the computation of PIC simulations of ion thrusters similarity scaling schemes are used among other methods. Studies have been carried out onto the effects of similarity scaling for Hall thruster by Taccogna et. al. [10]. But these studies focused on the channel solution only. The effect on the plume and the nonlinear coupling between plume and channel have not been investigated, yet. To understand the influence of the similarity scaling on HEMP-Ts and show the limit is the aim of the following chapter.

4.2 Similarity studies in PIC

In order to maintain physical accuracy and numeric stability in PIC simulations of plasmas, the Debye length has to be resolved. Depending on the region of interest, in thruster simulations namely the channel and the near exit plume region, the simulation domain can contain a large number of cells ($> 10.000.000$). The spatial resolution necessary for PIC therefore leads to large domain sizes, as is shown in table 4.1, which result in longer computation times. Hence, similarity scaling is applied, to downscale the domain.

Thruster	Channel Size (mm)	# cells ($\xi = 1$)	# cells (scaled)
Dm3a [6]	9.2 x 51.14	920 x 5114	92 x 511 ($\xi = 10$)
DP1 [12]	15.1 x 64	4081 x 17297	68 x 288 ($\xi = 60$)
TDP1 [P2]	5.03 x 21.33	1359 x 5765	68 x 288 ($\xi = 20$)

Table 4.1: Number of cells used in PIC simulation for peculiar HEMP-T designs with different scaling factors. The Debye length used for the calculation of the cell numbers is $\lambda_{Db} = 5 \cdot 10^{-3}$ mm

For the verification the thruster design of the DP1 has been chosen [12]. Because the original DP1 is a rather large system and only allows for big similarity scaling factors, to be computational feasible, an artificial test system, the TDP1 (Tiny-DP1), with smaller dimensions is set up, to allow small similarity scaling factors. The TDP1 is set up to have the same size ratios as the DP1 and therefore represents a geometrically downscaled thruster of the DP1. In [P2] it is shown, that this test system shows HEMP-like behaviour and qualifies as a test system to study the influence of the similarity scaling factor on HEMP-Ts. The simulation of the TDP1 with the lowest similarity scaling factor is set as the reference with the scaling factor $\xi_{ref} = 1$. By increasing the scaling factor and comparing global properties as well as the plasma solution, the similarity scaling can be verified. For ion thrusters the thrust and the percentage of ionization of the neutral feed gas are two of the most important operation parameters. Other parameters, which are evaluated here are the anode current and the axial electric field at the thruster exit. The anode current is one of the settable operation parameters in the experiment. On the other hand the electric field at the exit strongly depends on the extension of the plasma bulk in the channel and is characteristic for a HEMP-T. In figure 4.1 these system properties are shown over the variance of ξ .

It can be seen, that these values stay nearly constant within statistical deviations. The variation is determined by the changing ratio of the Debye length to the system size. With only small variations of the scaling factor, this ratio stays nearly constant and the increasing charge separation and the resulting effects are small, compared to the overall solution, see figure 4.1. These selected system properties represent the global solution of the HEMP-T and show the conservation of the solution for the applied similarity scaling.

Another important key observable is the electron distribution in the channel, which is directly correlated to the ionization. In figure 4.2 the axial profile of the electron density in the thruster channel is shown for different relative scaling factors like in figure 4.1. The general profile shows the electron density peaks at the cusps, the increased density of the electrons between the cusps and the density drop at the thruster exit. All profiles show a similar shape with variations in the density of up to 30%, which can be explained by the variations of the global ionization, see figure 4.1. The biggest variations in the density can

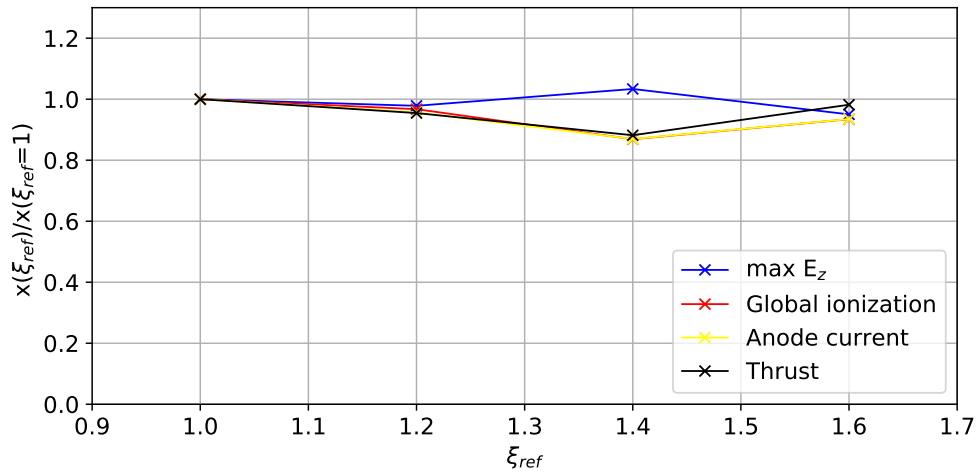


Figure 4.1: Behaviour of global values of the HEMP-T, namely the maximum electrical field at the exit (blue), the global ionization (red), the anode current (yellow) and the thrust (black), with rising scaling factor. The values are normalized by the values from $\xi_{ref} = 1$. Taken from [P2].

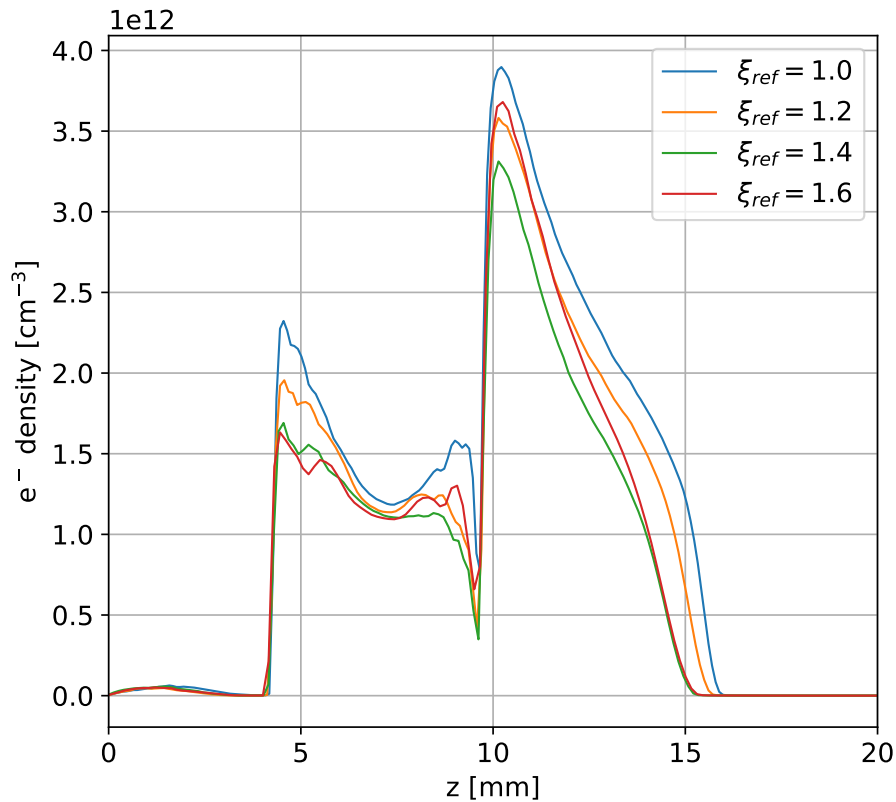


Figure 4.2: Axial electron density profile for distinctive relative scaling factors ξ_{ref} at the radius of $r = 4$ mm of the channel of the TDP1. Taken from [P2]

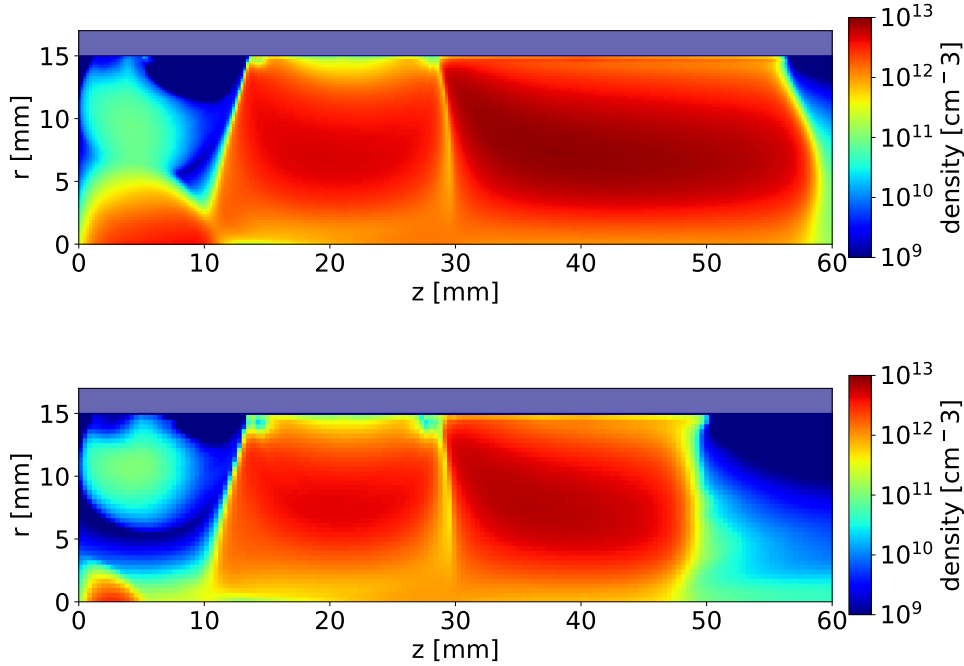


Figure 4.3: Comparison of electron density distribution in the discharge channel of the DP1 between two disparate similarity scaling factors, (top) $\xi = 60$ and (bottom) $\xi = 100$ [P2]

be found close to the thruster exit region. This can be explained by the expansion of the charge separation, which occurs on a length scale of the Debye length. With the preservation of the Debye length and simultaneous shrinking of the system size, a rising influence by electric fields produced by charge separation and of the grounded metal boundary at the exit can be expected. Normally, the domain size is chosen so that a change in the domain boundary conditions in the plume does not change the solution if they are changed from open boundary $E_z = 0$ to grounded potential $\Phi = 0$.

The self-similarity scaling scheme delivers an exact representation of the larger system in the scaled thruster channel. The parameters of interest are dominated by the plasma solution in the channel. They are conserved if the channel solution is maintained. Considering only small variations of the similarity scaling factors, the rising influence of the boundary conditions is therefore negligible. This is supported by the results from figure 4.1 and figure 4.2, which show the preservation of key properties of the HEMP-T, as already discussed above. The scaling scheme is applicable in a range of scaling factors, where the ratio of Debye length to the system size is still small or the influence of the sheath is negligible.

Now that the similarity scaling scheme is verified for small variations of the scaling factor, the limits of this approach can be studied on the DP1.

In figure 4.3 the electron density distribution in the channel of the DP1 is shown for the

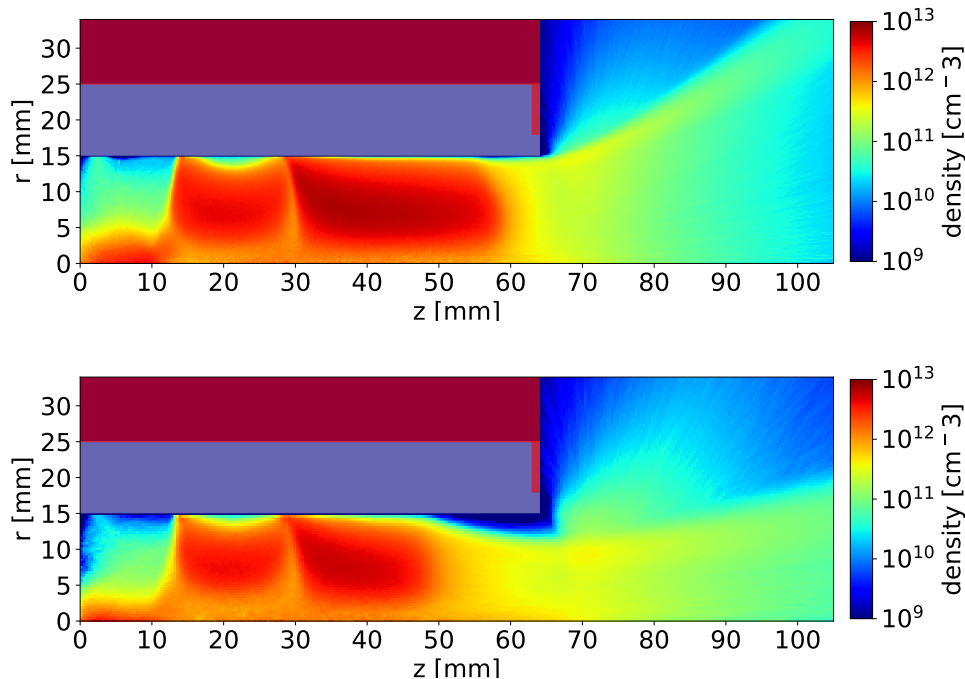


Figure 4.4: Comparison of ion density distribution of the DP1 between two disparate similarity scaling factors, (top) $\xi = 60$ and (bottom) $\xi = 100$ [P2]

scaling factors $\xi = [60, 100]$. Smaller scaling factors $\xi < 60$ are not considered, because of the already discussed computational limits. As expected in HEMP-Ts, the channel is filled with plasma and accordingly not easily influenced by expanding effects of charge separation, which occur with an increasing scaling factor. This is due to the comparably small Debye length in the channel. In the exit region, where the potential drop produces strong electric fields and the Debye length is larger compared to the channel, the influence of the scaling is stronger [P2], which can be seen for example in the ion density distribution in figure 4.4. With the relative increase of the Debye length, the length at which charge separation occurs in the discharge expands in regard to the system size. This leads to a relative expansion of the electric field decay length in the plasma, resulting in the grounded potential at the metal plate at the exit extending further and pushing the potential drop further into the channel. The plasma accordingly contracts further into the channel with higher scaling factor. The further the potential drop is located in the channel the smaller is the radial component of the exiting ions, resulting in a smaller emission angle like shown in figure 4.4. But in the channel center between the cusps the plasma solution is mostly maintained, showing the stability of the similarity scaling. The results show, that the channel solution is mostly preserved by the scaling, but the plume region is strongly influenced by the scaling at higher scaling factors.

While this is the case, it is important to address that the acceptable limit of the variations,

Scaling factor ξ	Thrust (mN)	Variation (%)	α_{exit} (°)	Variation (%)
60	18.2	0	38	0
80	17.3	~ 5	30	~ 17
100	14.7	~ 20	26	~ 32

Table 4.2: Comparison of Thrust and mean emission angle α_{exit} of the DP1 for distinct self-similarity scaling factors ξ . The variations are relative to the simulation with the self-similarity scaling factor 60.

e.g., of thrust or exit angle of the ion beam, depends on the use case. In this study of the DP1 the variation of the thrust and the mean emission angle are listed in table 4.2. Especially for high scaling factors the disparity is of several 10%. Relating to possible uncertainties in design and experiment, these levels can be acceptable [45].

Because the TDP1 was chosen as a geometric downscaled version of the DP1, further insights on the limits of the application of the similarity scaling can be obtained by comparing the results from the DP1 to the TDP1. If one could derive the system properties of a downscaled systems and apply it to bigger systems, the number of necessary prototypes to generate a new thruster design would decrease a lot. But the similarity scaling factor is not a good variable to compare the results of both systems. The influence of the same scaling factor on contrasting systems is expected to differ. This is due to the individual ratios of the Debye length to system size. For a better comparability of distinct systems under similarity scaling, a new factor

$$\tilde{\xi} = \frac{\lambda_{Db}\xi}{L}$$

is introduced, with the Debye length λ_{Db} , the applied similarity scaling factor ξ and the system size L . In figure 4.5 the axial (z) and radial (r) volume integrated ionization processes at various positions inside the thruster are shown over $\tilde{\xi}$. It can be seen, that the relative deviation of the axial cuts is generally lower than the radial cuts, but with increasing $\tilde{\xi}$ the discrepancies surge. The same behaviour can be seen for the electron density and the electric potential [P2]. These results provide a general guideline for the limits of application of the similarity scaling scheme. Considering that the deviations rise sharply at $\tilde{\xi} = 0.01$ while only showing variations of 20-30% to the initial state at $\tilde{\xi} = 0.006$, this ratio can be taken as a suggested limit of the scaling factor. In this case it means, that the channel length of the DP1 and TDP1 should be 100 times and the channel radius at least 20 times larger than the Debye length.

It is recommended to study the similarity scaling for each scenario, where it is applied, and decide what can be considered a realistic solution, for example by analysing the space charge.

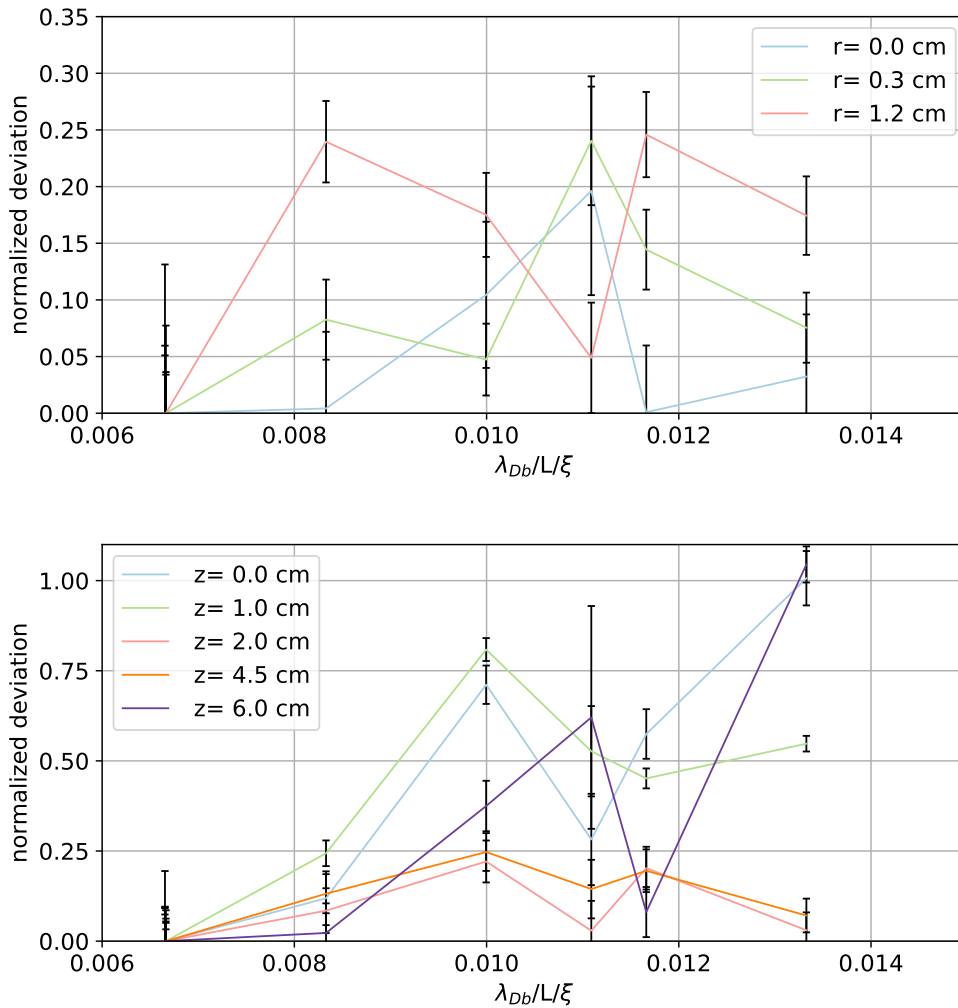


Figure 4.5: The absolute deviation of the volume integrated ionization processes. (Top) Axial variations from anode to thruster exit at various radial positions (r) and (bottom) radial variations from the axis to the dielectric of the channel at different axial positions (z) are shown in dependence of the ratio ξ [P2].

4.3 Subsummary

In this chapter it was shown, that the similarity scaling scheme is applicable to PIC simulations, because it maintains core parameters like thrust and the plasma solution of the thruster channel. But especially the exit region, where charge separation and boundary conditions influence the simulation, has to be handled with care with rising scaling factors. While the similarity scaling is a viable method to speed up PIC simulations, the application of high similarity scaling factors is limited by the ratio of the Debye length to the channel radius of the thruster and hence the expanding influence of charge separation and boundary conditions. The upper limit of applicable self-similarity scaling factors results in a definite maximum of shrinking the system size to increase the computation speed, while keeping physical accuracy. To further raise the speed of the exploration of the possible parameter

space of ion thrusters, a new approach is taken, combining evolutionary algorithms and PIC to explore optimized thruster designs. This approach is discussed in the next chapter.

5 Optimization of HEMP-T with PIC and MDO

In the previous chapter it was shown that the application of similarity scaling laws is a valid approach in PIC simulations to reduce the system size and hence decrease the computation time. This approach is limited to study selected thruster designs. To optimize HEMP-Ts, a method to explore a larger design space is presented here. Using a Multi-Objective-Design-Optimization (MDO) new optimized thruster designs are generated. In the MDO empirical parametrization is used, allowing to use experimental and modeling input. This means that this is not a self-consistent approach, but has the advantage of exploring a vast design space on a short time scale. By validating the generated thruster designs with PIC simulations and calculating the former empirical estimates for the given thruster design from the self-consistent simulation, a considerable improvement is possible adopting the self-consistent parameters from modeling.

5.1 Multi-Objective-Design-Optimization (MDO)

The group of Ogawa [46] developed a Multi-Objective-Design-Optimization tool for HEMP-Ts in 2017. MDO describes the process of optimizing the combination of various parameters, while considering interaction between the parameters during the calculation, making the generated optimum superior to the optimum generated by single parameter optimization. With MDO it is possible to generate thruster designs optimized for thrust T , specific impulse I_{sp} and total efficiency η by varying the applied anode voltage U_a , the anode current I_a , the mass flow rate m_a and the inner IMR and outer OMR magnetic radii. The base of the calculation is a set of 28 equations, delivered by the zero dimensional (0D) power balance model from Kornfeld et. al. [13]. With these equations and given anode potential, anode current and the magnetic mirror strength, the thruster performance can be estimated. These equations use the arrival probabilities of the electrons at the cusps as a measurement of the magnetic mirror strength. The iterative optimization process of the MDO starts with

a set of physically viable decision variables (listed above), which are transferred into a feasible geometry. Accepting this emerging thruster design, a magnetostatic and electrostatic calculation using ANSYS MAXWELL [47] is performed and from there the cusp arrival probabilities of the electrons are calculated. Afterwards the power balance model is solved with the calculated probabilities, which results in the performance values of the chosen thruster design. With the performance values the MDO generates optimized designs based on the former designs applying evolutionary algorithms to explore a huge design space. A more detailed description of the whole MDO process can be found in [P4]. While exploring a large design space and generating optimized thruster designs, the MDO uses empirical estimates, which are necessary for the power balance model. Therefore, it cannot guarantee self-consistent solutions. By applying PIC simulations for one promising thruster design, namely the S_1 [46], the estimates can be validated, analyzed and improved.

5.2 Validation of optimized HEMP-T

The expected performance parameters calculated by the MDO for the S_1 are listed in table 5.1.

System parameter	Optimized values
Anode voltage U_a	999.9 V
Anode current I_a	2.94 A
Neutral mass flow rate \dot{m}_a	49.98 sccm
IMR	9.91 mm
OMR	25.1 mm
Performance parameter	Optimized values
Thrust T	102.7 mN
Total efficiency η_t	36.5%
Specific impulse I_{sp}	2131 s

Table 5.1: Optimized design configuration with the calculated performance parameters [P4].

The same PIC code, as described in section 2.4, is used for simulating the S_1 . First solutions are given in [P4]. The boundary conditions are applied as they are given in the upper part of table 5.1, namely the anode voltage U_a , the mass flow rate \dot{m}_a and the dimensions of the magnets. The anode current is then achieved by the variation of the neutralizer strength, which is a free parameter in the PIC simulation.

As an example of the simulation results, the ion density distribution is shown in figure 5.1. The anode is located at the left boundary and the anode potential is set to 1000 V. The upper left and top boundary is grounded, while a fixed electric field gradient $E = 0$ is

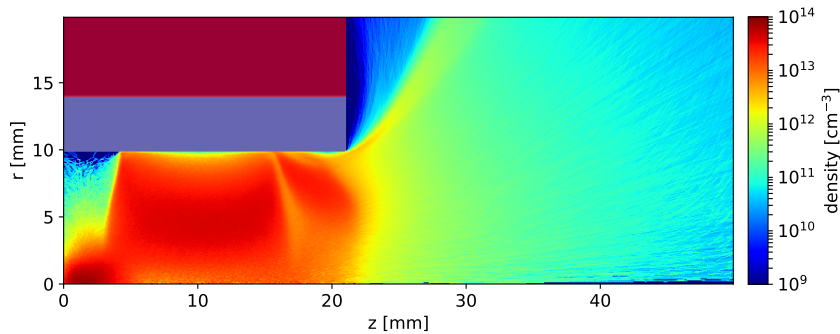


Figure 5.1: Xe^+ density distribution in the S_1 thruster. The gray box surrounding the channel from 9.91 mm to 13.5 mm represents the dielectric surface of the channel wall. The red box in the upper left corner is the grounded metal of the surrounding satellite.

applied at the right domain boundary. The neutral gas, xenon in this case, is injected at the center of the anode in the lower left corner of the simulation domain with a flow rate of 50 sccm. The discharge is fed with an electron source, simulating an effective neutralizer. It is implemented as a constant electron current, which is injected over the whole right domain boundary. The electron current was adjusted to provide the optimized anode current and was finally set to 800 mA.

Following [P3] and looking at figure 5.1, the S_1 shows qualitatively the same ion beam characteristics and channel physics as other HEMP-Ts. A detailed analysis of the physical processes in the S_1 is given in [P3].

One key finding of the PIC simulation is the dependency of the mean emission angle $\alpha_{emission}$ of the ions to the anode current I_a , or in other words the chosen operation state. In this case enough data was gathered to interpolate between various operation states in a reasonable range. A nearly linear dependency is derived with neutralizer currents in a range of 100...1000 mA, resulting i

$$\alpha_{emission}(I_a) = 7.7 \cdot I_a + 34.7 . \quad (5.1)$$

Using a simplified equation for the efficiency η in dependency of the anode current [46]

$$\eta = I_a \cos^2(\alpha_{emission}) \quad (5.2)$$

$$= I_a \cos^2(7.7 \cdot I_a + 34.7) , \quad (5.3)$$

it is now possible to include this effect in the optimization process. This is done by applying evolutionary algorithms [48] for different anode currents and applying equation 5.3 as the fitness function. The resulting optimum is at an anode current of 2.61 A, representing the optimal operation state concerning the anode efficiency for the PIC simulations. This is

supported by the self-consistently calculated anode current of 2.66 A from the full-kinetic data at the optimal operating state, see [P3]. The used PIC simulation needs a couple of weeks to get to an equilibrated state for one thruster design and one operation state. To get such scaling laws with PIC is very time consuming, since collecting enough data to apply interpolation schemes requires multiple simulations. This increases the need for a fast tool like MDO, to limit the operation states which can then be studied by more time consuming methods like PIC. The MDO only uses on average 10 minutes per configuration and a total of 18 days for 2560 design points.

Comparing the performance parameter of the optimized PIC operation state with the MDO, the results differ. The reasons for the differences are discussed in detail in [P3], with the main reason being the empirical input data for the used 0D power balance scheme. These empirical input data are namely the coefficients representing the relative proportion of gained electron power transferred to excitation, ionization and thermalization. They are now recalculated self-consistently with the results of the PIC simulations. The results are listed in [P3] and show a significant difference to the empirical estimated input parameters from the MDO. Especially, the fixed operating parameters, which were applied to set up the model the first time in [13], are responsible for the arising difference. Despite differing in the performance parameters, the MDO delivered a fast and robust tool using the simplified power balance model, resulting in a working HEMP-T design. The generated design has been verified, considering the current simulations. By supporting the lack of physical accuracy with self-consistent PIC simulations the model can be greatly improved. This process can be repeated iteratively with alternating cycles of PIC and MDO studies.

5.3 Subsummary

In this chapter it was shown, that optimized thruster designs generated with the simplified power balance model lack physical accuracy due to empirical input parameters. By simulating an optimized thruster, obtained by MDO, with PIC and compare the resulting performance values, obvious differences were revealed. To understand the difference in performance, the underlying 0D power balance model was investigated. By taking advantage of the full kinetic information of the system from PIC, more physically correct cusp arrival probabilities and energy transfer coefficients were calculated. Adopting these new improved parameters, the MDO predictions were greatly improved. This might lead to a powerful and time efficient tool, combining ab initio PIC simulations with optimization algorithms. The resulting tool will be of great interest to industrial applications.

6 Conclusions

In this work the applicability of scaling laws and optimization methods for ion thrusters were investigated with the means of PIC simulations.

The first question posed was the one of the general reliability of PIC. Therefore, the used PIC simulation was validated by simulating established systems, like rf discharges and one selected ion thruster design from THALES Deutschland GmbH. PIC was able to reproduce experimental measured high energy peaks of the negative ions in a ccrf discharge by including additional secondary ion emission. The application of PIC to the HEMP-T showed that the behaviour under the variation of the anode voltage is the same as in the experiment. To conclude, PIC was able to reproduce established experimental data and providing further physical insight into these systems, proving that PIC can be used for qualitative predictions.

Next, the aim was to verify the commonly used self-similarity scaling scheme applied to PIC simulations. After assuring the quality of the used PIC method, the presented self-similarity scaling was thus used to speed up the simulation. As a test system the DP1 thruster design was chosen. The influence of the chosen self-similarity scaling scheme on the solutions of the simulations was studied by varying the scaling factor and comparing the solutions. It was found that the scaling scheme conserves the solution of the channel of the thruster and global performance values. But in areas where charge separation and boundary conditions influence the solution, rising scaling factors lead to deviations. These deviations occur because of the relative increasing length of charge separation, namely the Debye length, to the system size. The application of the scaling is therefore limited by the ratio of Debye length to the system size. As long as this ratio is small the self-similarity scaling scheme can be safely applied.

With this in mind, PIC in combination with the similarity scaling is only applicable for a limited design space of ion thrusters. New approaches like the Multi-Objective-Design-Optimization MDO emerged, providing a tool which generates new optimized thruster designs in a short amount of time. Because this thesis was looking for tools which work in an application oriented manner, the resulting designs of the MDO were of special interest. One of these designs was thoroughly analyzed using PIC with the aim of verifying the

MDO. It was shown that the optimization model delivers working HEMP-T designs, but the performance parameters showed considerable deviations. The reason for these deviations was traced back to the used power balance model, because the MDO uses empirical energy transfer coefficients. Self-consistent PIC simulations have shown that these were not applicable for the chosen thruster design and the optimized operation state. As a result the MDO was improved, by using the energy transfer coefficients gained from PIC simulations, leading to a new collaborative tool to generate optimized thruster designs.

This is just the start of a robust and fast tool to generate optimized HEMP-Ts. In the future further parameters for the optimization process have to be found. Promising candidates to be considered are the length of the channel and the decay length of the neutral density. More detailed studies will show their influence on ion thruster designs and hence improve future optimization approaches.

7 Bibliography

- [1] G. Beutler, R. Weber, U. Hugentobler, M. Rothacher, and A. Verdun, “Gps satellite orbits”, in, P. J. G. Teunissen and A. Kleusberg, Eds. Berlin, Heidelberg: Springer Berlin Heidelberg, 1998, pp. 43–109, ISBN: 978-3-642-72011-6. [Online]. Available: https://doi.org/10.1007/978-3-642-72011-6_2.
- [2] R. De Gaudenzi, C. Elia, and R. Viola, “Analysis of satellite broadcasting systems for digital television”, *Selected Areas in Communications, IEEE Journal on*, vol. 11, pp. 99–110, Feb. 1993. DOI: 10.1109/49.210548.
- [3] B. Turner, “International telecommunications satellite organization (intelsat)”, in. London: Palgrave Macmillan UK, 2000, pp. 115–115, ISBN: 978-0-230-27129-6. [Online]. Available: https://doi.org/10.1057/9780230271296_69.
- [4] D. Lev, R. Myers, and e. a. K.M. Lemmer, “The technological and commercial expansion of electric propulsion in the past 24 years”, *35th IEPC*, 2017.
- [5] N. Koch, M. Schirra, S. Weis, A. Lazurenko, B. van Reijen, J. Haderspeck, A. Genovese, P. Holtmann, R. Schneider, K. Matyash, and O. Kalentev, “The hempt concept - a survey on theoretical considerations and experimental evidences”, *32nd IEPC*, no. 236, Sep. 2011.
- [6] G. Kornfeld, N. Koch, and G. Coustou, “First test results of the hemp thruster concept”, *28th IEPC*, no. 212, 2003.
- [7] H. Kornfeld G. Seidel and J. Wegener, “Plasma accelerator arrangement.”, *filed 26 June 1998*, no. priority: Germany No. 198 28 704.6, 1999.
- [8] D. Tskhakaya, K. Matyash, R. Schneider, and F. Taccogna, “The particle-in-cell method”, *Contributions to Plasma Physics*, vol. 47, no. 8-9, pp. 563–594, 2007.
- [9] J. Lacina, “Similarity rules in plasma physics”, *Plasma Physics*, vol. 13, no. 4, pp. 303–312, Apr. 1971. DOI: 10.1088/0032-1028/13/4/003. [Online]. Available: <https://doi.org/10.1088%2F0032-1028%2F13%2F4%2F003>.
- [10] F. Taccogna, S. Longo, M. Capitelli, and R. Schneider, “Self-similarity in hall plasma discharges: Applications to particle models”, *Physics of Plasmas*, vol. 12, no. 5, p. 053 502, 2005. DOI: 10.1063/1.1877517. eprint: <https://doi.org/10.1063/1.1877517>. [Online]. Available: <https://doi.org/10.1063/1.1877517>.

- [11] P. Matthias, R. Schneider, R. Heidemann, F. Holtmann, D. Kahnfeld, and K.-F. Lüskow, “Influence of different anode voltages on the hemp”, *35th IEPC*, no. 310, Oct. 2017.
- [12] N. Koch, J. Duras, D. Kahnfeld, P. Matthias, G. Bandelow, K. Lüskow, R. Schneider, S. Kemnitz, and M. Schirra, “Particle-in-cell simulation of a hemp thruster digital prototype optimized for future satellite applications”, Oct. 2017, IEPC-2017-329.
- [13] G. Kornfeld, N. Koch, and H. Harmann, “Physics and evolution of hemp-thrusters”, *30th IEPC*, no. 108, pp. 17–20, Sep. 2007.
- [14] U. Flender and K. Wiesemann, “Characterization of plasma-surface contacts in low-pressure rf discharges using ion energy analysis and langmuir probes”, *Plasma Chemistry and Plasma Processing*, no. 15, pp. 123–157, 1995.
- [15] M. Moravej and R. Hicks, “Atmospheric Plasma Deposition of Coatings Using a Capacitive Discharge Source”, *Chemical Vapor Deposition*, vol. 11, no. 11-12, pp. 469–476, 2005.
- [16] J. Meichsner, M. Schmidt, R. Schneider, and H.-E. Wagner, *Nonthermal Plasma Chemistry and Physics*. CRC Press, 2012.
- [17] G. Gibson, W. Jordan, and E. Lauer, “Particle Behaviour in Static, Axially Symmetric, Magnetic Mirror and Cusp Geometries”, *The Physics of Fluids*, vol. 6, pp. 116–133, 1963.
- [18] F. Chen, *Introduction to Plasma Physics and Controlled Fusion*. Springer, 2015, ISBN: 978-3-319-22309-4.
- [19] G. Fubiani, L. Garrigues, G. Hagelaar, N. Kohen, and J. Boeuf, “Modeling of plasma transport and negative ion extraction in a magnetized radio-frequency plasma source”, *New Journal of Physics*, vol. 19, no. 1, p. 015 002, 2017. [Online]. Available: <http://stacks.iop.org/1367-2630/19/i=1/a=015002>.
- [20] S. J. J, “Fully kinetic numerical modeling of a plasma thruster”, *PhD Massachusetts Institute of Technology*, 2001.
- [21] O. Kalentev, K. Matyash, J. Duras, K.-F. Lüskow, R. Schneider, N. Koch, and M. Schirra, “Electrostatic ion thrusters - towards predictive modeling”, *Contributions to Plasma Physics*, vol. 54, no. 2, pp. 235–248, Feb. 2014. DOI: 10.1002/ctpp.201300038.
- [22] C. Birdsall and A. Langdon, *Plasma Physics via Computer Simulation*. CRC Press, 2004, ISBN: 9780750310253.
- [23] K. Matyash, O. Kalentev, R. Schneider, F. Taccogna, N. Koch, and M. Schirra, “Kinetic simulation of the stationary hemp thruster including the near-field plume region”, *31st IEPC*, no. 110, pp. 20–24, 2009.

-
- [24] C. K. Birdsall and D. Fuss, “Clouds-in-clouds, clouds-in-cells physics for many-body plasma simulation”, *Journal of Computational Physics*, vol. 3, no. 4, pp. 494–511, Apr. 1969. DOI: 10.1016/0021-9991(69)90058-8. [Online]. Available: [http://dx.doi.org/10.1016/0021-9991\(69\)90058-8](http://dx.doi.org/10.1016/0021-9991(69)90058-8).
- [25] S. Li Xiayoe, J. Gilbert, and J. Demmel, “Superlu users’ guide”, 1999.
- [26] J. P. Boris, “Relativistic plasma simulation-optimization of a hybrid code”, *Proceeding of Fourth Conference on Numerical Simulations of Plasmas*, Nov. 1970.
- [27] V. Vahedi, G. DiPeso, C. Birdsall, M. Lieberman, and T. Rognlien, “Capacitive rf discharges modelled by particle-in-cell monte carlo simulation. i. analysis of numerical techniques”, *Plasma Sources Science and Technology*, vol. 2, no. 4, p. 261, 1993.
- [28] F. Bronold, K. Matyash, D. Tskhakaya, R. Schneider, and H. Fehske, “Radio-frequency discharges in oxygen: I. particle-based modelling”, *Journal of Physics D: Applied Physics*, vol. 40, no. 21, p. 6583, 2007.
- [29] T. Takizuka and H. Abe, “A binary collision model for plasma simulation with a particle code”, *Journal of Computational Physics*, vol. 25, no. 3, pp. 205–219, 1977.
- [30] K. Matyash, “Kinetic modeling of multi-component edge plasmas.”, Dissertation, Ernst-Moritz-Arndt Universität Greifswald, 2003.
- [31] A. Langdon, “Effects of the spatial grid in simulation plasmas”, *Journal of Computational Physics*, vol. 6, no. 2, 1970.
- [32] C. K. Birdsall and N. Maron, “Plasma self-heating and saturation due to numerical instabilities”, *Journal of Computational Physics*, vol. 36, no. 1, pp. 1–19, Jun. 1980. DOI: 10.1016/0021-9991(80)90171-0. [Online]. Available: [http://dx.doi.org/10.1016/0021-9991\(80\)90171-0](http://dx.doi.org/10.1016/0021-9991(80)90171-0).
- [33] H. Ueda, Y. Omura, H. Matsumoto, and T. Okuzawa, “A study of the numerical heating in electrostatic particle simulations”, *Computer Physics Communications*, vol. 79, 1994.
- [34] V. Vahedi and M. Surendra, “A monte carlo collision model for the particle-in-cell method: Applications to argon and oxygen discharges”, *Computer Physics Communications*, vol. 87, no. 1, pp. 179–198, 1995, Particle Simulation Methods, ISSN: 0010-4655. DOI: [https://doi.org/10.1016/0010-4655\(94\)00171-W](https://doi.org/10.1016/0010-4655(94)00171-W). [Online]. Available: <http://www.sciencedirect.com/science/article/pii/001046559400171W>.
- [35] M. Hayashi, “Bibliography of electron and photon cross sections with atoms and molecules published in the 20th century - xenon”, NIFS, Tech. Rep. NIFS-DATA-79, 2003. [Online]. Available: <http://www.nifs.ac.jp/report/NIFS-DATA-079.pdf>.
- [36] P. Arlinghaus, “Application of advanced solver for pic”, 2018.

- [37] D. Kahnfeld, J. Duras, P. Matthias, S. Kemnitz, P. Arlinghaus, G. Bandelow, K. Matyash, N. Koch, and R. Schneider, “Numerical modeling of high efficiency multi-stage plasma thrusters for space applications”, *Reviews of Modern Plasma Physics*, vol. 3, no. 1, 2019.
- [38] R. Schneider, K. Matyash, O. Kalentev, F. Taccogna, N. Koch, and M. Schirra, “Particle-in-cell simulations for ion thrusters”, *Contributions to Plasma Physics*, vol. 49, no. 9, pp. 655–661, 2009.
- [39] A. Keller, P. Köhler, F. Hey, M. Berger, C. Braxmaier, D. Feili, D. Weise, and U. Johann, “Parametric Study of HEMP-Thruster, Downscaling to μN Thrust Levels”, *33rd IEPC*, no. 269, 2013.
- [40] A. Keller, P. Köhler, W. Gärtner, and et al., “Feasability of a down-scaled HEMP-Thruster”, *32nd IEPC*, 2011.
- [41] F. Hey, T. Brandt, G. Kornfeld, and et al., “Downscaling a HEMPT to micro-newton thrust levels: Current status and latest results”, *34th IEPC*, 2015.
- [42] N. Koch, H. Harmann, and G. Kornfeld, “Development & test status of the thales high efficiency multistage plasma (hemp) thruster family”, *29th IEPC*, 2005.
- [43] —, “Status of the thales high efficiency multi stage plasma thruster development for hemp-t 3050 and hemp-t 30250”, *30th IEPC*, 2007.
- [44] J. Duras, D. Kahnfeld, G. Bandelow, S. Kemnitz, K. Lüsrow, P. Matthias, N. Koch, and R. Schneider, “Ion angular distribution simulation of the highly efficient multi-stage plasma thruster”, *Journal of Plasma Physics*, vol. 83, 2017. DOI: {10.1017/S0022377817000125}.
- [45] S. Weis, A. Lazurenko, A. Genovese, R. Heidemann, P. Holtmann, and H. Stalzer, “Overview, qualification and delivery status of the hempthruster based ion propulsion system for smallgeo”, *35th IEPC*, 2017.
- [46] T. Fahey, M. A., and H. Ogawa, “High fidelity multi-objective design optimization of a downscaled cusped field thruster”, *Aerospace*, no. 4, p. 55, 2017.
- [47] A. Inc., “Ansys electronics desktop suite ver.17.2 users’ guide”, 2016.
- [48] D. Dasgupta and Z. Michalewicz, *Evolutionary Algorithms in Engineering Applications*. Springer Science & Business Media, 2013.

8 Cumulative thesis articles

Author Contributions

Article [P1]: "PIC simulations of capacitively coupled oxygen rf discharges", P. Matthias, G. Bandelow, K. Matyash, J. Duras, P. Hacker, D. Kahnfeld, S. Kemnitz, L. Lewerentz, K.F. Lüsrow, J. Meichsner and R. Schneider, *Eur. Phys. J. D* 72:86 (2018).

All authors carved out the problem, outlined the calculation, and determined the scope of the article. P. Matthias and R. Schneider performed the analytic calculation. P. Matthias performed the numerical calculation, based on numerical developments by S. Kemnitz, G. Bandelow, J. Duras and D. Kahnfeld. J. Meichsner performed the experiments and provided the data used. The manuscript was written by P. Matthias and R. Schneider and was edited by all authors.

Article [P2]: "Similarity scaling - application and limits for ion thruster PIC modeling", P. Matthias, D. Kahnfeld, S. Kemnitz, J. Duras, N. Koch and R. Schneider, *Physics of Plasmas* e201900199 (2020).

All authors carved out the problem, outlined the calculation, and determined the scope of the article. P. Matthias and R. Schneider performed the analytic calculation. P. Matthias performed the numerical calculation, based on numerical developments by D. Kahnfeld, S. Kemnitz and J. Duras. The manuscript was written by P. Matthias and R. Schneider and was edited by all authors.

Article [P3]: "Particle-in-cell simulation of an optimized high-efficiency multistage plasma thruster", P. Matthias, D. Kahnfeld, R. Schneider, S.H. Yeo and H. Ogawa, *Contribution to Plasma Physics* e201900028 (2019).

All authors carved out the problem, outlined the calculation, and determined the scope of the article. P. Matthias performed the numerical calculation, based on numerical developments by D. Kahnfeld. S.H. Yeo and H. Ogawa developed the design of the ion thruster. The manuscript was written by P. Matthias and R. Schneider and was edited by all authors.

Article [P4]: "Multi-Objective Optimization and Particle-In-Cell Simulation of Cusped Field Thruster for Micro-Satellites Platform", S.H. Yeo, T. Fahey, H. Ogawa, A. Muffati, P. Matthias, D. Kahnfeld, M. Padivattathumana and R. Schneider, *AIAA* (2019).

All authors carved out the problem, outlined the calculation, and determined the scope of the article. S.H. Yeo, T. Fahey, A. Muffati and H. Ogawa performed the optimization calculation. P. Matthias and R. Schneider performed the analytic calculation. P. Matthias performed the numerical calculation, based on numerical developments by S. Kemnitz, G. Bandelow, J. Duras and D. Kahnfeld. The manuscript was written by S.H. Yeo, H. Ogawa, P. Matthias and R. Schneider and was edited by all authors.

Article [P5]: "Numerical modeling of high efficiency multistage plasma thrusters for space applications", D. Kahnfeld, J. Duras, P. Matthias, S. Kemnitz, P. Arlinghaus, G. Bandelow, K. Matyash, N. Koch and R. Schneider, *Reviews of Modern Plasma Physics* **3**(1): 11 (2019). All authors carved out the problem, outlined the calculation, and determined the scope of the article. D. Kahnfeld performed the analytic and the numerical calculation, based on numerical developments by S. Kemnitz, G. Bandelow, J. Duras, P. Matthias, K. Matyash and P. Arlinghaus. The manuscript was written by D. Kahnfeld, R. Schneider and N. Koch and was edited by all authors.

Article [P6]: "Breathing modes in HEMP thrusters", D. Kahnfeld, R. Heidemann, J. Duras, P. Matthias, G. Bandelow, K.F. Lüskow, S. Kemnitz, K. Matyash and R. Schneider, *Plasma Sources and Technology* **27**(12): 124002 (2018). All authors carved out the problem, outlined the calculation, and determined the scope of the article. D. Kahnfeld performed the analytic and the numerical calculation, based on numerical developments by S. Kemnitz, G. Bandelow, J. Duras, P. Matthias and K. Matyash and K.F. Lüskow. R. Heidemann provided the experimental data. The manuscript was written by D. Kahnfeld, R. Schneider and N. Koch and was edited by all authors.

Article [P7]: "Ion angular distribution simulation of the Highly Efficient Multistage Plasma Thruster", J.Duras, D. Kahnfeld, G. Bandelow, S. Kemnitz, K.F. Lüskow, P. Matthias, N. Koch and R. Schneider, *Journal of Plasma Physics* **83**(1): 595830107 (2017). All authors carved out the problem, outlined the calculation, and determined the scope of the article. D. Kahnfeld performed the analytic calculation. J. Duras performed the numerical calculation, based on numerical developments by D. Kahnfeld, S. Kemnitz, G. Bandelow, P. Matthias and K.F. Lüskow. The manuscript was written by J. Duras, D. Kahnfeld, R. Schneider and N. Koch and was edited by all authors.

Article [P8]: "Particle-in-cell simulation of the cathodic arc thruster", K.F. Lüskow, P.R.C. Neumann, G. Bandelow, J. Duras, D. Kahnfeld, S. Kemnitz, P. Matthias, K. Matyash and R. Schneider, *Physics of Plasmas* **25**(1): 013508 (2018).

All authors carved out the problem, outlined the calculation, and determined the scope of the article. K.F. Lüskow and R. Schneider performed the analytic calculation. K.F. Lüskow performed the numerical calculation, based on numerical developments by D. Kahnfeld, S. Kemnitz, G. Bandelow, K. Matyash, J. Duras and P. Matthias. The manuscript was written by K.F. Lüskow, R. Schneider and P.R.C Neumann and was edited by all authors.

Confirmed:

(Prof. Dr. Ralf Schneider)

Greifswald, _____, 2021

(Paul Matthias)

Greifswald, _____, 2021

PIC simulations of capacitively coupled oxygen rf discharges^{*}

Paul Matthias^{1,a}, Gunnar Bandelow¹, Konstantin Matyash¹, Julia Duras², Philipp Hacker¹, Daniel Kahnfeld¹, Stefan Kemnitz³, Lars Lewerentz¹, Karl F. Lüskow¹, Jürgen Meichsner¹, and Ralf Schneider¹

¹ Institute of Physics, Ernst-Moritz-Arndt-University Greifswald, 17489 Greifswald, Germany

² Nuremberg Institute of Technology, 90489 Nuremberg, Germany

³ Institute of Computer Science and Technology, University Rostock, 18051 Rostock, Germany

Received 31 August 2017 / Received in final form 13 November 2017

Published online 22 May 2018 – © EDP Sciences, Società Italiana di Fisica, Springer-Verlag 2018

Abstract. Capacitively coupled discharges with a radio-frequency operated voltage (ccrf) are important for plasma assisted material processing. Experiments with electronegative oxygen ccrf discharges show a high-energy peak in the energy distribution of negative ions arriving at the anode, depending on the cathode material used. One possible explanation is ionization at or close to the surface of the cathode for the production of negative ions. By introducing an additional surface ionization model into a Particle-In-Cell (PIC) simulation with Monte Carlo Collisions (MCC) the experimental result is reproduced qualitatively. Comparison of one dimensional and two dimensional simulation results allows an improved understanding of the microscopic processes determining the dynamics of negative ions.

1 Introduction¹

In industrial applications plasma is used for plasma etching, thin-film deposition [1] and sputter techniques [2,3]. Especially reactive electronegative plasmas increase sputtering and deposition rates and are widely used in technology. For the treatment of surfaces it is important to know the detailed energy distribution functions (EDF) of the impinging ions, and in case of electronegative plasmas the EDF of negative ions as well [4–6]. Experiments show high energy peaks in the EDF for negative ions arriving at the grounded electrode in an asymmetric ccrf discharge with oxygen as the process gas, depending on the powered electrode material used. Therefore, surface effects may be important for the EDF of the negative ions. Investigating surface effects and their impact on the plasma is the aim of this work.

2 Surface effects and secondary ion emission

In addition to secondary electron emission [7] there also exists secondary ion emission (SIE). Theoretical studies of surface ionization are mostly devoted to the production of positive ions from incident atoms of thermal energy [5]. The degree of ionization can be derived by applying thermodynamics.

The ionization coefficient $\alpha^+(M^+)$ is given by

$$\alpha^+(X^+) = \frac{n^+}{n} = \frac{1-r^+}{1-r} \cdot \frac{w^+}{w} \exp\left(\frac{\bar{\Phi}^+ + e\sqrt{eF} - I(X)}{k_B T}\right), \quad (1)$$

where n^+ and n are the numbers of positive ions X^+ and neutrals X coming from a unit surface area per unit time, w^+/w is the statistical weight ratio of X^+ to X , r^+ and r are the internal reflection coefficients at the potential barrier on the emitter surface, $\bar{\Phi}^+$ is the average work function, T is the absolute temperature at the surface, F is the externally applied field and $I(X)$ is the initial energy of the impinging atoms.

Equation (??) can also be used for a surface which emits negative ions. A negatively biased surface like the powered electrode in an asymmetric ccrf discharge is assumed with an equilibrium condition

$$X + e^- (\text{in the substrate metal}) \rightleftharpoons X^- \quad (2)$$

at the surface. The equation for the negative ionization coefficient is derived in analogy to equation (??)

$$\alpha^-(X^-) = \frac{n^-}{n} = \frac{1-r^-}{1-r} \cdot \frac{w^-}{w} \exp\left(\frac{-\bar{\Phi}^- - e\sqrt{eF} + A(X)}{k_B T}\right), \quad (3)$$

^{*} Contribution to the Topical Issue “Fundamentals of Complex Plasmas”, edited by Jürgen Meichsner, Michael Bonitz, Holger Fehske, Alexander Piel.

^a e-mail: pm101481@uni-greifswald.de

where $A(X)$ is the electron affinity of atom X , $\bar{\phi}^-$ is the average effective work function for producing the negative ion X^- on the metal surface and the other parameters are in analogy to the case of positive ion emission. No detailed theoretical and experimental studies of reflection coefficients exist for negative ions. Therefore, no cross-section data for such processes are available. For the simulations in this work an empirical production efficiency $\eta = n_-/n_+$ is introduced for positive ions hitting a surface. n_+ is the number of incoming positive ions and n_- the number of emitted negative ions.

To get a microscopic understanding of the underlying physics a ccrf oxygen discharge is simulated kinetically with PIC-MCC [8,9]. This is necessary, because mean free paths are of the same magnitude as the electrode gap and relaxation of the distribution functions to Maxwell distributions due to collisions does not occur. This means that fluid models are incomplete and kinetic models have to be applied.

3 PIC-MCC method

The discharge of the experiment is operated in cylindrical geometry. For the region close to the center of the discharge a one-dimensional approach is usually used neglecting transport processes in radial direction. This can be further improved using a two-dimensional simulation in radial and axial direction. Particle-in-Cell (PIC) with Monte-Carlo-Collisions (MCC) methods simulate the motion of pseudo-particles, representing a large number of real particles, in continuous phase space while macro quantities like density or potentials are computed on stationary mesh points [10]. The method follows the trajectories of charged particles in self-consistent electromagnetic (in this case electrostatic) fields computed on a fixed mesh. The macro-force is then calculated from the field equations. Macro forces are used to avoid the computer time consuming particle-particle interactions which scale quadratic with the particle number N^2 . In contrast to this, the particle-mesh method just scales with $N \log N$ and is hence much faster [8]. For the system studied here, neutrals are considered as a constant background due to their much higher density compared with the charged species and the rather low ionization degree in such discharges. The neutrals act as a kind of reservoir. Therefore, the collision dynamics is only resolved for the charged species. Here the same collision and cross sections were used as in [11].

4 Simulation of ccrf oxygen discharges

As standard parameters a pressure of 10 Pa and a peak-to-peak voltage of 800 V_{pp} are chosen. Pressure is reduced down to 2 Pa. The radio-frequency is set to 13.56 MHz as in experiment. PIC simulations work with normalized units to resolve the spatial (Debye length) and temporal (plasma frequency) properties. Reference parameters for the normalized PIC units are an electron density of $n_e = 5 \cdot 10^9 \text{ cm}^{-3}$ and an electron temperature of $T_e = 4 \text{ eV}$. This results in a Debye-length of the system

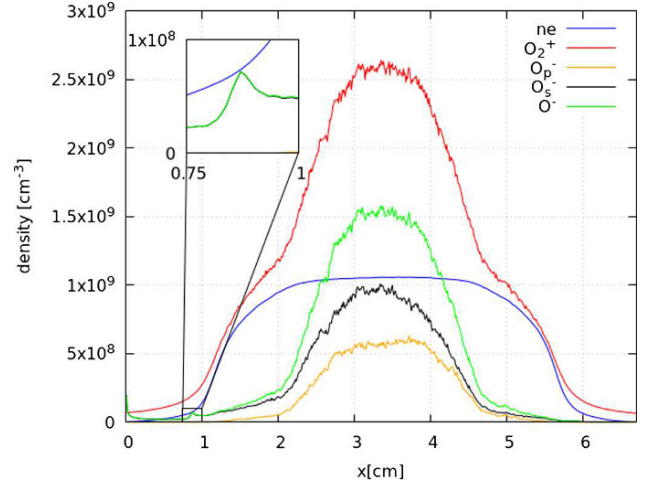


Fig. 1. Densities of e^- , O_2^+ and O^- with secondary ion emission at the powered electrode ($\eta = 0.03$). The pressure was 5 Pa and the rf voltage was set to $U_{rf} = 800 \text{ V}_{pp}$. The zoomed in area shows the small density peak of O_s^- at the powered electrode sheath edge. The powered electrode is located at $x = 0 \text{ cm}$.

of $\lambda_{Db} \approx 0.021 \text{ cm}$ and an electron plasma frequency of $\omega_{pe} \approx 3.99 \cdot 10^9 \text{ s}^{-1}$. The electrode gap of the experiment is 5 cm. Studies have shown that the choice of η in a short range of $[0.01 \dots 0.1]$ has only little influence on the plasma. In the following simulations only secondary negative ion emission is added for the powered electrode as an additional wall process with an efficiency of $\eta = 0.03$ [7] to separate the influence of other processes.

4.1 Discharges with secondary ion emission

Including the SIE injection model of oxygen anions at the powered electrode, one can see in Figure ?? that the number density of the anions is slightly shifted towards the powered electrode compared with the grounded electrode where no SIE model is applied.

The anion number densities were separated into the ones produced by volume processes in the plasma O_p^- and the ones produced at the surface O_s^- .

A small density peak of O_s^- at the sheath edge in front of the powered electrode is noticeable. It forms due to elastic collisions of the anions O_s^- in the sheath.

The O_s^- get accelerated in the sheath, cross the bulk and then get reflected in the sheath of the grounded electrode similar to the movement of the electrons, but on a larger time scale (microseconds for electrons but milliseconds for negative ions). In the energy distributions of O_s^- an additional high-energy peak builds up (Fig. ??). It decays with the time of flight (distance to the powered electrode) due to charge-exchange and elastic collisions with neutral molecules O_2 which results in an energy loss for the anions. Also, a part of the anions get detached by neutrals or recombine with positive ions. In existing publications it is assumed that if an anion collides with a neutral it is very likely to get detached due to the cross-section [12].

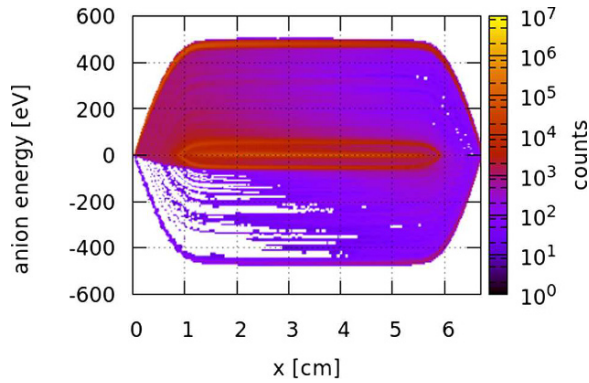


Fig. 2. Energy distribution function of O_s at 5 Pa and a driver voltage of 800 V_{pp} . The “sign” of the energy indicates the direction of the particles. The powered electrode with additional SIE is located at $x = 0$ cm.

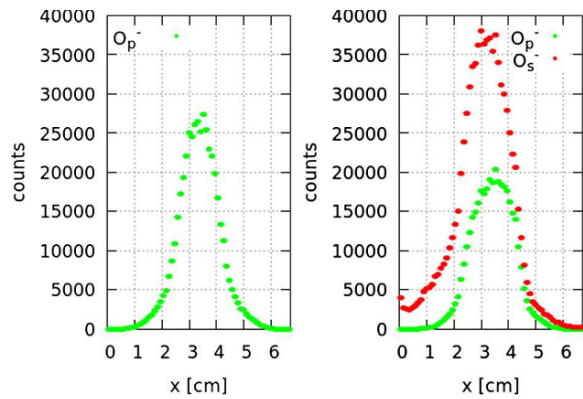


Fig. 3. Number of elastic collisions of negative ions O^- with neutral molecules O_2 per 10^5 time steps without SIE (left) and with SIE ($\eta = 0.03$) (right) where the two O^- species are separated. The powered electrode is located at $x = 0$ cm.

In Figure ?? the difference between the numbers of elastic collisions for a normal discharge and a discharge with additional SIE are shown. It is obvious that the anions undergo elastic collisions which leads to an energy loss and a continuous plateau in the energy distribution. Most elastic collisions occur in the bulk while the sheaths are mostly collisionless. But for the surface ions O_s^- one can see that the collisions in the powered electrode sheath cannot be neglected. They lead to an energy loss for the anions which influence their energy distribution.

In Figure ?? a structure in the lower energy region in the bulk can be seen. The elastic collisions produce a peak structure in the ion energy distribution. To study the sheath dynamics during a rf period one phase of the energy distribution function for O_s^- is shown in Figure ??.

The density peak at the sheath edge (as seen earlier in Fig. ??) originates from the low-energy peak in the energy distribution. With the average ion energy in the sheath and the rf-cycle time τ_{rf} one can calculate the transit time τ_{ion} . Assuming an average ion energy of 40–50 eV and a traveled distance of ≈ 1 cm it follows the ratio $\tau_{ion}/\tau_{rf} \approx 4.5$. This is the number of rf-cycles an

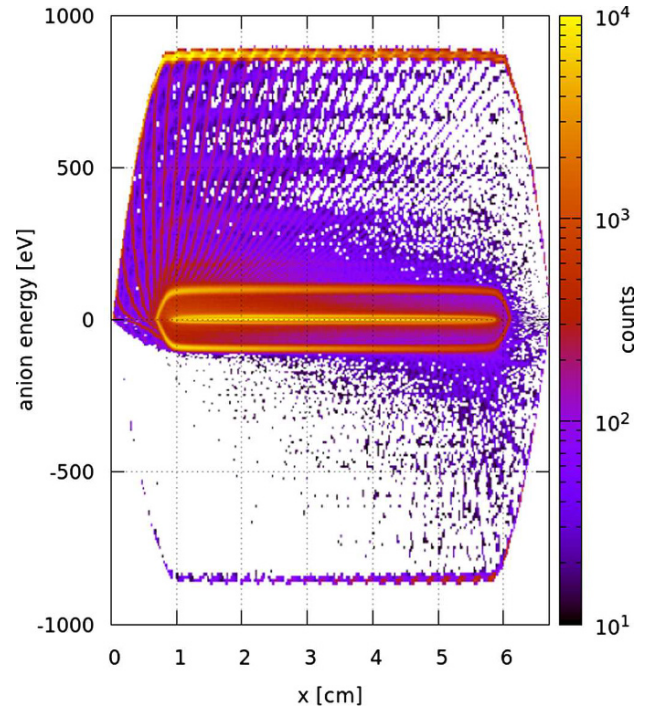


Fig. 4. Same energy distribution as in Figure ?? with an applied driver voltage of 1600 V_{pp} at $t = 0$ of the rf cycle, which is equal to a voltage of $U(t) = 0$ at the powered electrode.

anion stays in the sheath. Hence the number of peaks in the negative ion energy distribution must be similar. In Figure ?? one can see that 4–5 low energy peaks in the sheath build up through elastic collisions of the negative ions with neutrals. At the sheath edge these energy density cycles overlay. Additional simulations have shown that without elastic collisions no additional density peak builds up. Hence, the energy plateau of the anions is mainly influenced by elastic collisions. The spatial resolved IEDF leads directly to the density distribution of the negative ions O_s^- . The density peak at the sheath edge (see Fig. ??) originates from the low-energy peak in the energy distribution of the negative surface ions O_s^- .

In the experiment the powered electrode potential is shifted by the self-bias voltage due to the asymmetry of the electrodes resulting in an asymmetric potential. As a consequence of this asymmetry the anions can get enough energy to get to the grounded electrode while in the 1d3v simulation they get reflected by the sheath potential due to its intrinsic symmetry. This results in a higher probability of elastic collisions with neutrals since the ions stay longer in the discharge leading to the discussed density peaks at the sheath. Figure ?? confirms that negative ions produced at the surface may lead to the measured high-energy peak. Since the experiment is driven by an adjustable network power, while the simulation depends on the voltage at the powered electrode, the results are only comparable on a qualitative level. But the energy distribution function of the simulation has additional low energy peaks (at <100 eV), too. They are probably created

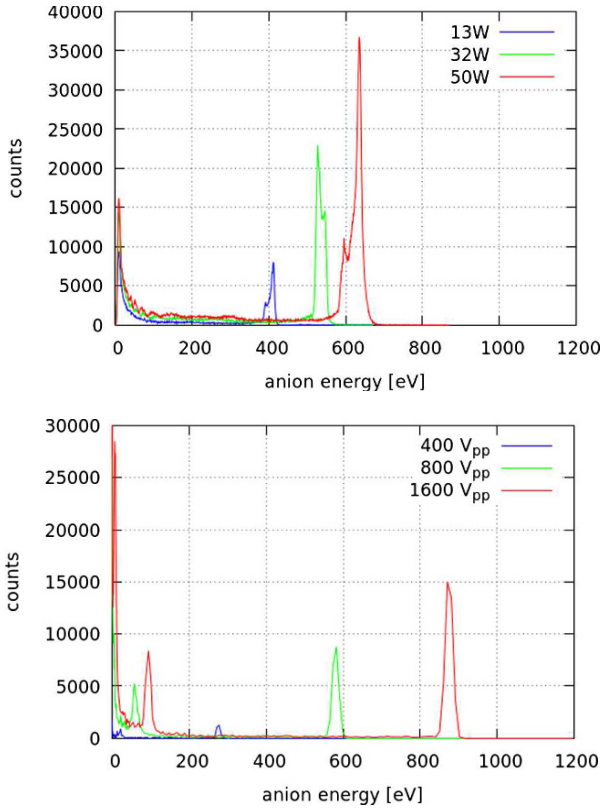


Fig. 5. Energy distribution of negative ions O^- . Top: experimental results for MgO measured at the grounded electrode for different rf powers. Bottom: simulation result with 1d3v PIC simulation with additional SIE, taken at the grounded electrode sheath edge 6 cm at different rf powers at 5 Pa and $\eta = 0.03$.

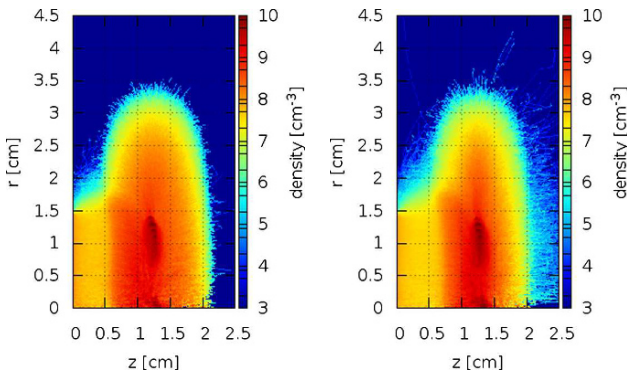


Fig. 6. Negative ion density distribution at 10 Pa (left) and 6 Pa (right). The powered electrode is located at $z = 0$ cm.

due to the intrinsic symmetry in the 1d3v simulation. In the experiment all high-energy anions are detected and thereby removed from the discharge.

Additional studies have been done varying pressure, voltage and injection coefficient. Their results support the hypothesis that the high energy peaks are created by secondary ion emission.

5 Two-dimensional PIC simulations

To be able to study also the effect of self-bias a two-dimensional r-z PIC code is used to simulate a capacitively coupled rf discharge.

To realize an asymmetric discharge the size of the powered electrode is set smaller than the size of the grounded electrode. In an asymmetric discharge the high mobility of the electrons charges the powered electrode, which then gets a negative self-bias voltage. The self-bias voltage is implemented using experimental values as an dc-offset of the rf-voltage at the powered electrode. This approach fulfills the flux balances [13] self-consistently.

To realize the parameters of the experiment, which uses electrode radii of a few centimeters, a powered electrode with a radius of 1.5 cm and an grounded electrode with a radius of 4.5 cm is used in the model and a grounded box is put around it. The electrode gap is about 2.5 cm. Due to the asymmetric distributions of the total currents to the walls and electrodes a negative self-bias voltage at the powered electrode according to the experimental values is added.

In Figure ?? the negative ion number density is shown for pressures of 10 Pa and 6 Pa with an applied rf voltage of 800 V_{pp} . One can see that the bulk region is deformed at the powered electrode side due to the self-bias voltage of 200 V_{sb} leading to a reduced electron flux towards the powered electrode.

There is a higher flux of positive ions towards the powered electrode than to the grounded electrode due to the self-bias voltage. In this one-dimensional simulation the total ion flux towards the powered electrode and the powered electrode sheath width are underestimated, because no self-bias can exist. There are other approaches like voltage waveform tailoring [14,15] or spherical 1d codes [16] to simulate self-bias voltages, but here we stick to a mono frequency approach. Still, the form of the number density distributions is nearly the same, which shows that a one-dimensional simulation is a good approximation near the center.

A special interest exists to study the energy distributions, especially of the negative ions, while applying the former model of SIE. Following the argumentation of the one-dimensional model the injected anions should not be able to stay in the discharge, due to the additional energy from the self-bias voltage (see Fig. ??).

The secondary negative ions, which do not collide or get detached in the bulk, obtain enough energy from the self-bias voltage to cross the grounded electrode sheath and impinge on the grounded electrode. This explains the discrepancy in the one-dimensional model, which is lacking this physics and is therefore not able to reproduce the experiment.

Calculating the negative ion EDF at the grounded electrode, one can compare the results with the experiment. In Figure ?? the same high energetic peak shows up as in the experiment. This supports the idea that the observed high energetic peaks in the EDF of the negative ions at the grounded electrode are produced by surface effects at the powered electrode.

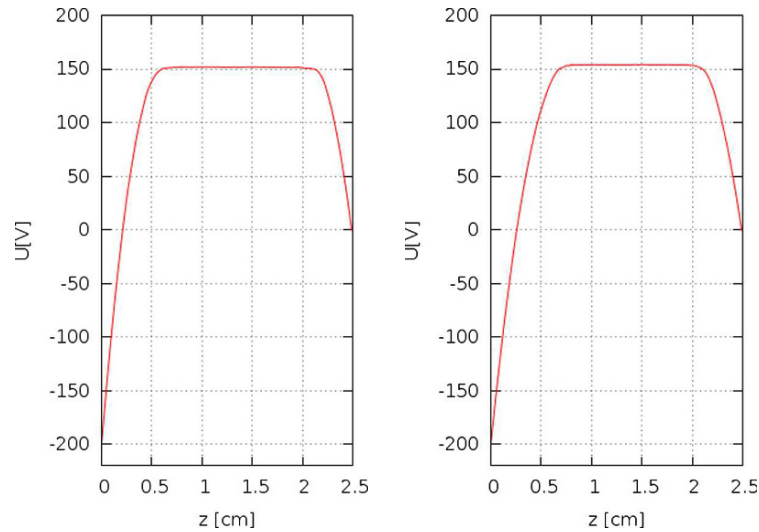


Fig. 7. Averaged Potential with self-bias voltage at the powered electrode shown along the axis at 10 Pa (left) and 6 Pa (right). The powered electrode is located at $z = 0$ cm.

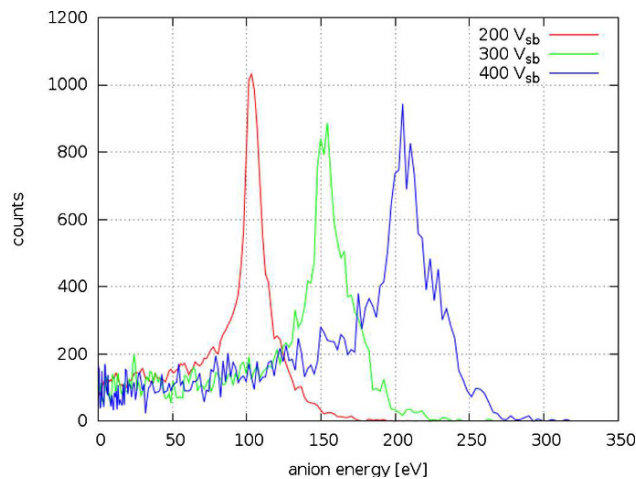


Fig. 8. Negative ion velocity distribution at the grounded electrode at 4 Pa and 800 V_{pp} with different self-bias voltages.

6 Summary

In this work 1D and 2D PIC-MCC models were used to simulate electronegative ccrf discharges with oxygen as process gas. The 1D simulations demonstrate the importance of elastic collisions for surface anions which leads to an energy loss and a continuous plateau in the energy distribution function. However, the 1D model lacks the possibility to study the influence of self-bias. Therefore, 2D simulations were done including the experimental self-bias and geometrical asymmetries. The results support the hypothesis that the high energy peak in the measured energy distribution function of negative ions at the grounded electrode originates from secondary negative ions created at the surface.

In the future the 2D PIC simulation can be used to study further aspects of asymmetric electronegative discharges, e.g. introducing complex sputter models. This will also allow to apply it to industrial applications like etching for a more detailed microscopic description.

Support from the Deutsche Forschungsgemeinschaft through Project No. B5 and No. B10 of the Transregional Collaborative Research Center SFB/TRR 24 is greatly acknowledged.

Author contribution statement

The experimental measurements were performed by JM. The code was developed by KM and further designed by RS, PM, SK, KFL, DK, JD and GB. All authors contributed to the conceptual design of the work, participated in the discussion of the results, provided valuable comments, and contributed to the revision of the manuscript.

References

1. U. Cvelbar, M. Mozetic, M. Klansjek-Gunde, *IEEE Trans. Plasma Sci.* **33**, 236 (2005)
2. M. Zeuner, H. Neumann, J. Zalman, H. Bidermann, *J. Appl. Phys.* **83**, 5083 (1998)
3. J.T. Gudmundsson, B. Ventéjou, *J. Appl. Phys.* **118**, 153302 (2015)
4. E. Stoffels, W.W. Stoffels, G.M.W. Kroesen, *Plasma Sources Sci. Technol.* **10**, 311 (2001)
5. H. Kawano, F.M. Page, *Int. J. Mass Spectrom. Ion Phys.* **50**, 1 (1983)
6. I. Korolov, A. Derzsi, Z. Donkó, E. Schlünger, J. Schulze, *Plasma Sources Sci. Technol.* **25**, 015024 (2016)
7. J. Meichsner, M. Schmidt, R. Schneider, H.-E. Wagner, *Nonthermal plasma chemistry and physics* (CRC Press, Boca Raton, Florida, 2013)

8. D. Tskhakaya, K. Matyash, R. Schneider, F. Taccogna, *Contrib. Plasma Phys.* **47**, 563 (2007)
9. J.T. Gudmundsson, E. Kawamura, M.A. Lieberman, *Plasma Sources Sci. Technol.* **22**, 035011 (2013)
10. K. Matyash, R. Schneider, F. Taccogna, A. Hatayama, S. Longo, M. Capitelli, D. Tskhakaya, F.X. Bronold, *Contrib. Plasma Phys.* **47**, 595 (2007)
11. F.X. Bronold, K. Matyash, D. Tskhakaya, R. Schneider, H. Fehske, *J. Phys. D: Appl. Phys.* **40**, 6583 (2007)
12. C. Küllig, J. Meichsner, K. Dittmann, *Phys. Plasma* **19**, 73 (2012)
13. Z. Donkó, J. Schulze, B.G. Heil, U. Czarnetzki, *J. Phys. D: Appl. Phys.* **42**, 25205 (2008)
14. E. Schüngel, I. Korolov, B. Bruneau, A. Derzsi, E. Johnson, D. OConnell, T. Gans, J.-P. Booth, Z. Donkó, J. Schulze, *J. Phys. D: Appl. Phys.* **49**, 265203 (2016)
15. A. Derzsi, T. Lafleur, J.-P. Booth, I. Korolov, Z. Donkó, *Plasma Sources Sci. Technol.* **25**, 015004 (2016)
16. M.A. Liebermann, A.J. Lichtenberg, *Principles of plasma discharges and materials processing* (John Wiley & Sons Inc., Hoboken, New Jersey, 1994)



Similarity scaling-application and limits for high-efficiency-multistage-plasma-thruster particle-in-cell modelling

Paul Matthias¹ | Daniel Kahnfeld¹ | Stefan Kemnitz² | Julia Duras³ |
Norbert Koch⁴ | Ralf Schneider¹

¹Institute of Physics, University of Greifswald, Greifswald, Germany

²Institute of Computer Science and Technology, University Rostock, Rostock, Germany

³Department Application Software, German Climate Computing Centre, Hamburg, Germany

⁴Department of Applied Mathematics, Physics and Humanities, Nuremberg Institute of Technology, Nürnberg, Germany

Correspondence

Paul Matthias, Institute of Physics, University of Greifswald, Felix-Hausdorff-Str. 6, D-17489 Greifswald, Germany.
Email: matthiasp@uni-greifswald.de

Funding information

German Space Agency DLR, Grant/Award Number: 50RS1510

Abstract

To suit a wide variety of space mission profiles, different designs of ion thrusters were developed, such as the High-Efficiency-Multistage-Plasma thrusters (HEMP-T). In the past, the optimization of ion thrusters was a difficult and time-consuming process and evolved experimentally. Because the construction of new designs is expensive, cheaper methods for optimization were sought-after. Computer-based simulations are a cheap and useful method towards predictive modelling. The physics in HEMP-T requires a kinetic model. The Particle-in-Cell (PIC) method delivers self-consistent solutions for the plasmas of ion thrusters, but it is limited by the high amount of computing time required to study a specific system. Therefore, it is not suited to explore a wide operational and design space. An approach to decrease computing time is self-similarity scaling schemes, which can be derived from the kinetic equations. One specific self-similarity scheme is investigated quantitatively in this work for selected HEMP-Ts, using PIC simulations. The possible application of the scaling is explained and the limits of this approach are derived.

KEYWORDS

electric propulsion, low-temperature plasma, similarity laws, simulation

1 | MOTIVATION

Because of their high efficiency, electric propulsion devices are attractive for modern space missions. By using different designs of plasma thrusters, many different mission profiles can be fulfilled. The High-Efficiency-Multistage-Plasma Thruster (HEMP-T), developed by Thales Deutschland GmbH,^[1] is an ion thruster concept with a wide operational range and high long term efficiency.^[2] Because developing and building prototypes of new thruster designs is expensive, simulations are used to improve the knowledge of the physical processes inside of ion thrusters. HEMP-T require a kinetic model because the mean-free path of the plasma particles are comparable with the system size. Particle-In-Cell (PIC) models have proven to be an effective tool for the simulation of plasma thrusters.^[3,4] Until today, it is not possible to

This is an open access article under the terms of the Creative Commons Attribution License, which permits use, distribution and reproduction in any medium, provided the original work is properly cited.

© 2020 The Authors. *Contributions to Plasma Physics* published by Wiley-VCH Verlag GmbH & Co. KGaA

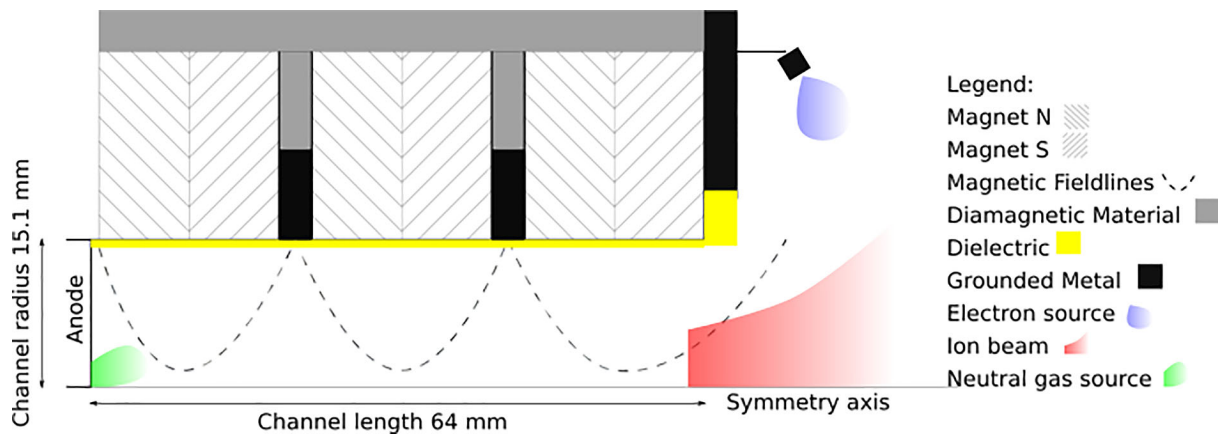


FIGURE 1 Schematic setup of the HEMP-T-DP1

use them for full predictive modelling, since all relevant time and space scales have to be resolved, namely, the electron plasma frequency and Debye length, respectively. This leads to large domain sizes and hence high computational demands. These practical run time limits are a problem and code optimization is necessary. Analysing the Boltzmann equation, a self-similarity scaling scheme can be derived,^[5] which can then be used to decrease the amount of computing time needed for PIC. The aim of this work is to evaluate the similarity scaling scheme for PIC simulations of HEMP-Ts and to study limits and deviations caused by the scaling, quantitatively. The specific system used for this is the HEMP-T DP1 thruster,^[6] which is described in the next section. Afterwards, the similarity scaling scheme is derived and discussed. With a miniaturized DP1 system (the TDP1) similar to the μ HEMP-T,^[7] the validity of the analytically derived similarity scaling scheme is shown. This verification is accomplished through various TDP1 simulations with different scaling factors and analysis of the deviations of key plasma properties. Then, the results are investigated from PIC simulations of the DP1 thruster with different similarity scaling factors. Since the DP1 is larger than the TDP1, higher similarity scaling factors have to be applied due to run time restrictions. These illustrate the limits of the self-similarity scaling approach. Finally, a summary and an outlook are given.

2 | THE HIGH-EFFICIENCY-MULTISTAGE-PLASMA-THRUSTER

The High-Efficiency-Multistage-Plasma-Thruster (HEMP-T) is an ion thruster developed by THALES Deutschland GmbH.^[1] A magnetic multi-cusp arrangement surrounds the thruster channel of the HEMP-T with subsequent axially magnetized permanent magnet rings with opposite polarization. The discharge channel is coated with a dielectric with a high sputtering threshold, such as boron nitride. Anode and neutral gas inlet are placed at the upstream end of the channel. Usually xenon is used as operating gas, due its high mass and low reactivity. Outside of the channel an electron source, representing the cathode, serves as a neutralizer for the emitted ion beam and an electron source for the plasma discharge in the channel. The high magnetic field strength of up to ~ 0.5 T leads to a magnetization of the electrons, resulting in Larmor radii much smaller than the channel diameter. Ions are not magnetized because of their higher mass. The cusp-like structure of the magnetic field resembles a magnetic mirror towards the dielectric wall in some channel regions. It reflects electrons impinging on the dielectric and thus traps them inside the thruster channel between the cusps. This trapping of electrons in the discharge channel results in high ionization rates. Another advantage of the cusp structure is the low plasma wall contact, which is limited to the cusps, resulting in very low sputtering yield rates. This leads to a long lifetime and a high efficiency of the thruster. The magnetic field enhances axial transport of the electrons in the channel which results in a flat potential structure. At the channel exit, the potential drops to vacuum level, accelerating the emitted ions and hence generating the thrust.

This work considers the thruster design HEMP-T-DP1 (short DP1), developed by Koch et al.^[6] Figure 1 shows a sketch of the DP1. The discharge channel is 64.0 mm long and has a radius of 15.1 mm. The magnetic circuit consists of three magnet rings with different lengths, resulting in a three-cusp magnetic field configuration. In the channel, the cusps are located at axial positions of about 15 and 30 mm, respectively. The last cusp is located at the channel exit. At

the bottom of the discharge channel (left side in Figure 1), the anode is located with an applied voltage in a range of 100–2,000 V. The neutral gas inlet is placed at the centre of the anode. Xenon is used as the propellant gas with injection fluxes between 10–30 sccm.

To better understand the scaling of the physics of the low temperature plasma in the HEMP-T, the fundamental kinetic equations are used to derive a scaling scheme in the next section.

3 | SCALING LAWS IN PLASMA PHYSICS

A plasma is described by the distribution function for each particle species s in space, velocity, and time $f_s(\mathbf{r}_s, \mathbf{v}_s, t)$. The time evolution for one species is given by the Boltzmann equation

$$\frac{\partial f_s}{\partial t} + \mathbf{v}_s \frac{\partial f_s}{\partial \mathbf{r}_s} + \frac{\mathbf{F}_s}{m_s} \frac{\partial f_s}{\partial \mathbf{v}_s} = \left. \frac{\partial f}{\partial t} \right|_{\text{coll}}, \quad (1)$$

with the force \mathbf{F}_s acting on a particle with the mass m_s and the collision term $\left. \frac{\partial f}{\partial t} \right|_{\text{coll}} = 0.0001 p t_{\text{coll}}$. In electromagnetic systems, \mathbf{F}_s is the Lorentz force. If the particle density is small, the collision term can be neglected and the Boltzmann equation simplifies to the Vlasov equation.^[8] The dynamics of a collisionless plasma is then fully described by the coupled system of the Vlasov and Maxwell equations.

Two systems are called similar if all physical quantities of both systems obey a scaling law which relates them through a similarity scaling factor ξ , e.g. the length $x = \xi \cdot \tilde{x}$. The tilde indicates the quantities of the scaled system in all following descriptions. The scaling laws for the physical quantities are derived from the invariants of the Maxwell-Vlasov system for collisional plasmas, which were derived by Lacina et al.^[9] The five invariants

$$C_1 = \frac{m_s v_s^2}{q_s E x}, \quad C_2 = \frac{m_s v_s}{q_s B x}, \quad (2)$$

$$C_3 = \frac{m_s n_s v_s^5}{E^2}, \quad C_4 = \frac{m_s n_s v_s^5}{B^2}, \quad (3)$$

$$C_5 = \frac{x}{v_s t}, \quad (4)$$

have to be conserved by the scaling scheme. Here, E is the electric field, B is the magnetic field, t is the time, m is the particle mass, q is the particle charge, v is the particle velocity, and n is the particle number density for each plasma species s . C_1 and C_2 are the invariants of trajectories in the electric and magnetic field. C_3 and C_4 describe the invariants of the self-induced electric and magnetic fields generated by internal currents. C_5 describes the similarity of a nonstationary process. Of special interest in a magnetized low-temperature plasma is the invariant C_2 , also called the Hall parameter

$$C_2 = \beta_{\text{Hall}} = \frac{r_g}{x} = \frac{m_e v_{e,\perp}}{e B x} = \text{const}, \quad (5)$$

which relates the gyro motion r_g to the system dimensions L . Additionally, the scaling of the trajectories in electric fields C_1 and the evolution of trajectories in time C_5 have to be conserved. In HEMP-Ts magnetic fields induced by the plasma currents are small compared to the externally applied magnetic fields. Therefore, an electrostatic approximation is valid for the simulation of ion thrusters. As a result, the invariants C_3 and C_4 can be neglected.

For ion thrusters, collisions have to be considered and therefore it is important to look for further invariants of the system. Applying binary collisions to the Boltzmann equation one can derive a sixth invariant,^[9]

$$C_6 = \frac{\lambda}{x}, \quad (6)$$

where λ is the mean free path. The expression from Equation (6) represents the Knudsen number Kn , relating the mean free path λ to the system dimension x . This results in a total of four different scaling constants (C_1, C_2, C_5, C_6), which have to remain invariant in a similarity scaling scheme for the low-temperature plasmas in ion thrusters. To derive the scaling approach most valid for PIC simulations, the PIC model is explained first in the next section.

4 | THE PIC METHOD

The PIC method is used for simulating low-temperature plasmas with non-Maxwellian distribution functions.^[10,11] Due to the axial symmetry and the negligible influence of self-induced magnetic fields in the DP1, the used PIC-MCC code is an axisymmetric, electrostatic 2D3v PIC code operating in cylindrical coordinates (r, z) . All three dimensions of the velocity space (v_r, v_z, v_t) are resolved to preserve energy and momentum in the collision algorithms. In regions where the electric field is perpendicular to the magnetic field, like at the exit of the HEMP-T, an ExB drift occurs in plasmas. This drift of the electrons leads to a Hall current in the azimuthal direction, resulting in density and electric field gradients which then lead to instabilities. This greatly increases the cross-field mobility of the electrons at the exit. For Hall-Effect-Thrusters, the influence of the anomalous transport has been thoroughly studied.^[12] In the used 2D simulation the azimuthal coordinate is only resolved in the velocity space, therefore neglecting the possible density and electric field instabilities. This anomalous transport is implemented as a random walk in velocity space acting as a rotation of the velocity vector of the electrons. It directly scales with the local electric and magnetic field, using a Bohm-scaling. The implementation of the anomalous transport in the present simulation was derived by Kalentev et al.^[13] using 3D simulations.

In the simulations presented here, neutral xenon particles Xe, electrons e, and singly Xe⁺ and doubly charged xenon ions Xe²⁺ are included. The density of doubly charged ions is only a small fraction (<10%) of the singly charged ions. Because the fraction of higher charge states less than 1% combined to the total number of ions, they are neglected.^[14] The Coulomb collisions are handled as described by Takizuka and Abe.^[15] Also included in this simulation are direct single and double e-Xe impact ionization, single e-Xe⁺ impact ionization, integral elastic Xe⁺-Xe collisions (including charge exchange and momentum transfer), and integral elastic and inelastic e-Xe collisions,^[13] using a binary collision model^[16,17] which utilizes experimentally measured collision cross section.^[18]

Further information on the PIC model used here can be found in previous publications.^[19,20]

4.1 | Similarity Scaling in PIC

PIC has to resolve the Debye length, which is several orders of magnitude smaller than the system dimensions, leading to large domain sizes in terms of the total number of cells required to cover the domain. Large domains result in high computing times for solving the Poisson equation and a high number of simulated particles, which again increases the work load for particle motion and collisions. To reduce the computational effort of PIC simulations, the following self-similarity scaling scheme is introduced, based on the plasma invariants discussed Section 3. Keeping the plasma density and hence the spatial resolution of PIC constant, which are determined by the Debye length, it is useful to reduce the system size by the similarity scaling factor ξ . This results in a scaling of the old domain length to $x = \xi \tilde{x}$ with $\xi > 1$ and thus in a reduction of the number of cells in the simulation with ξ^n , where n is the number of spatial dimensions of the PIC model. With the scaling constant of time evolution C_5 from Equation (4) it follows that the time is scaled as $t = \xi \tilde{t}$, to keep the particle velocity constant. The scaling of the domain size in combination with the resolution of the Debye length leads to a scaling of the cell volume relative to the system size with the scaling factor $\sim \xi^n$. To keep the number density constant, the number of super-particles in each cell has to be scaled, too. The scaling of the particle numbers is then applied to the super-particle factor, increasing the amount of particles represented by one super-particle and keeping the total amount of particles to be tracked low.

In HEMP-Ts, the motion of particles is determined by the magnetic and electric fields. The scaling of both fields follows from the derived plasma constants of Equation (2) and the scaling of the system length

$$E = \xi^{-1} \tilde{E} \text{ and } B = \xi^{-1} \tilde{B}. \quad (7)$$

Due to the electric field being scaled with ξ^{-1} , the electric potential Φ remains nonscaled. To preserve ionization and other collisions, which are vital for thruster operation, the plasma invariant for binary collisions C_6 from equation Equation (6) has to be considered. The mean free path is then scaled as $\lambda = \xi \tilde{\lambda}$ through scaling the collision cross sections σ

$$\frac{\lambda}{x} = \frac{1}{n\sigma\langle v \rangle x} = \text{const.} \quad (8)$$

$$\rightarrow \sigma = \xi^{-1} \tilde{\sigma}, \quad (9)$$

TABLE 1 The most important quantities in the self-similarity scaling scheme. A tilde indicates the quantities of the down scaled system. ξ is the similarity scaling factor

Quantity	Scaling law
Length scale	$x = x - \xi$
Time scale	$t = t - \xi$
Collision cross section	$\sigma = \tilde{\sigma} \xi^{-1}$
Magnetic field strength	$B = \tilde{B} - \xi^{-1}$
Electric field strength	$E = \tilde{E} - \xi^{-1}$
Potential	$\Phi = \tilde{\Phi}$
Super particle factor	$N_{sp} = \tilde{N}_{sp} \xi^3$
Number density	$n = \tilde{n}$
Super particle flux per unit area	$\Gamma_{sp} = \tilde{\Gamma}_{sp}$

for each collision process represented in the model, with the averaged velocity $\langle v \rangle$ and taking into account the other scaling laws. It is important to mention, that the numeric implementation of the anomalous transport is represented by a Bohm-like transport. The Bohm transport scales with the magnetic field, which scales with the self-similarity scaling factor. The anomalous transport is implemented according to the self-similarity scaling. A general overview of the resulting scaling scheme is given in Table 1.

One should note, that the presented scaling scheme is exact for all plasma volume processes, including particle trajectories, binary collisions, and even fluxes. But because the system size shrinks while the plasma density remains constant, the ratio of the Debye length λ_{Db} to the size of the scaled system changes

$$\frac{\lambda_{Db}}{\tilde{x}} \neq \text{const.} \quad (10)$$

The increased ratio leads to an overestimation of charge separation, which occurs on the scale of the Debye length. Especially, in regions with smaller Debye lengths, such as the plasma sheath or the exit region and plume of ion thrusters, the scaling overestimates the charge separation. When extrapolating the results from the down-scaled system to the real one, this leads to regions where quasi-neutrality is seemingly violated.

The plasma boundary sheath with a typical dimension of a few Debye lengths increases relative to system size L . This leads to a higher sheath to plasma volume ratio for higher scaling factors. The increased charge separation leads to longer decay lengths of the potential, increasing the influence of the potential boundary conditions for larger similarity scaling factors. As long as the sheath is small compared to the plasma volume the similarity scaling is an accurate model for the discharge, but has an upper bound of applicable similarity scaling factors. For HEMP-Ts this influence manifests mainly in the plume and at the thruster exit. Additionally, if three-body processes become important the scaling lacks accuracy, because only binary collisions are covered in this self-similarity scaling Scheme.^[9] This is usually not important for ion thrusters, but can be dominant in fusion edge plasmas.^[21]

The applicability of a scaling model was already shown for Hall thrusters by Taccogna et al.^[5] The scaling presented here is equivalent to the scaling of the vacuum permittivity ϵ_0 ^[22] or a scaling of the plasma density n_e , as was shown by Lacina.^[9] Multiple groups applied such a scaling scheme already in the past without discussing their limits, for example, to simulate spoke frequencies in a Penning discharge^[23,24] or to gain physical insights in Hall effect thrusters.^[22,25,26]

However, a quantitative study of the influence of the scaling factor on the results is missing. The aim of this work is to present a quantitative analysis of the influence of the self-similarity scaling scheme for the example of the HEMP-T system, including channel and plume solutions.

5 | RESULTS

To study the influence of the scaling factor on the system, the following strategy is pursued. At first, the PIC simulation setup of the DP1 thruster is described to introduce the considered thruster design. A verification study of the similarity scaling is then carried out for a smaller system, the Tiny-DP1 (TDP1). The simulation results from the TDP1

ξ	Domain size ($r \times z$)
60	157 × 493
70	134 × 422
80	117 × 370
90	104 × 328
100	94 × 297

TABLE 2 Domain size for PIC simulations of the DP1 in cell numbers in radial r and axial z direction for different similarity scaling factors ξ

are additionally used to describe the general characteristics of HEMP-Ts. Afterwards, the larger DP1 is used to study quantitative limits of the similarity scheme.

5.1 | Setup of the simulation

To cover the channel and the near-exit region of the DP1 the simulation domain measures 35×100 mm (r, z). With an expected charged particle density of 10^{13} cm^{-3} and an electron temperature of 10 eV, the spatial resolution $\Delta r = 3.7 \times 10^{-4}$ cm and temporal resolution $\Delta t = 2.8 \times 10^{-13}$ s are chosen. The target particle density is represented by six super-particles at the symmetry axis and increases linearly with radial distance. The anode potential is set to 500 V and the metal and the top domain boundary are set to ground potential, while the right domain boundary is set to an electric field of zero in axial direction to simulate a vacuum transition downstream. At the anode the neutral gas inlet is set to a mass flow rate of 15 sccm. An electron source is located at the right domain boundary, replacing the electron current from the neutralizer of the real system. The injected electron current is an input parameter for the PIC simulations. In ion thruster physics, the operation mode is defined by the anode current, beam current, and thrust. Higher electron source currents lead to higher plasma densities and thereby increase anode and beam current. Therefore, the strength of the electron source current is the parameter to generate different operational modes in thruster simulations, assuming a constant anode potential and neutral gas mass flow rate.

For the simulations of the DP1, an electron current of 360 mA is applied. The simulation domain is set up similar to Figure 1. The similarity scaling scheme introduced in Section 3 is applied to scale down the size of the simulated system and therefore decrease computing time. With increasing scaling factor, the number of cells in the domain decreases according to Table 2.

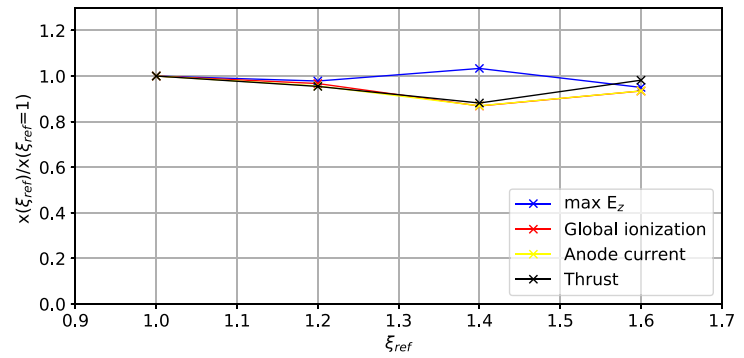
5.2 | Verification of the self-similarity scaling scheme with the TDP1

To verify the similarity scaling scheme, a new thruster design, in the following referred to as the TDP1, is introduced to be able to study small similarity scaling factors. It is geometrically similar to the DP1, but the geometric dimensions are reduced. The channel length of the TDP1 is 21.33 mm with a radius of 5.033 mm. Its magnetic field topology is similar to the magnetic field of the DP1. For the same plasma parameters as the DP1, the total number of cells in the simulation is reduced. The simulation with a low scaling factor represents the reference case from which the similarity scaling factor can be incrementally increased, which is used to verify the similarity scaling. The plasma solution characteristics should not vary strongly across the different scaling factors for the verification. In the Figures A1 and A2, the resulting electron and ion density distributions are shown for different scaling factors relative to the reference case in the range between $\xi_{\text{ref}} = 1 \dots 1.6$.

For discussion of the HEMP-T characteristics, the simulation of the reference case of the TDP1 thruster with $\xi_{\text{ref}} = 1$ is considered here. The results of the PIC simulation of the TDP1 thruster model show the same general behaviour as other HEMP-Ts, namely, a flat potential in the acceleration channel, a potential drop at the exit and the trapping of the electrons between the magnetic cusps. The electric potential, as shown in Figure A3 is flat in the thruster channel due to the high electron mobility, in particular close to the axis.

Typical for HEMP-Ts is the cusp structure leading to low plasma wall contact, which is limited to the cusp region. The electrons in the thruster are trapped between the cusps, which act as magnetic mirrors, enhancing the ionization of the neutral xenon gas, which can be seen in the electron density distribution in Figure A1. In addition, the ion energies at the

FIGURE 2 Behaviour of global values of the HEMP-T, namely the maximum electrical field at the exit (blue), the global ionization (red), the anode current (yellow) and the thrust (black), with rising scaling factor. The values are normalized by the values from $\xi_{ref} = 1$



cusps are so low that they are below the sputter threshold and produce very low sputtering rates at the channel wall.^[2] The magnetization of plume electrons at the exit cusp, leads to an additional plasma in front of the exit. Due to the magnetic field structure the electrons follow the magnetic field lines towards the axis and into the discharge channel. In the density gap between the plasma in the exit cusp and the acceleration channel the potential drops and the electrons are accelerated by the electric field upstream into the discharge channel. The ion density distribution in Figure A2 is similar to the electrons in the acceleration channel. At the exit, they are accelerated by the electric field and are then ejected into the plume to generate the thrust. All these results are typical for HEMP-Ts.^[2,27]

Because the TDP1 shows these typical characteristics of a HEMP-T, the aim is now to verify the self-similarity scaling scheme. Because the scheme is exact for volume processes and wall fluxes, only little impact on the plasma distribution in quasi-neutral regions of the discharge is expected, i.e. in the acceleration channel.

The evolution of the system is now shown for increasing similarity scaling factors in relation to the reference case. A very important constraint of the self-similarity scheme results from the additional influence of charge separation producing electric fields. This is determined by the Debye length, which changes relative to the system size and hence causes deviations from the reference case. For low similarity scaling factors the ratio of Debye length to system size does not increase much, leading to a conservation of the plasma solution by the similarity scaling. This is shown by comparing some of the bulk parameters at different scaling factors, shown in Figure 2. Afterwards, the maximum of the electric field is determined at the exit. For the global ionization, the ionization collision rates are integrated over the whole channel volume. The anode current is obtained by integrating the axial particle flux crossing the left domain boundary and converting them into an electric current by multiplying with the correspondent particle charge and divide by the time step. The thrust is calculated by summation of the axial momentum of the emitted ions. For better statistics the data is averaged over 10^6 time steps of a converged simulation, which is equal to 1.68×10^{-5} s in the scaled system. The averaging time covers all relevant transport processes in the system.

In Figure 2, it can be seen, that the maximum electric field at the thruster exit, which is responsible for the acceleration of emitted ions, stays nearly constant over the considered range of scaling factors. The same behaviour is observed for the global ionization, the anode current and the thrust of the TDP1. These selected parameters are representative for the global thruster solution and show that the similarity scaling conserves the solution for small scaling factors.

To further study the similarity scaling scheme, the time averaged axial electron density profile in the channel at $r = 4$ mm is shown in Figure 3 for different scaling factors. It shows the increase of density at the cusp, the electron density of trapped electrons between the cusps and the density drop at the exit of the thruster. All density profiles have a similar shape, with variations of the total values of up to 30%, which can be explained by the slight variations of the global ionization, see Figure 2.

The channel solution in front of the potential drop is similar for the applied scaling factors as long as the influence of the charge separation in the plasma sheath remains small. This limit is violated for large scaling factors when the radial sheath approaches the radial diameter of the channel, similar to systems such as the μ HEMP-T.^[7] In small systems with an already high ratio of Debye length to system size this limit is reached with already comparably small scaling factors. Therefore, the similarity scaling factor is not the correct parameter to decide if realistic solutions are possible. Another parameter to be considered is the ratio of Debye length to scaled system size

$$\tilde{\zeta} = \frac{\lambda_{Db} \xi}{L}, \quad (11)$$

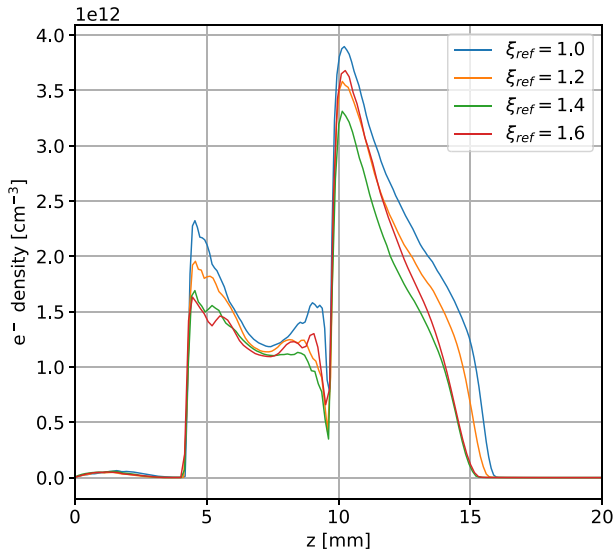


FIGURE 3 Comparison of axial electron density profile in the channel at $r = 4$ mm for different scaling factors. The scaling factors are set in relation to the reference case of $\xi_{ref} = 1$

which allows a better estimate of limits of the applied scaling. The TDP1 shows relatively small variations for the most important parameters (see Figure 2) under the application of the similarity scaling scheme on a scale of $\tilde{\xi} = 0.066 - 0.12$. It is important to note that the limit, where one considers the scaling to produce too strong deviations, depends on the question to be addressed. In qualitative studies deviations of up to 50% can be sometimes acceptable, whereas for specific design studies even deviations of 10%, e.g. of thrust, can be too large. In general, deviations of several 10% can be still considered acceptable, given other uncertainties in designs.^[28] The scaling is limited by simulations, where the sheath covers the whole radius of the thruster channel, which leads to unexpected and physically not correct behaviour. Some of these limits of the similarity scaling can be found in the work from Brandt et al.,^[7] where a down-scaled HEMP-T is discussed.

Now, the influence of larger scaling factors on a large system, but in a similar range of $\tilde{\xi}$ is studied.

5.3 | Quantitative self-similarity scaling study for the DP1

The larger DP1 system is now used to study the influence of the applied similarity scaling on the PIC results. The size of the DP1 leads to run-time restrictions for the PIC calculations. Therefore, high similarity scaling factors have to be applied to stay within reasonable computing times of weeks. Full PIC simulations of the DP1 for scaling factors in the range from $\xi = 60$ to $\xi = 100$ were performed, which results in different sized domains as listed in Table 2. For completeness, the density distributions and potential solutions can be found in the Appendix A. Since the self-similarity scheme is exact for volume processes and wall fluxes, only little impact on the plasma distribution in quasi-neutral regions of the discharge is expected, especially in the acceleration channel in front of the potential drop.

In the plasma density distribution in Figure B1 can be seen, that most of the channel distribution between anode and potential drop is unchanged by the applied scaling Scheme. As expected, a difference appears close to the exit region, where the plasma contracts further towards the inner channel with a higher scaling factor.

This behaviour is generated due to the different decay length of the grounded domain boundary conditions in addition to the overestimated charge separation because of the increased Debye length relative to the system size with increased similarity scaling factor. With higher scaling factors the grounded potential from the metal at the thruster exit extends further, since the relative distance in terms of Debye lengths between the boundary and the plasma is smaller. This pushes the potential drop further into the channel, resulting in a decreased plasma bulk volume.

In Figure 4 a comparison of the electron density distribution in the channel is shown for two different scaling factors of $\xi = 60$ and $\xi = 100$. Most of the channel distribution is unchanged by the applied scaling scheme. As expected, a difference appears close to the exit region, where the plasma contracts further towards the inner channel with a higher scaling factor.

The decrease of the plasma volume in the exit region, see Figure B1, leads to reduced ionization in the plume and decreased ionization at the exit cusp with increasing similarity scaling factors. The dependence of the ionization current

FIGURE 4 Comparison of electron density distribution in the discharge channel of the DP1 between different similarity scaling factors, (top) $\xi = 60$ and (bottom) $\xi = 100$

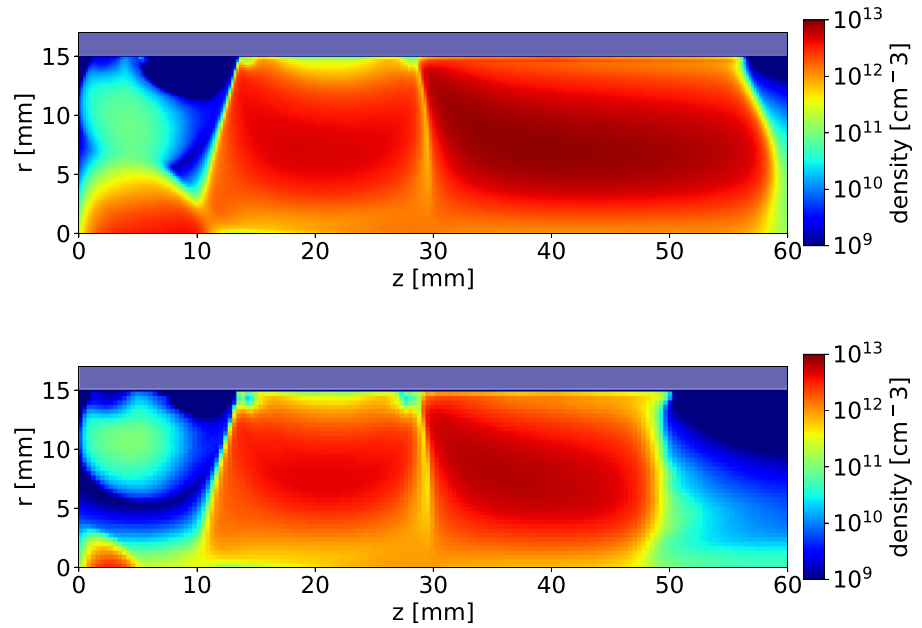
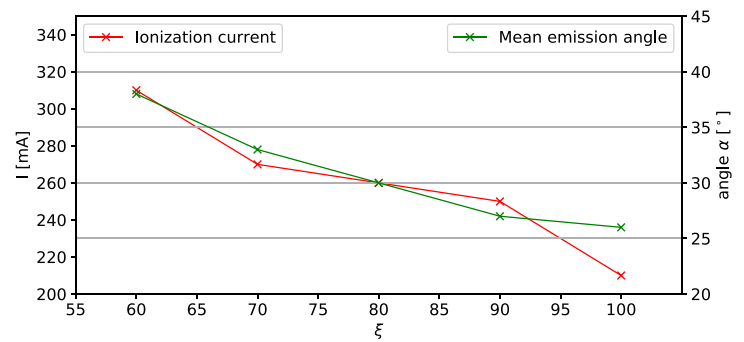


FIGURE 5 Mean emission angles α and ionization currents at the exit in the range $z = [40 \text{ mm}, 75 \text{ mm}]$ for different scaling factors



on the similarity scaling factor is shown in Figure 5. Less ionization leads to a lower plasma source for the channel plasma, which decreases the effective plasma volume and density. In front of the anode the electron density decreases with rising scaling factor. This is due to the already discussed decrease of plasma volume and density. Because of less electrons in the discharge, less electrons reach the anode region and lead to a lower electron density in the pre-anode region. In comparison to the main ionization areas in the DP1, namely, between the two cusps in the middle ($z = 15\text{--}30 \text{ mm}$) and between the second cusp and the exit ($z = 30\text{--}50$), the changes in the anode region have only little impact on the overall plasma solution. Other plasma parameters in the thruster channel, such as thermal and excitation losses, remain nearly constant with the variation of the scaling factor. This demonstrates again the physical accuracy of the chosen self-similarity scaling scheme for volume process and wall flux dominated plasmas, where the charge separation on the Debye scale relative to the system size is not dominating the behaviour with increasing scaling factor the mean emission angle drops (Figure B2).

Now, the changes in performance parameters for different scaling factors are investigated. Thruster performance is mainly defined by the anode I_a and beam current I_b , the thrust T and the beam efficiency $\eta_{\text{beam}} = I_b / em_{\text{source}}$ at a given neutral gas mass flow rate \dot{m}_{source} . Especially, the ion angular current distribution is important and accessible experimentally using a Retarding-Potential-Analyser (RPA).^[2] The mean emission angles of the ion angular current distributions for different scaling factors are shown in Figure 5. With increasing scaling factor the mean emission angle drops (Figure B2). This leads to a higher thrust contribution of the ions due to a smaller ratio of radial to axial momentum because only the latter contributes to the thrust. To explain the drop of the mean emission angle, one has to take into account the potential solution.

In Figure 6, axial potential profiles at the axis and radial potential profiles at the exit are shown. The axial potential at the exit ($z = 50 \text{ mm}$) is nearly at anode potential and drops downstream from the exit until it reaches vacuum potential.

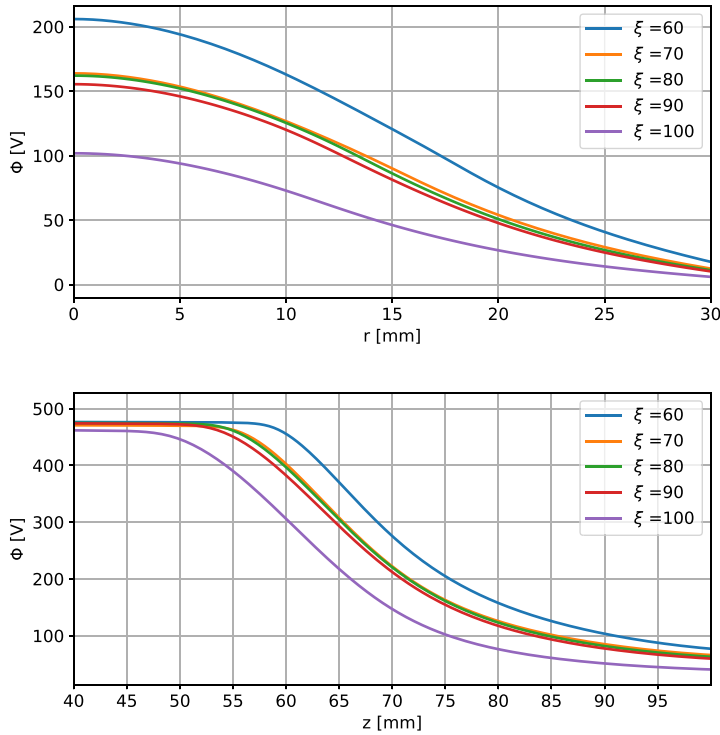


FIGURE 6 Potential profiles of the DP1 for different scaling factors. (*Top*) radial profile at the exit at $z = 75$ mm and (*bottom*) axial profile in the exit region at the axis $r = 0$ mm

Scaling factor ξ	Thrust (T)	I_A (mA)	I_B/I_A	$\bar{\alpha}_{\text{exit}}$ ($^\circ$)	η_{beam} (%)
60	18.2	851	0.9	38	71
70	17.4	777	0.9	33	65
80	17.3	756	0.9	30	63
90	17.3	747	0.9	27	61
100	14.7	640	0.9	26	53

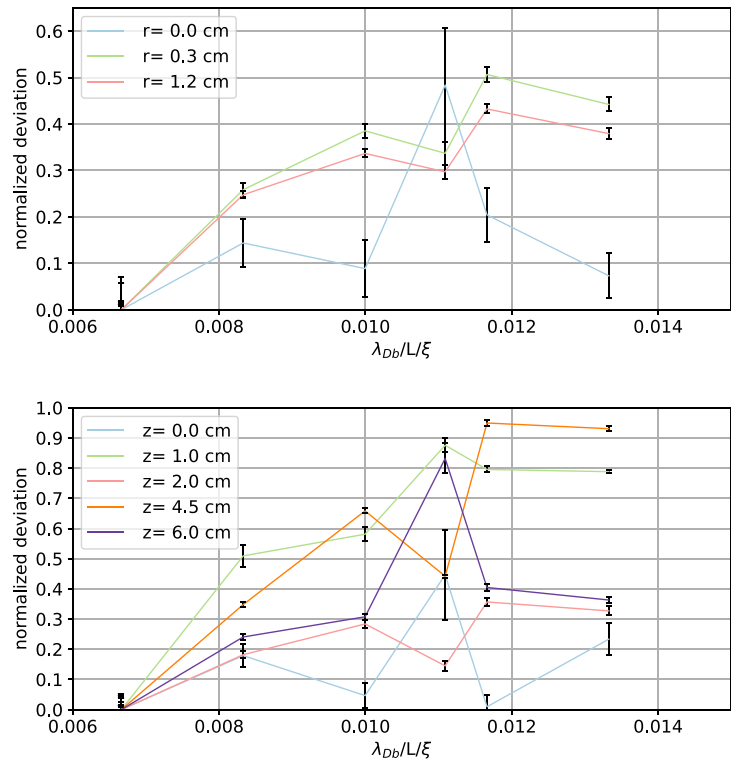
TABLE 3 Comparison of the operational parameters thrust T , anode current I_A , beam current I_B , mean emission angle $\bar{\alpha}_{\text{exit}}$ and beam efficiency η_{beam} for the DP1 using different self-similarity scaling factors

For reference see also Figure B3, where the full potential solutions are shown. With increasing scaling factor the plasma contracts, due to the increasing influence of the grounded metal at the thruster exit as discussed before. In addition, the increased charge separation creates lower electric fields at the exit, leading to reduced ionization processes in the exit region. This trend is visible also in the global ionization current, see Figure 5, which also decreases with rising scaling factor. The contracted plasma and the decreased potential in the exit region, as shown in Figure 6, draw the potential drop further into the thruster. This contracted potential profile decreases the radial potential drop (Figure 6) outside of the thruster exit leading to lower radial electric fields. Therefore, the ions receive less radial momentum which leads to a decrease of the main emission angle of the exiting ions. The change of the ion angular beam current leads to the effect that the same electron source current does not represent the same operating state for different scaling factors because of the change in the plasma density distribution.

In Table 3, the most important parameters defining the operation state calculated from the PIC simulations of the DP1 are listed for different scaling factors. In summary, the beam divergence is reduced with increasing scaling factors, increasing the contribution to the thrust of the ions due to lower emission angles. The decreasing plasma bulk volume and hence the decrease of the ion density volume compensates the decreasing emission angle, so that the thrust of the DP1 stays nearly constant for different scaling factors, except for the highest scaling factor $\xi = 100$, where it drops sharply. The reduced ionization leads to a reduced beam current and therefore to a decreasing beam efficiency η_{beam} of the thruster.

For practical applications, the limit for scaling factors is important, which is determined by the ratio of the Debye length to the scaled system size. As already mentioned, this range changes with the system size of the considered device, because higher scaling factors can be applied to bigger thrusters. To compare different system sizes, the following physical

FIGURE 7 The absolute deviation of the volume integrated electron density. (*Top*) Axial variations from anode to thruster exit and (*bottom*) radial variations from axis to the dielectric of the channel are shown in dependence of the ratio $\tilde{\xi}$ of Debye length λ_{Db} to scaled system size



properties are shown in dependence of the ratio $\tilde{\xi}$ of the Debye length to the scaled system size ($\lambda_{Db}/[L/\xi]$). General important volume integrated properties such as electron density, potential and ionization collision rates are representative for the thruster solution and are shown in Figures 7–9. The characteristic system size is defined, without loss of generality, as the thruster channel length.

The averaged data d is subtracted and then normalized by the values from the simulation with the lowest scaling factor ξ_0 for either DP1 and TDP1, resulting in the absolute deviation $\tilde{d}(\xi)$

$$\tilde{d}(\xi) = \frac{|d(\xi) - d(\xi_0)|}{d(\xi_0)}. \quad (12)$$

As discussed above, the biggest changes to the plasma properties are expected close to the exit, where the influence of the space charge should be the strongest. To identify this effect, the channel is divided into different characteristic volumes. In each of Figures 7–9, the upper figure represents axial cuts, representing the volume at the axis ($r = 0$ – 0.3 cm), in the centre of the discharge ($r = 0.3$ – 1.2 cm) and the sheath towards the dielectric ($r = 1.2$ – 1.4 cm). The figures at the bottom depict radially oriented slices, representing the anode area ($z = 0$ – 1 cm), the first cusp ($z = 1$ – 2 cm), the second cusp ($z = 2$ – 4.5 cm), the exit region ($z = 4.5$ – 6 cm) and the plume region ($z = 6$ – 10 cm).

From Figures 7–9 one can see that the scale of the relative deviation is different, showing that the axial cuts show in general lesser variations than the radial cuts. But with increasing ratios $\tilde{\xi}$, the deviations increase for all considered properties. Especially the radial cuts which cover the exit region show strong deviations with increasing ratio of Debye length to the scaled system size.

When comparing the different plots, it is apparent that the rate of the increase of the deviation rises sharply, when the ratio of Debye length to scaled system size gets bigger than 0.01. For lower ratios the deviations from the simulation at a ratio of 0.006, are lower than 20–30%, which usually can be considered to be sufficient for design studies.^[28]

As a consequence for the DP1 and the TDP1, the scaled channel length should be at least 100 times larger than the Debye length, while the channel radius should be at least 20 times larger than the Debye length. This can be considered as a general guideline, at least for the considered thruster design.

The results in this section demonstrate that the similarity scaling factor influences the results of the PIC simulations mostly in the thruster exit region. One expects the simulation with a scaling factor of 1 to be the best representation

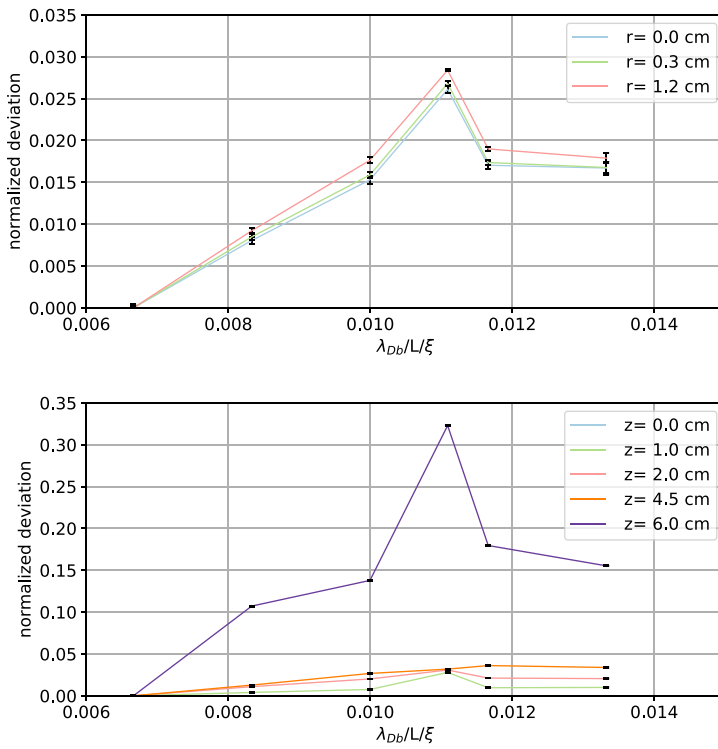


FIGURE 8 The absolute deviation of the volume integrated electric potential. (Top) Axial variations from anode to thruster exit and (bottom) radial variations from axis to the dielectric of the channel are shown in dependence of the ratio $\tilde{\xi}$

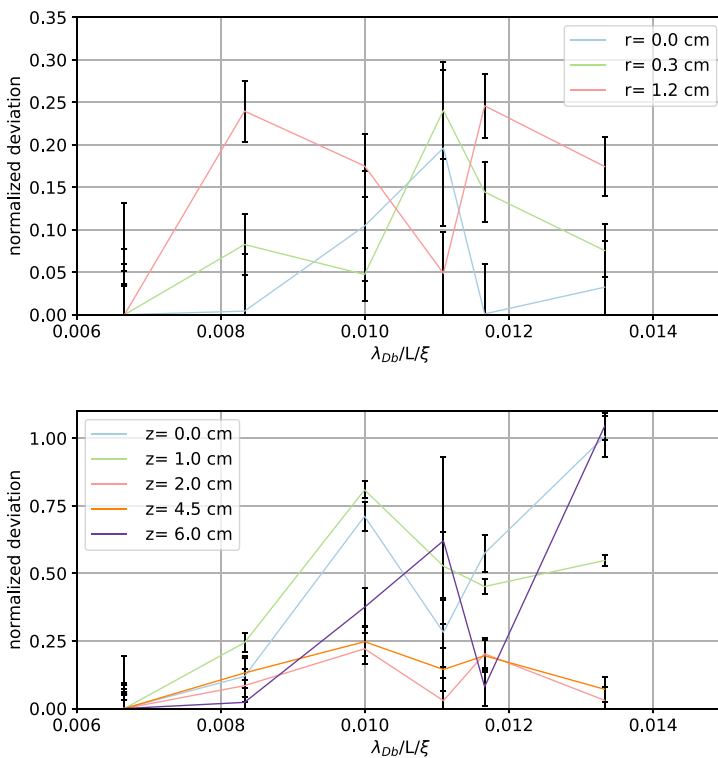


FIGURE 9 The absolute deviation of the volume integrated ionization processes. (Top) Axial variations from anode to thruster exit and (bottom) radial variations from axis to the dielectric of the channel are shown in dependence of the ratio $\tilde{\xi}$

of the experiment. In the present PIC studies, it shows that with increasing similarity factor the mean emission angle decreases, which in the contrary leads to higher emission angles at lower scaling factors. But in comparable HEMP-Ts, the experiment measures small emission angles $\sim 30^\circ$.^[2] This creates a mismatch of PIC and experiment, because PIC simulations with similarity scaling factors already tend to overestimate the emission angle of HEMP-Ts compared to the experiment.^[29] As shown in Figure 5, the ionization rate at the exit changes with scaling factor. The position of the potential drop reacts to this and affects the ion dynamics being accelerated into the plume. This changes the emission angle. In general, the exit region and the plume, which are influenced by the potential and charge separation at the exit have to be handled with care. Here, a combination with other methods, such as hybrid codes, can overcome these problems.^[30] It is expected that for lower similarity scaling factors the boundary conditions will have less impact on the plasma solution, as shown for the TDP1.

6 | CONCLUSIONS AND OUTLOOK

In this work, principles and limits of a self-similarity scaling scheme applied to PIC simulations of HEMP-Ts simulations are shown. The aim of this scheme is the reduction of the computing time of PIC simulations, at the cost of an increased ratio of Debye scale to system size. For the investigation of the influence of the scaling factor, PIC results for two different thruster designs and different scaling factors were considered. First, the scaling scheme was verified with the smaller thruster design of the TDP1 thruster, which allowed the application of low scaling factors. It was found that the scaling scheme delivers nearly identical results in the plasma acceleration channel, including fluxes and ionization currents. However, simulations of a larger thruster, the DP1, demonstrated the influence of the potential boundary conditions and the overestimation of the charge separation for higher similarity scaling factors, which are responsible for the reduction of the plasma bulk volume in the exit region of the discharge channel. The contracted plasma bulk leads to a decreased potential at the thruster exit and hence to a decreased emission angle, while generating comparable amounts of thrust. It was shown that the scaling factor has a non-negligible impact on the beam divergence and thrust. Therefore, if predictive simulations are required, the simulation results have to be benchmarked against unscaled simulations. It was found that the ratio of electron Debye length to scaled system size can be used to estimate practical limits for the application of the similarity scaling. To generate similar potential solutions the down-scaled channel length should be at least 100 times larger than the Debye length, while the down-scaled channel radius should be at least 20 times larger the Debye length. For a better scaling of particle densities and volume ionization processes even stricter ratios have to be chosen. Similarity scaling is a powerful tool to reduce computation time. Simulations with high scaling factors can be taken as a new starting point for further simulations with lower scaling factors, since the initializing phase of PIC simulations until convergence is reached is quite time and resource consuming otherwise.

To overcome the changes in the plume region, different solutions can be applied in the future. A hybrid solution,^[30] where the electrons are treated as a collisionless fluid, could be a better representation since it is not influenced by charge separation on the Debye scale. However, the disadvantage of the hybrid method is the loss of the full kinetic information. Another method could be a more application-oriented approach, such as a Multi-Objective Design Optimization (MDO).^[31,32] Here, experimental measurements can be combined with simulation characteristics for design optimization. As shown in this work and in ref.,^[5] the solution of the acceleration channel in front of the potential drop does not change for different scaling factors, and thus, these plasma properties can be used for MDO, which is based on a zero-dimensional power balance equation system. With this approach a large design space can be explored, where the lack of physical accuracy is minimized with the insight gained from PIC, which promises a fast and robust tool for thruster optimization in the future.

ACKNOWLEDGMENTS

The work of P.M. and D.K. was funded by the German Space Agency DLR through Project 50RS1510.

REFERENCES

- [1] S. H. Kornfeld, G. J. Wegener, *filed June 26, 1998* **1999** (priority: Germany No. 198 28 704.6).
- [2] N. Koch, M. Schirra, S. Weis, A. Lazurenko, B. van Reijen, J. Haderspeck, A. Genovese, P. Holtmann, R. Schneider, K. Matyash, O. Kalentyev, presented at *32nd Int. Electr. Propulsion Conf.*, Sep **2011**, 11, 15.
- [3] R. Schneider, K. Matyash, O. Kalentev, F. Taccogna, N. Koch, M. Schirra, *Contrib. Plasma Phys.* **2009**, 49, 655.
- [4] R. W. Hockney, J. W. Eastwood, *Computer Simulation Using Particles*, Taylor & Francis, Inc., Bristol, PA **1988**.

- [5] F. Taccogna, S. Longo, M. Capitelli, R. Schneider, *Phys. Plasmas* **2005**, 053502.
- [6] N. Koch, J. Duras, D. Kahnfeld, P. Matthias, et al, in *Proc. 35th Int. Electric Propulsion Conf.*, **2017**.
- [7] T. Brandt, R. Schneider, J. Duras, D. Kahnfeld, F. G. Hey, H. Kersten, F. Jansen, C. Braxmeier, *Trans. Jpn Soc. Aeronaut. Space Sci. Aerospace Technol. Jpn* **2016**, 14, 235.
- [8] F. Chen, *Introduction to Plasma Physics and Controlled Fusion*, Heidelberg: Springer, **2015**.
- [9] J. Lacina, *Plasma Phys.* **1971**, 13, 303.
- [10] C. Birdsall, A. Langdon, *Plasma Physics via Computer Simulation*, Boca Raton, FL: CRC Press, **2004**.
- [11] R. W. Hockney, *Phys. Fluids* **1966**, 9, 1826.
- [12] T. Lafleur, S. Baalrud, P. Chabert, *Phys. Plasmas* **2016**, 23, 053502.
- [13] O. Kalentev, K. Matyash, J. Duras, *Contrib. Plasma Phys* **2014**, 54, 235.
- [14] G. Kornfeld, N. Koch, G. Coustou, in *Proc. 28th International Electric Propulsion Conf.*, **2003**.
- [15] T. Takizuka, H. Abe, *J. Comp. Phys.* **1977**, 25, 205.
- [16] K. Matyash, *Ph.D. Thesis*, University of Greifswald, **2003**.
- [17] V. Vahedi, G. DiPeso, C. K. Birdsall, M. A. Lieberman, T. D. Rognlien, *Plasma Sources Sci. Technol.* **1993**, 2, 261.
- [18] M. Hayashi, *Bibliography of Electron and Photon Cross Sections with Atoms and Molecules Published in the 20th Century—Xenon, NIFS-DATA-79*, NIFS, **2003**.
- [19] D. Tskhakaya, K. Matyash, R. Schneider, F. Taccogna, *Contrib. Plasma Phys.* **2007**, 47, 563.
- [20] D. Kahnfeld, J. Duras, P. Matthias, S. Kemnitz, P. Arlinghaus, G. Bandelow, K. Matyash, N. Koch, R. Schneider, *Rev. Mod. Plasma Phys.* **2019**, 3, 2367–3192.
- [21] P. J. Catto, D. A. Knoll, S. I. Krasheninnikov, J. W. Connor, *J. Nucl. Mater.* **1997**, 241–243, 369.
- [22] J. J. Szabo, *Ph.D. Thesis*, Massachusetts Institute of Technology, **2001**.
- [23] A. T. Powis, J. A. Carlsson, I. D. Kaganovich, Y. Raitses, A. Smolyakov, *Phys. Plasmas* **2018**, 25, 072110.
- [24] J. Carlsson, I. Kaganovich, A. Powis, Y. Raitses, I. Romadanov, A. Smolyakov, *Phys. Plasmas* **2018**, 25, 061201.
- [25] H. LI, X. LIU, Z. GAO, Y. DING, L. WEI, D. YU, X. WANG, *Plasma Sci. Technol.* **2018**, 20, 125504.
- [26] J.-P. Boeuf, *J. Appl. Phys.* **2017**, 121, 011101.
- [27] G. Kornfeld, N. Koch, H.-P. Harmann, in *Proc. 30th Int. Electric Propulsion Conf.*, Florence, Septemeber 2007, 17–20.
- [28] S. Weis, A. Lazurenko, A. Genovese, R. Heidemann, P. Holtmann, H. Stalzer, *35th IEPC*, **2017**.
- [29] K. Matyash, R. Schneider, A. Mutzke, O. Kalentev, F. Taccogna, N. Koch, M. Schirra, *IEEE Trans. Plasma Sci.* **2010**, 38, 2274.
- [30] D. Kahnfeld, R. Schneider, F. Cichocki, M. Merino, E. Ahedo, J. Duras, N. Koch, *35th Int. Electr. Propulsion Conf.*, **2017** (IEPC-2017-309).
- [31] Ogawa H. Fahey, T. Muffatti A, *High Fidelity Multi-Objective Design Optimization of a Downscaled Cusped Field Thruster*, Aerospace, **2017**.
- [32] S. H. Yeo, T. Fahey, H. Ogawa, A. Muffatti, P. Matthias, D. Kahnfeld, M. Padivattathumana, R. Schneider, *AIAA* **2019**, 1–9.

How to cite this article: Matthias P, Kahnfeld D, Kemnitz S, Duras J, Koch N, Schneider R. Similarity scaling-application and limits for high-efficiency-multistage-plasma-thruster particle-in-cell modelling. *Contributions to Plasma Physics*. 2020;e201900199.. <https://doi.org/10.1002/ctpp.201900199>

APPENDIX A. SIMULATION RESULTS OF THE TDP1

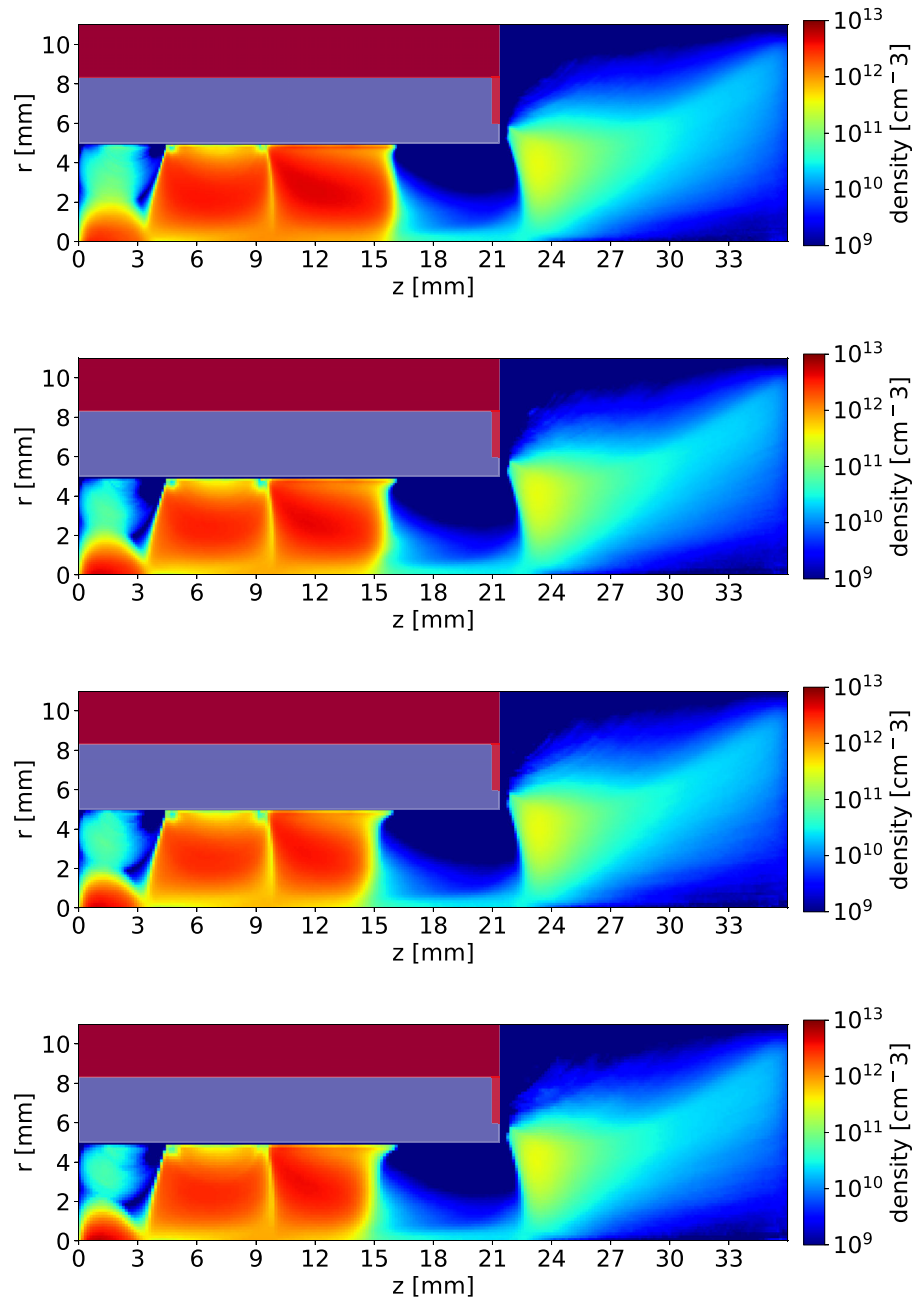


FIGURE A1 Electron density distribution of the TDP1 for the scaling factors $\xi = \{1, 1.2, 1.4, 1.6\}$, from top to bottom

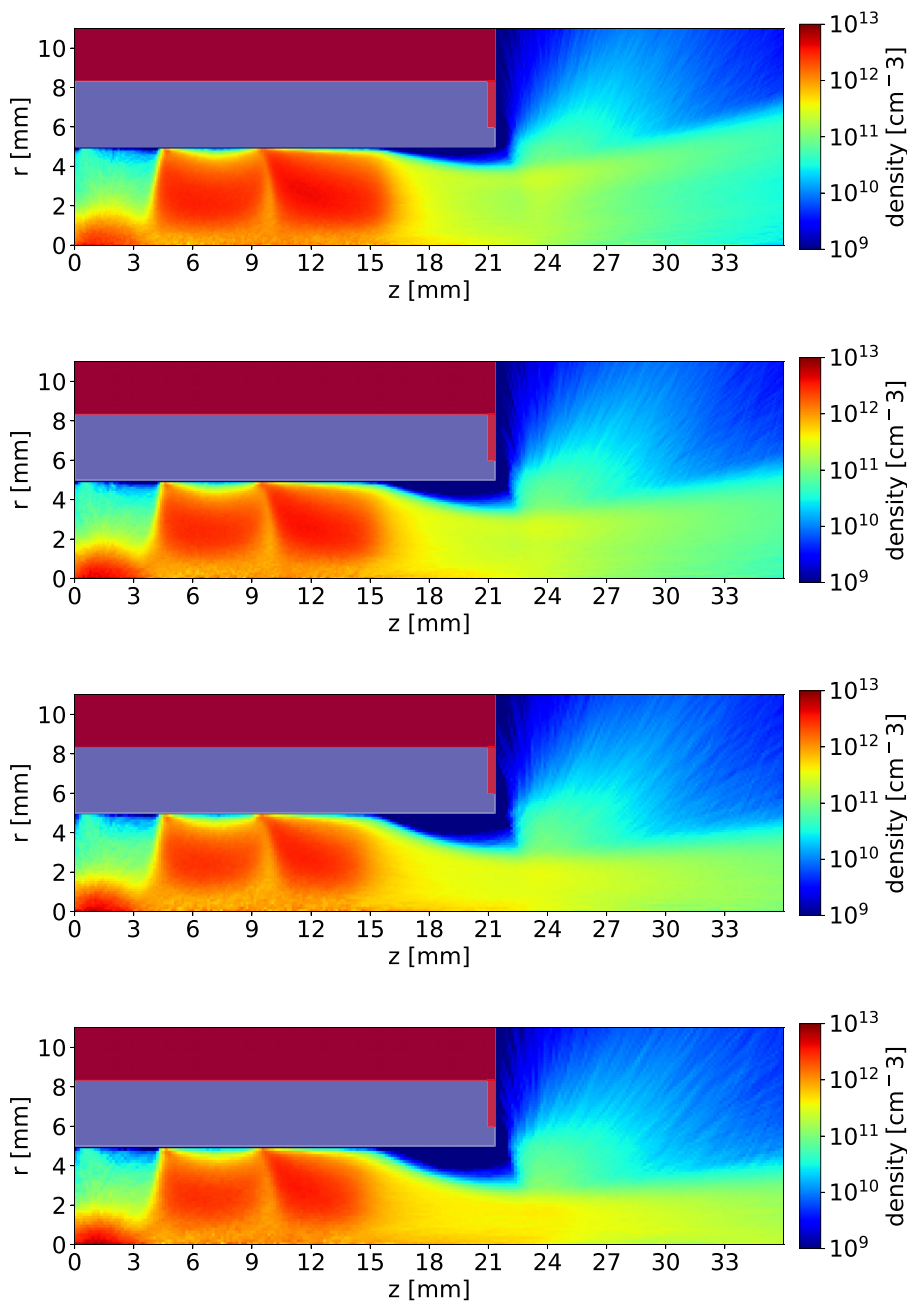
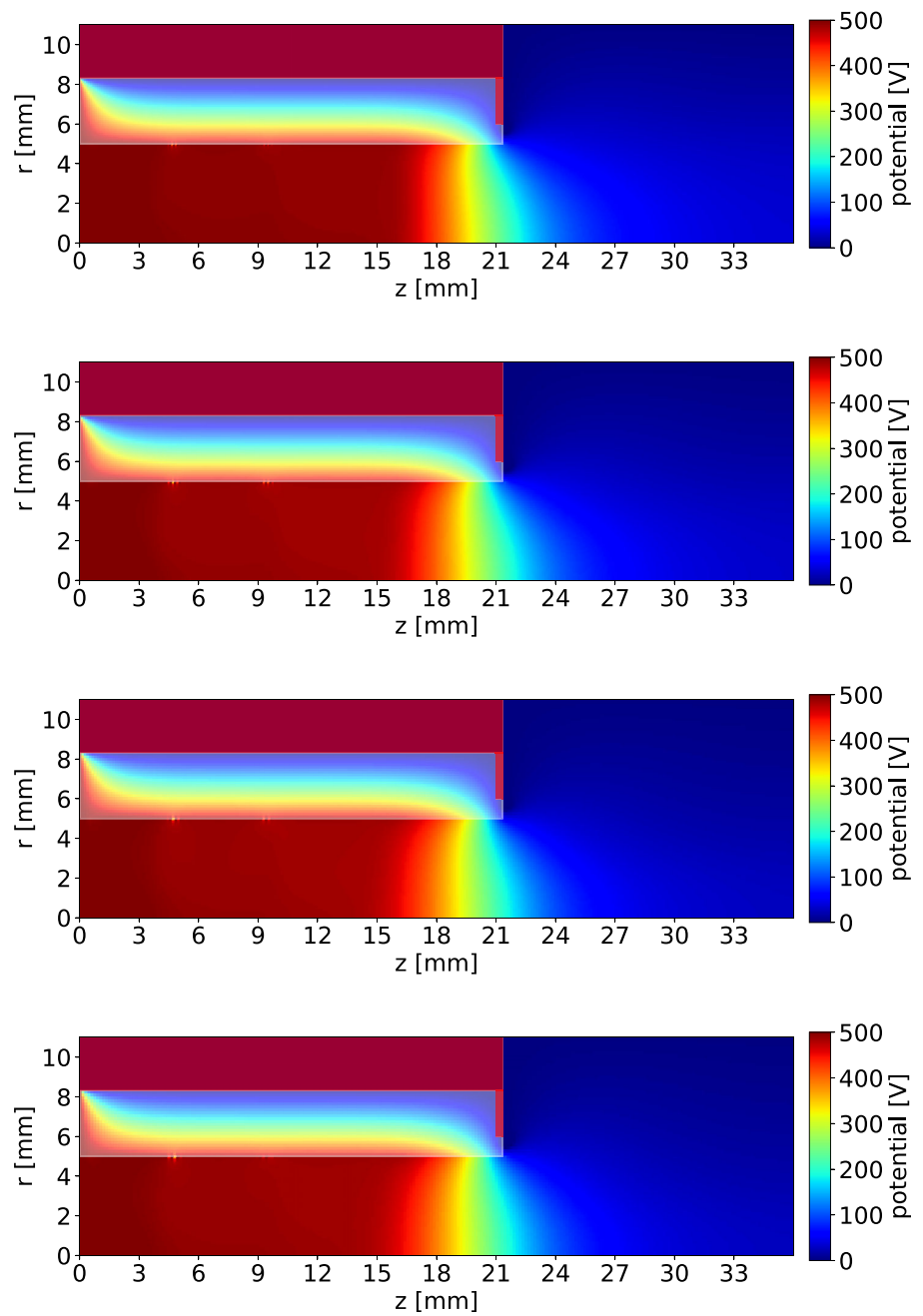


FIGURE A2 Ion density distribution of the TDP1 for the scaling factors $\xi_{\text{ref}} = \{1, 1.2, 1.4, 1.6\}$, from top to bottom

FIGURE A3 Potential solution of the TDPI for the scaling factors $\xi_{\text{ref}} = \{1, 1.2, 1.4, 1.6\}$, from top to bottom



APPENDIX B. SIMULATION RESULTS OF THE DP1

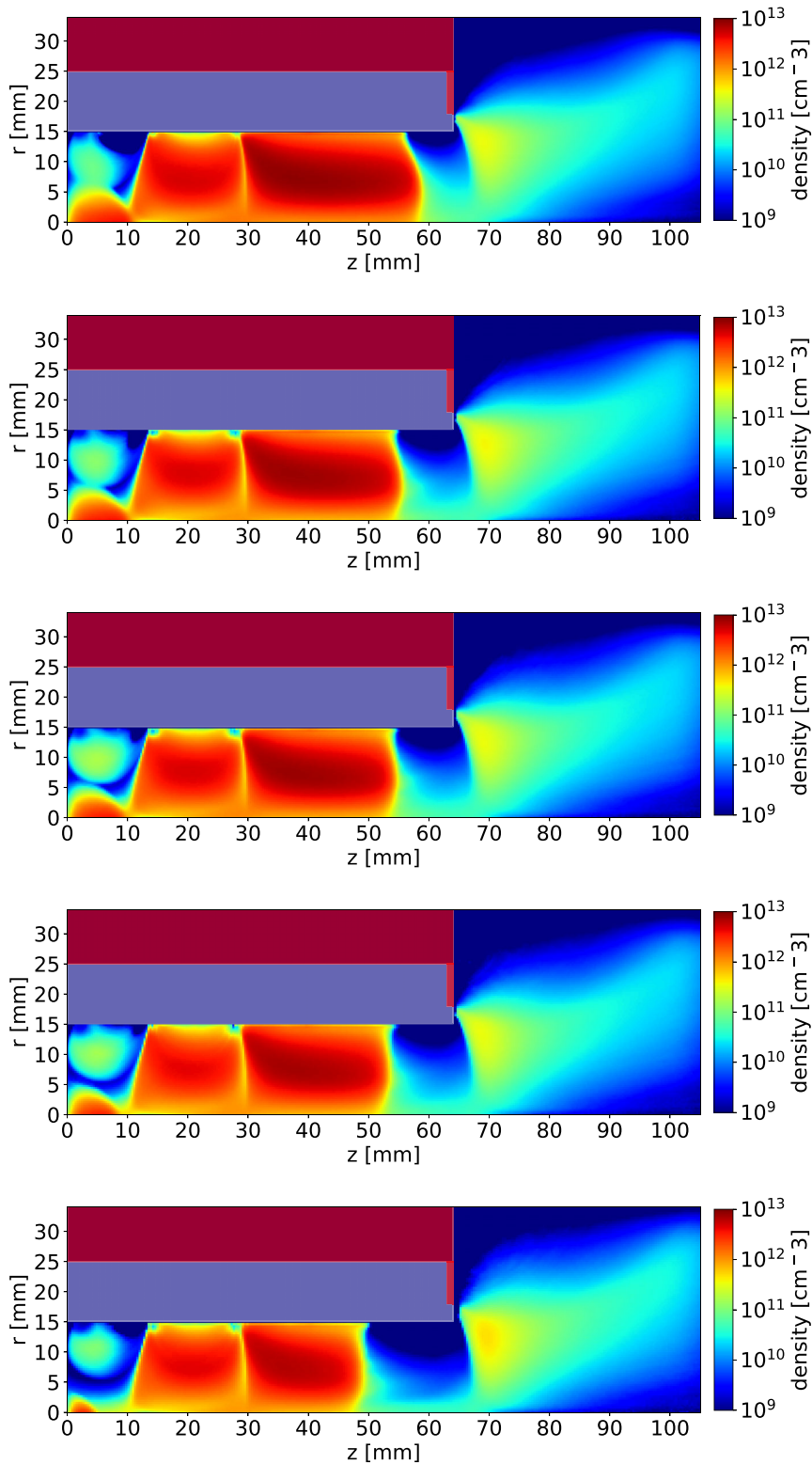
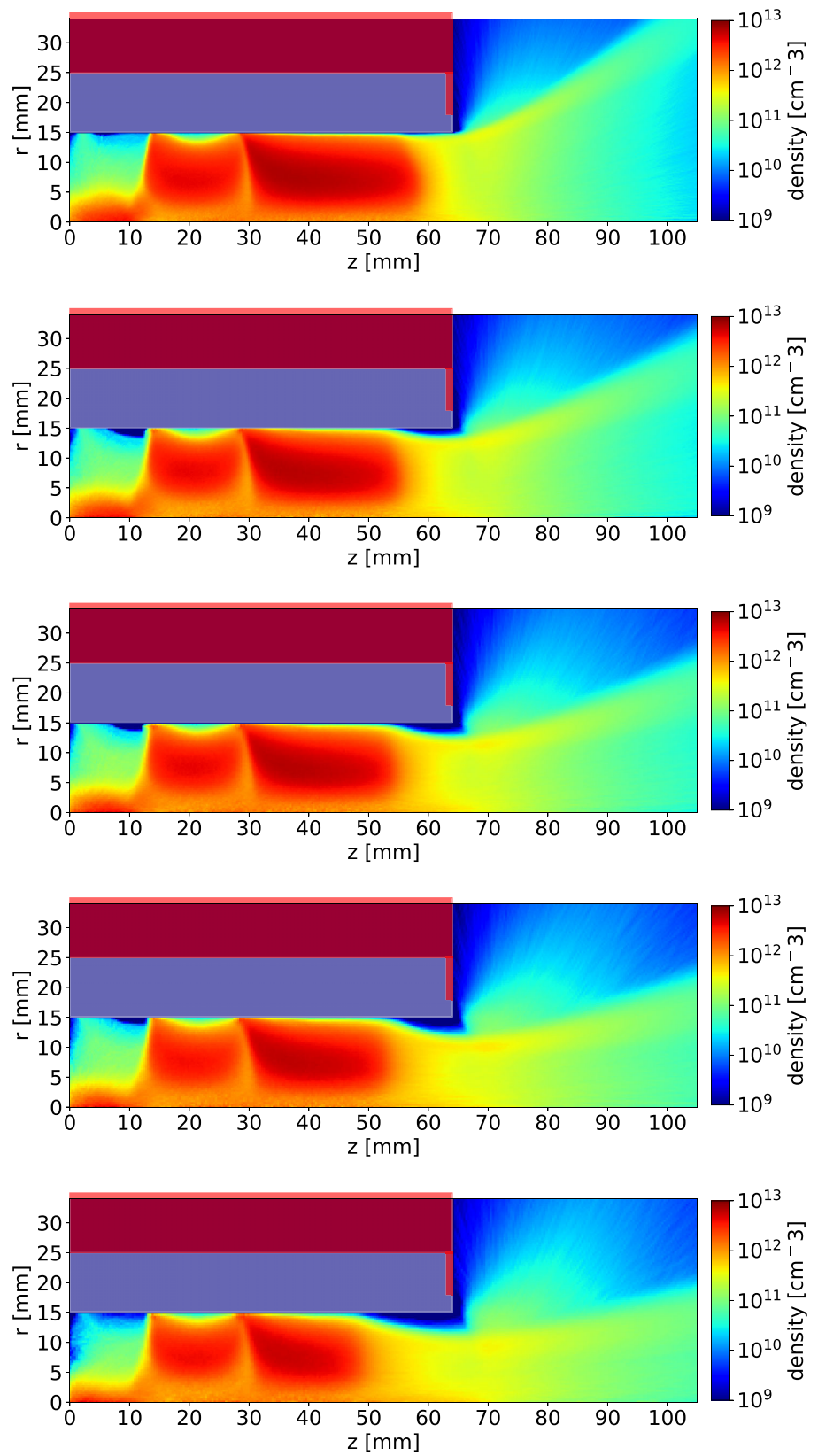


FIGURE B1 Electron density distribution of the DP1 for the scaling factors $\xi_{ref} = \{60, 70, 80, 90, 100\}$, from top to bottom

FIGURE B2 Ion density distribution of the DP1 for the scaling factors $\xi = \{60, 70, 80, 90, 100\}$, from top to bottom



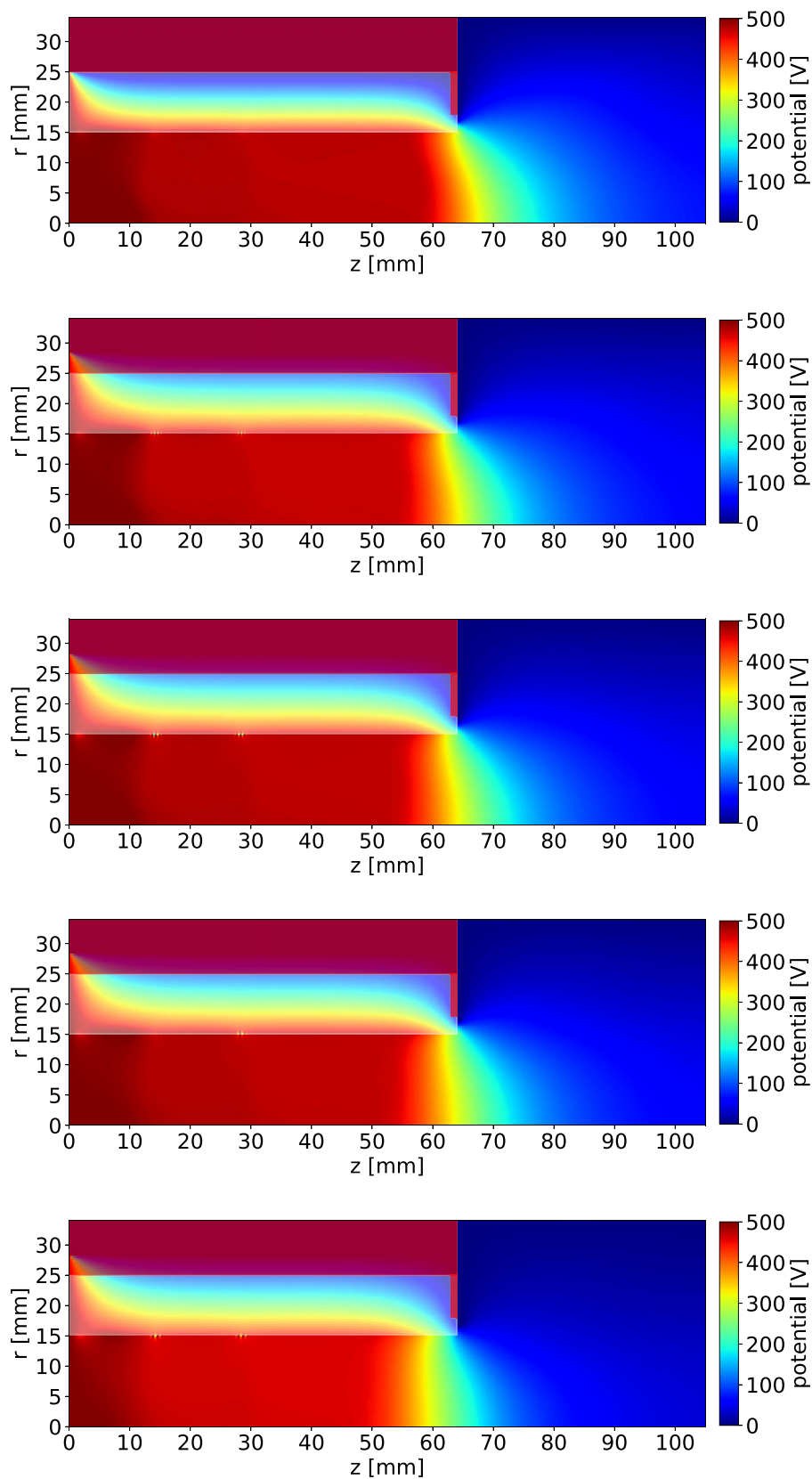


FIGURE B3 Potential solution of the DP1 for the scaling factors $\xi = \{60, 70, 80, 90, 100\}$, from top to bottom

Multi-Objective Optimization and Particle-In-Cell Simulation of Cusped Field Thruster for Micro-Satellites Platform

Suk H. Yeo*, Thomas Fahey†, and Hideaki Ogawa‡
RMIT University, Melbourne, Victoria 3001, Australia

Angus Muffatti§
Aerospace Systems Pty Ltd., Prahran, Victoria 3181, Australia

Paul Matthias¶, Daniel Kahnfeld||, Maya Padivattathumana**, and Ralf Schneider††
Ernst-Moritz-Arndt University Greifswald, Greifswald 17498, Germany

Electric Propulsion (EP) is a suitable propulsion technology for satellite and space missions, offering advantages over chemical propulsion in various aspects including fuel consumption hence launch cost. The cusped field thruster (CFT) offers advantages over other types of EP such as the gridded ion thruster and Hall effect thruster, with enhanced electron confinement owing to the magnetic mirror and reduced particle loss effects at the dielectric wall. The increasing demand for performance improvement of the propulsion system while downscaling for micro-satellite class platforms has led to considerable efforts dedicated to physical modeling and performance characterization of downsized CFT. In the present study a multi-objective design optimization (MDO) study has been conducted to characterize the performance to maximize three performance objectives of downscaled CFT, namely, thrust, total efficiency, and specific impulse defined by common design parameters, namely, anode voltage, anode current, mass flow rate and geometric configuration. Particle-in-cell simulations have been performed for the selected design points identified in MDO studies for verification by accurately accounting for phenomena and performance losses that originate from uncertainties and complexities associated with the thruster design and physics.

Nomenclature

B [T]	: magnetic field	P [W]	: power
B_0 [T]	: magnetic field at low field region	S_i	: first-order sensitivity index
B_m [T]	: magnetic field at high field region	S_{T_i}	: total-effect sensitivity index
q [C]	: elementary charge	T [mN]	: thrust
I_a [A]	: anode current	v [m/s]	: velocity
I_{sp} [s]	: specific impulse	μ	: magnetic moment
K	: kinetic energy	η_b [%]	: beam efficiency
M [kg]	: particle mass	η_t [%]	: total efficiency
m_a [sccm]	: anode mass flow	η_u [%]	: mass utilization efficiency
N	: population size	U_a [V]	: anode potential

*PhD Candidate, Aerospace Engineering and Aviation, School of Engineering, GPO Box 2476, Melbourne, AIAA Student Member

†Aerospace Graduate, Aerospace Engineering and Aviation, School of Engineering, GPO Box 2476, Melbourne

‡Senior Lecturer, Aerospace Engineering and Aviation, School of Engineering, GPO Box 2476, Melbourne, AIAA Member

§Executive Director, 8/27 Izett St, Prahran

¶PhD Student, Institute of Physics, University of Greifswald, Germany

||PhD Student, Institute of Physics, University of Greifswald, Germany

**Scientist, Institute of Physics, University of Greifswald, Germany

††Professor of Computational Science, Director of the Computing Centre, Institute of Physics, University of Greifswald, Germany

I. Introduction

IN-space electric propulsion technologies have been studied and developed over many years for spacecraft propulsion for space missions due to the performance benefits of electric propulsion (EP) such as a longer operational lifetime, better fuel efficiency and less weight [1]. They have mainly been used for station keeping for more than hundreds of satellites in orbit and a few have been proved for primary propulsion in deep-space scientific missions [1].

In general, EP uses electricity to increase the propellant exhaust velocity, aiming to achieve thrust with high exhaust velocities. The gridded ion thruster (GIT) and the Hall effect thruster (HET) are well understood and known as most efficiency propulsion types of EP. These classes of propulsion offer a longer lifetime over 10,000 hours, and higher specific impulse I_{sp} of 1600s - 6000s, but relatively lower thrust values of around 30mN - 230mN, as compared to chemical propulsions [2, 3]. Cusped field thruster (CFT) has been contrived as a possible concept for future missions to avoid undesirable effects while keeping performance at a similar level.

The High-Efficiency Multistage Plasma Thruster (HEMP-T) was firstly developed by Thales Electron Devices (TED) in 1999, and a similar thruster design known as CFT was developed by Harbin Institute of Technology [4, 5]. These technologies are based on the principle of electron ionization from the anode and ion acceleration in electric field similarly to HET schematically shown in Fig. 1 [6].

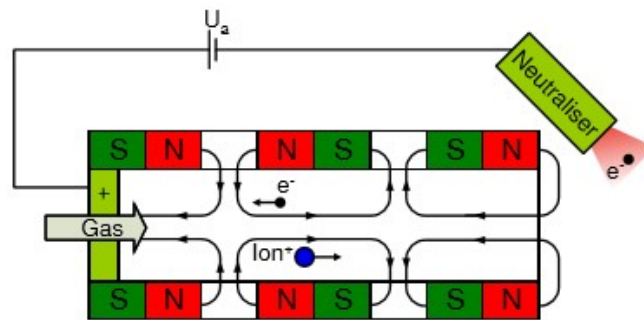


Fig. 1 Principle of HEMP-T (High-Efficiency Multistage Plasma Thruster) [6]

A series of ring-shaped permanent magnets are periodically used to confine the plasma beam through the magnetic mirror effect. These magnets are aligned co-axially along the chamber with reversing polarity to produce the magnetic mirror effect. This significantly reduces wall erosion by restricting the radial motion of the plasma and yields high ion beam efficiencies in the range of 80% - 90% [7]. Cusped regions are formed at between the states of permanent periodic magnets (PPM) where the magnetic field runs radially from the chamber wall, so the electrons oscillate on Larmor radii to increase the interaction length and to reduce wall erosion [7]. This effectively confines the electrons to the center of the engine that in turn helps to electro-statically confine the ions, upon which the magnetic field has little effect because the mean free path of the ion is significantly smaller than its gyro-radius and is not considered magnetized [8]. Ions that escape this confinement contribute to an overall positive charge of the chamber wall and hence enhancement of ion beam formation [9]. The main ionization and acceleration zone separations are characterized by a grid-less GIT as shown schematically in Fig.2 [9]. The thruster also features a steep potential drop occurring after the exit cusp while the plasma potential is constant throughout the engine [7, 9–11]. The electrons emitted from the cathode form the cloud and are confined at the exit cusp that acts as a virtual acceleration grid, like the GIT, resulting in high efficiencies and ions close to the potential of the anode.

Furthermore, there have been some efforts made to scale down EP for specific micro-satellites and deep space exploration, as a miniature concept of CFT would offer better performance over current full-scaled EP thrusters in terms of weight reduction and fuel consumption. This would subsequently result in saving on launch cost for satellites application. However, the previous experimental data of down-scaled EP revealed significantly low performance due to the complexity of the EP system [6]. The main problem arises in the complex interaction of plasma beam with the magnetic field, anode current, anode power, mass flow rate and geometric considerations.

In the present study a multi-objective design optimization (MDO) study based on evolutionary algorithms has been conducted, aiming to simultaneously maximize three objectives, *i.e.*, thrust, total efficiency, and specific impulse of the

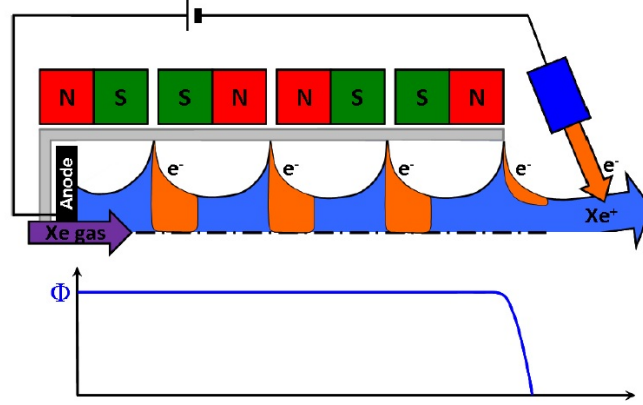


Fig. 2 Ionization region (orange) and potential profile of the thruster [9]

CFT configuration so as to fulfill such design requirements for down-scaled EP. The optimization has been performed by employing the surrogate models that have been trained, based on the results from an initial MDO run using a chain process that incorporates magnetic field analysis coupled with power distribution calculation into evolutionary algorithms. This approach effectively enables robust and efficient population-based optimization at reasonable computational cost by approximating the performance with surrogate modeling in lieu of expensive computational evaluation. Selected CFT designs have been examined to gain insights into key design factors and underlying mechanism. Further investigation has been conducted to verify the performance by means of particle-in-cell simulation that accounts for kinetic effects for accurate analysis of the physics and performance.

II. Methodology

A. Performance characterization

The basic principle of electric propulsion is accelerating mass and ejecting it from the vehicle at higher exhaust velocity than the other propulsion systems. Due to operational similarities of HET and CFT, the basic relation of performance parametric such as thrust T , specific impulse I_{sp} , power P and ideal power to thrust ratio can be defined as follows [1, 12]

$$T = v\dot{m}_p = qE \quad (1)$$

$$I_{sp} = \frac{T}{\dot{m}_p g} \quad (2)$$

$$P_a = \frac{1}{2}\dot{m}_p v^2 = U_a I_a \quad (3)$$

$$PTTR = \frac{P}{T} = \frac{U_a I_a}{I_a \sqrt{2\frac{M}{q}U_a}} = \sqrt{\frac{qU_a}{2M}} \quad (4)$$

where E is the potential difference in an electric field, U_a is the anode voltage, I_a is the anode current, M is the propellant molecular mass (2.18×10^{-25} kg for Xe), and q is the elementary charge (1.602×10^{-19} C).

The total efficiency η_t of electric propulsion is defined as the ratio of the electrical power to the input power from the anode P_a .

$$\eta_t = \frac{T^2}{2\dot{m}_p P_{in}} \quad (5)$$

where P_{in} is the total power input.

Similarly, anode efficiency is generally utilized, defined as:

$$\eta_a = \frac{T^2}{2\dot{m}_a P_d} \quad (6)$$

where P_d is the discharge power, \dot{m}_a is the anode mass flow rate, and \dot{m}_p is the mass flow rate of propellant (anode and cathode) [1].

The anode efficiency η_a can be derived and accurately calculated using voltage efficiency, beam efficiency, utilization efficiency, and the coefficient of plume divergence. The beam efficiency η_b is the ratio of power at the anode to the power at plasma beam, and the utilization efficiency η_u is the maximum current obtainable from the supplied beam current assuming only singly charged ions. Due to the divergence of the ion beam with the effective divergent angle θ_{eff} , the coefficient of plume divergence is required to solve proper relation of propulsions [1].

$$\eta_v = \frac{U_b}{U_a} \quad (7)$$

$$\eta_b = \frac{P_b}{P_a} = \frac{I_b}{I_a} \quad (8)$$

$$\eta_u = \frac{I_b}{\dot{m}_p q / M} \quad (9)$$

$$\eta_a = \frac{1}{Q^2} \eta_v \eta_b \eta_u \cos^2 \theta_{eff} \quad (10)$$

From Goebel and Kats [1], the beam current can be determined by the mass flow rate.

$$I_b = \frac{q\dot{m}_a}{M} \quad (11)$$

where the subscript b indicates the ion beam, Q is the average ionic charge, I_b is the total ion current in the beam, U_b is the total ion voltage in the beam, $\cos^2 \theta_{eff}$ accounts for plume divergence where ions are not accelerated parallel to the engine axis. The propellant is assumed to be Xenon, which is typical for CFT. Eq. (10) is a basic equation that assumes 100% ionization and singly ionized for HET, while it would not fully describe low ionization at low voltages and multiply charged ions at high voltages, which could occur in practical applications.

A key feature of the CFT concept is high voltage operational range, typically between 500V and 2000V. Lower efficiencies under the same mass flow rates condition were found with the anode voltage below 500V [4, 5], thus the effects of low ionization were not captured by this study. The ion current can be approximated by the anode current with an error of less than 20% with 100% singly charged ions [4].

$$\eta_m = \frac{\dot{m}_a}{\dot{m}_p} = \frac{I_b}{q} \frac{M}{\dot{m}_p} \quad (12)$$

The mass utilization efficiency, described in part of Eq. (12) is sensitive to the beam current and mass flow. As a result, this study assumes that the ion beam current can be sufficiently approximated by Eq. (11). The mass utilization efficiency correction factor to consider the effect of multiply charged ions is given by α_m in Eq. (13) [1].

$$\eta_m = \alpha_m \frac{I_b}{q} \frac{M}{\dot{m}_p} \quad (13)$$

$$\alpha_m = \frac{1 + \frac{1}{2} \frac{I^{++}}{I^+}}{1 + \frac{I^{++}}{I^+}} \quad (14)$$

Applying this methodology without the correction factor to the Variable Magnet Length Cusped Field Thruster (VML-CFT) resulted in mass utilization efficiency of 89% [5]. This correlated well with the results of the experimental study on DCFT, where the mass utilization efficiency was measured to be 87% [13]. In the present study the MDO does not consider the effects of multiple ion species on the correction factor. However, the effect of 20% doubly charged ions in the mass utilization efficiency ($\alpha_m=0.9$) [4] and other assumptions made regarding the acceleration, divergence and utilization efficiencies are taken into account in the post-processing phase. This is because while these factors have uniform effects on the objective parameters, they are difficult to be determined accurately with the present methodology.

A simplified power balance description of HEMP-T based on plasma fluid theory yields a one-dimensional set of equations (28 in total), which can be solved simultaneously to allow for reasonable estimate of the thruster performance [7]. As the only known values in the equation set are the probabilities to reach the channel wall at the cusp locations and these probabilities are based on the magnetic field strength, the thruster performance can be estimated through only a few parameters. These are anode potential, anode current and the ratio of magnetic field strength from the axially aligned region where the fields radially cross the discharge channel walls, *i.e.*, the magnetic mirror strength. It is also important to note that the ratios of power transferred to excitation, ionization, and thermalization are only estimations as per Ref. [7], where a full description of the power model can be found.

CFT operation is mainly characterized by the PPMs that are used to create magnetic mirror effect to reduce electrons losses due to impingement on the walls, as prescribed by the Lorentz force equation below in Eq. (15). It follows that the magnetic field does not have impact on the particle directly, but it exerts longitudinal axial force F_z when its strength increases in the opposite direction of its motion with constant kinetic energy K [1, 11, 14, 15].

$$F_z = \frac{mv_{\perp}^2}{2B} \nabla_{\parallel} B \quad (15)$$

where v_{\perp} is the cyclotron motion of the particle in terms of a magnetic moment.

$$F_{\parallel} = -\mu \nabla_{\parallel} B \quad (16)$$

The magnetic moment is constant by equating and balancing the magnetic moment at the high and low field regions when the particle is moving through a magnetic field of increasing strength:

$$\frac{v_{\perp 0}^2}{B_0} = \frac{v_{\perp m}^2}{B_m} \quad (17)$$

where subscripts 0 and m refer to low and high field regions, respectively.

The equation of velocity of the particle can be solved by conservation of the particle kinetic energy:

$$K = \frac{1}{2}m(v_{\parallel}^2 + v_{\perp}^2) \quad (18)$$

Therefore

$$v_{\parallel} = \left[\frac{2}{m}(K - \mu B) \right]^{\frac{1}{2}} \quad (19)$$

To ensure magnet mirror effect, the vector of velocity is required to be within acceptable angle, and the equation can be solved using the conservation of kinetic energy and derived as follows [14]:

$$\frac{B_m}{B_0} = \frac{v_{\parallel 0}^2 + v_{\perp 0}^2}{v_{\perp 0}^2} = \frac{1}{\sin^2 \theta_m} \quad (20)$$

Therefore

$$\theta_m \leq \sin^{-1} \left(\frac{B_0}{B_m} \right) \quad (21)$$

Arrival probabilities of the electrons at the cusp region can be determined as [7]

$$P_c = \frac{2\pi \int_0^{\alpha_c} \sin \theta d\theta}{4\pi} \quad (22)$$

The cusp arrival probabilities are directly related to the accuracy of the simulated magnetic topologies of the thruster, which is calculated using two-dimensional electromagnetic field analysis.

VML-CFT from the available literature is used to validate this approach as it considered the physical dimensions and material properties for the thruster and the subsequent analysis of the results provides a robust range of observation points that can be modeled and compared [5] (readers are referred to Ref. [16] for validation).

B. Multi-Objective Design Optimization

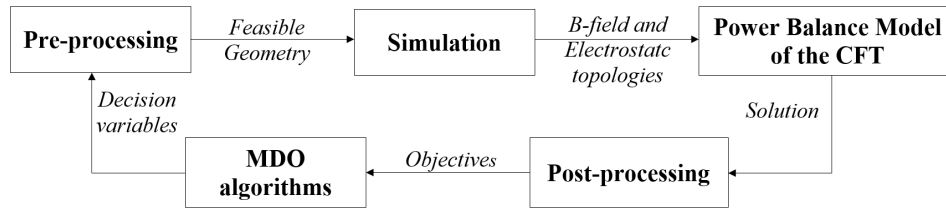


Fig. 3 MDO process chain

MDO is performed in a chain process consisting of sequential phases, as shown in Fig. 3 [16]; (1) The decision variables are examined in the pre-processing phase to assure the geometry is physically viable prior to simulation; (2) ANSYS Maxwell [17] constructs a model for the given geometry and calculates the magnetic field by means of magnetostatic analysis, and then electrostatic analysis is performed to calculate the potential at the thruster exit and in the plume. The data is then extracted from the magnetic topology to compute the cusp arrival probability for each location throughout the thruster; (3) These conditions are subsequently passed on to be used in the power balance calculation; (4) The resultant solutions from this are post-processed to deliver the objectives and assess if they lie within the set of physical constraints; (5) They are then submitted to the MDO algorithms for evaluation. This iterative cycle continues, yielding more designs to be evaluated according to the set criteria.

The design optimization is performed by employing evolutionary algorithms. In particular, use is made of the elitist non-dominated sorting genetic algorithm (NSGA-II) assisted by surrogate modeling [18]. It is a population-based approach where the candidate solutions in the population pool evolve over generations. A population size of $N = 64$ is used in this study to be evolved over 50 generations for the initial MDO stud and that of $N = 100$ over 100 generations in the MDO run performed solely based on prediction from surrogate models. These values have been chosen to sufficiently explore the design space for a 3-objective design problem with 5 decision variables within reasonable computational effort. Recombination operators are applied to the previous generation's decision variable values to create offspring. A simulated binary crossover and polynomial mutation are used as recombination operators at a given probability (1.0 and 0.1, respectively, in this study) with a specified distribution index (10 and 20, respectively)[19]. The use of a strongly elitist non-dominated sorting genetic algorithm always retains the best solutions across generations. This means that there is no incentive for parents to survive but to use the crossover mutation to broaden the search for better solutions; hence the crossover probability is given by 1.0. The advantage of the MDO approach undertaken in the present study is the ability to maintain multiple objectives and perform optimization to aim at all the objectives simultaneously, which is the primary virtue of MDO. This removes the no need for weighting on the objectives to convert a multiple-objective optimization problem to a single objective one, as required for a single-objective optimization framework.

Surrogate modeling is commissioned to estimate the possible values of the objectives and constraints in an inexpensive manner, imitating the behavior of the solutions from the magnetic and power analyses with meta-models characterized by appropriate mathematical functions based on the magnetostatic, electrostatic and power balance simulations. The surrogate models are constructed by using a fraction (90% in this study) of the actual solutions calculated from the magnetic and power distribution models to prevent over fitting, whereas the remainder (10%) of the evaluated solutions are used to assess the performance of the surrogate models [19]. Surrogates for each of the objective and constraint functions are trained by using a subset of the archive, which is created by selecting the solutions closest to the centroids of the k clusters obtained through k -means clustering [20]. Multiple surrogate models are employed and evaluated; quadratic response surface model; artificial neural network (ANN) models including the radial basis function network and multilayer perceptron model, which are single-layer and feed forward types of ANN models, respectively; and Kriging model based on Gaussian process regression [21–24]. The mean squared error (MSE) in the actual and predicted values of the objectives and constraints is calculated for the remaining (10%) solutions and used as the measure to validate the surrogate models. Prediction from the best surrogate model with a minimum error is adopted to replace simulation analysis, only if the MSE is within a threshold value of 5% for all objective and constraint functions and the distance to the closest point in the archive is smaller than 5% [19].

Three objective functions are considered and employed to evaluate design performance, namely thrust T , total

efficiency η_t^* , and specific impulse I_{sp} . Total efficiency η_t is comprised of the measures of efficiencies within the thruster model, that is, the beam efficiency η_b , the mass utilization efficiency η_m , and the voltage efficiency η_v . The decision variables chosen to represent the main design factors investigated in this study are U_a (V), I_a (A), \dot{m}_a (sccm), inner magnetic radius IMR (mm), outer magnetic radius OMR (mm). The negative sign for the objective functions denotes a maximization problem (converted from a minimization problem). The decision variables U_a (V), I_a (A) and \dot{m}_a (sccm) relate to the objective functions through Eqs. (1) - (10) and the initial conditions of the CFT at the anode. The magnetic radii IMR and OMR are related to the objective functions through the one-dimensional simplified power balance model. The radii affect the strength of the magnetic field in the high and low regions which is used to solve the power balance model, describing the plasma potentials, cusp potentials, ionization source currents, and electron and ion currents across plasma cells that divide the discharge chamber length in the simplified model. In consequence the beam and grid efficiencies are determined, and power losses due to ionization and excitations are calculated at the anode and cusps, which impact the objective functions. The optimization statement is thus summarized in Table 1, along with the rangers of the decision variables.

Table 1 Optimization problem

Maximize:	T, η_t, I_{sp}
Subject to:	$0 \leq U_a \text{ (V)} \leq 1000$ $0 \leq I_a \text{ (A)} \leq 10$ $0.2 \leq \dot{m}_a \text{ (sccm)} \leq 50$ $2 \leq IMR \text{ (mm)} \leq 50$ $2 \leq OMR \text{ (mm)} \leq 50$

Variance-based global sensitivity analysis is performed to examine the influence of each decision variable, x_i as input (*i.e.*, design parameters) on the objective function y as output (*i.e.*, performance parameters). A numerical procedure is employed to derive the sensitivity indices, facilitated by surrogate modeling [25]. Input matrices \mathbf{X} of a base sample quantity of 10,000 and multiple columns for the decision variables are built by using quasi-random numbers within the range for each variable [26]. Output vectors \mathbf{Y} are obtained by forwarding the input matrices to the surrogate model that is of the greatest prediction accuracy. The first-order indices S_i and total-effect indices S_{T_i} in Eqs. (23) and (24) are calculated by the method described in Ref. [27].

$$S_i = V[E(Y|X_i)]/V(Y) \quad (23)$$

$$S_{T_i} = 1 - V[E(Y|X_{-i})]/V(Y) \quad (24)$$

A simplified two-dimensional CFT model is used for the calculations using ANSYS Maxwell to mitigate the computational load, which would otherwise be expensive due to the nature of the MDO process and to facilitate the identification of the relationships between the output objectives and the decision variables. This model assuming axis symmetry at the engine axis consists of a consistently straight chamber made of BN Ceramic, Samarium-Cobalt (SmCo) 27 megagauss-oersteds (MGOe) magnets with spacers made of pure iron (due to high conductivity and to improve commonality with other CFT design) and the thruster housing made of Al 6061-T6 [4, 9, 28, 29]. Geometric constraints are applied to restrict the scope and output of the design space, including geometries (inner magnetic radius IMR and outer magnetic radius OMR). Designs with a geometry that overlaps are deemed infeasible solutions in MDO. The upper limit is assumed within the limits of the standard CubeSat design (1U) [30].

C. Particle-In-Cell Simulation

Since the electron mean-free paths in the considered HEMP-Ts are comparable to the system size and kinetic effects in the magnetic cusps (similar to magnetic mirrors) create non-Maxwellian perturbations of the electron distribution functions, a kinetic simulation of the system is necessary for accurate analysis [31]. Due to the axisymmetric problem, a two-dimensional PIC code with cylindrical (r - z) coordinates and three dimensions in the velocity space is used, in conjunction with a Monte-Carlo-collision (MCC) model[32].

*Efficiency term with the subscript t is a somewhat misnomer, usually descriptive of total efficiency, and it must be stated that the model presented in this paper does not take into consideration plume divergence losses or an accurate representation of acceleration efficiencies.

The number of particles in the real plasma is so large that it exceeds the capacity that can be handled even by supercomputers. Therefore the present PIC simulations consider a single particle (so-called *superparticle*) consisting of many plasma particles. Since the charge/mass ratio of the superparticle is the same as the actual particle, the particle trajectories are also the same as those of individual plasma particles. Consequently, the plasma model simulated using superparticles is the same as that of the real plasma with appropriate re-scaling of parameters. The dynamics of neutral propellant atoms (Xe), electrons (e^-), as well as Xe^+ and Xe^{2+} ions, are treated as superparticles. In measurements of other HEMP-Ts the density of multiply charged Xenon ions is of magnitudes lower than doubly charged ions [33]. Based on these observations, multiply charged Xenon ions are neglected for this work, too.

In order to simulate the real plasma, the force on the particles has to be calculated self-consistently. The potential and the electric field are calculated on a spatial grid based on the charge of the superparticles mapped on the grid points done by charge weighting. The calculated fields and forces are mapped from the grid points to the particle positions, called field weighting, using the same weighting function as before to preserve energy and impulse. The superparticles are moved according to the Lorentz force using the Boris algorithm [34]. The new particle positions and velocities are calculated considering the thruster boundary conditions.

The MCC model covers several different collisions. In the present study electron-electron Coulomb collisions are simulated directly [35] and all other collisions are modeled with experimentally measured collision cross-sections [36]. These collisions are direct single and double e^- -Xe impact ionization, single e^- - Xe^+ impact ionization, integral elastic Xe^+ -Xe collisions (including charge exchange and momentum transfer), and integral elastic and inelastic e^- -Xe collisions [32]. An electrostatic model is used since the magnetic field contribution from the plasma currents can be neglected.

In the simulation model, the entire thruster discharge channel and a part of the near-field plume are considered.

For computational feasibility, similarity scaling is used to simulate the system. It is designed to leave the physical behavior within the thruster channel (where electrons are magnetized) unchanged, thus the Hall parameter and the Knudsen number of the system are preserved. The similarity scaling scales down the system size and time linearly, while the velocities and densities remain unscaled. A closer description of the similarity scaling scheme can be found in Ref. [32].

III. Results

A. Multi-Objective Design Optimization

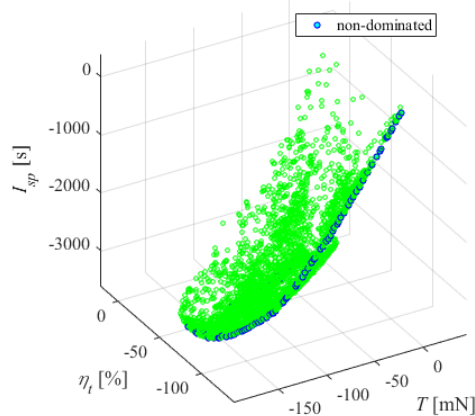


Fig. 4 Optimization results from MDO

Figure 4 presents the results obtained from the MDO after evolution over 100 generations performed by using the surrogate models that have been built based on the initial MDO performed by employing ANSYS Maxwell for magnetostatic analysis. The green points indicate the feasible geometries, and the blue points represent non-dominated

solutions. The Pareto optimal front is indicative of the counteracting nature of the objective functions. Presented in Fig. 5 is parallel coordinate plots that visualize the trends and relations among the decision variables and objective and constraint functions for the non-dominated solutions identified by the MDO.

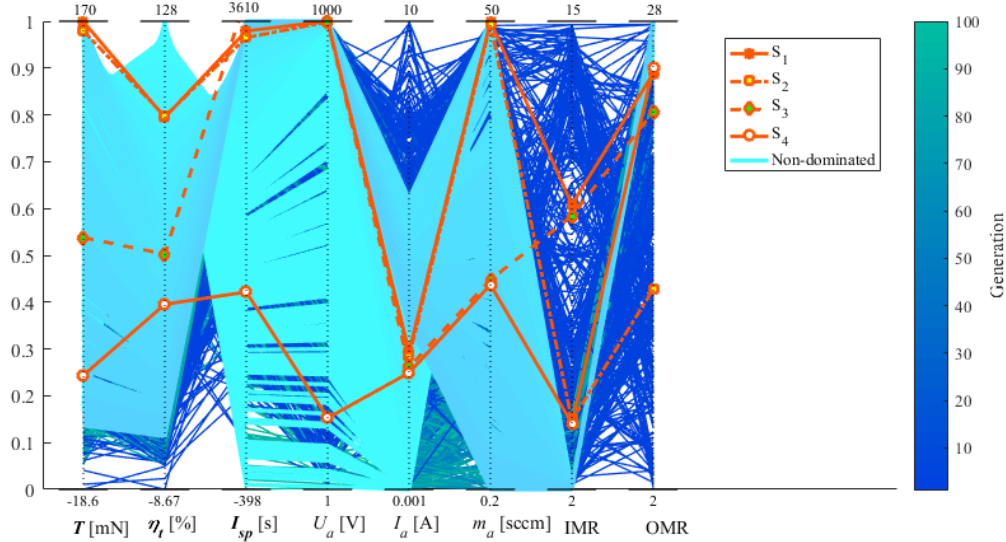


Fig. 5 Parallel coordinate plot

Table 2 shows the representative solutions, primarily non-dominated hence optimal design points that have been selected from the Pareto optimal front (Fig. 4) with respect to each objective function, as indicated by bold values. The first selected solution S_1 features the largest thrust T among all designs. It is characterized by the mass flow and anode potential at their upper limits. The second selected point S_2 has attained the highest measured total efficiency η_t of the evaluated feasible designs, while it produces the lowest specific impulse, as compared to its non-dominated peers, *i.e.*, S_1 and S_3 (albeit similar in values). S_2 is characterized by a distinctly different design configuration, with the inner magnet radius (IMR) much closer to the engine axis. This signifies the role of the inner magnet radius in achieving high thrust densities. The third selected solution S_3 has the highest specific impulse I_{sp} of all evaluated designs with the lowest mass flow rate. It achieves appreciably high I_{sp} as a trade-off with thrust and efficiency. In comparison to its non-dominated peers, it incurs approximately 80 mN reduction in thrust. Further, reduction of about 40% in efficiency is observed for S_3 . In comparison to S_1 and S_2 , S_3 has comparable thrust, efficiency, anode potential, while the mass flow rate in S_1 is much lower than its peers.

Table 2 Selected design configurations

Solution	T [mN]	η_t [%]	I_{sp} [s]	U_a [V]	I_a [A]	\dot{m}_a [sccm]	IMR [mm]	OMR [mm]
S_1	169.9	99.6	3526	999.9	2.94	49.98	9.91	25.10
S_2	166.2	99.9	3469	998.4	2.83	49.69	3.91	13.13
S_3	82.9	59.8	3825	997.8	2.61	22.51	9.59	22.97

Tables 3 and 4 display the first-order indices S_i and the total-effect indices S_{T_i} identified by the covariance-based sensitivity analysis performed for both magnetic configurations. They quantitatively indicate the main and overall effects of the input parameters (*i.e.*, decision variables) namely U_a , I_a , \dot{m}_a , IMR , and OMR on the output parameters (*i.e.*, objective functions) namely thrust T , total efficiency η_t , and specific impulse I_{sp} . The difference between the total-effect index S_{T_i} and the first-order index S_i is indicative of the degree of the influence of the decision variable in combination with other decision variables (*i.e.*, interactions) on the objective functions [26]. If the decision variables are characterized by the sum of both first-order and total-effect indices being near unity (*i.e.*, $\sum S_i \approx 1$ and $\sum S_{T_i} \approx 1$),

it follows that the effects of individual decision variables are linearly additive. The sensitivity indices indicate that the influence on the design is primarily caused by four design parameters, *i.e.*, I_a , OMR , IMR , and \dot{m}_a . I_a exerts the most influence on specific impulse I_{sp} , while OMR predominantly influences the total efficiency. It is evident that the decision variables exhibit similar influence across the three objectives, as expected by Eq. (5). The considerably large difference between the summations of S_i and S_{T_i} is indicative of highly nonlinear behavior between the design variables and output parameters.

The large influence of mass flow rate \dot{m}_a and anode current I_a is inherently expected due to the highly interrelated nature of the calculation of total efficiency η_t that involves and relies on these parameters. The beam efficiency η_b represents a primary source of the efficiency loss and is thus directly sensitive to anode current as per Eq. (9) [15]. Further, the beam current is strongly related to the mass flow rate due to Eq. (11) [1, 37, 38], and assessment of the influence of these decision variables (design parameters) on the objective functions (performance parameters) offers flexibility in identifying the designs to achieve optimal performance. The sizable influence of the outer and inner magnet radius OMR and IMR is assumed to be attributed to their influence on the magnetic field strength due to geometric variation, while further investigation would be necessary to verify this. It is important to note that other measures for the efficiency such as the mass utilization, acceleration efficiency and divergence losses are not taken into consideration in the present model, as mentioned in Section II.A, and would need to be estimated or deduced from existing experimental studies.

Table 3 First-order sensitivity indices

Output Parameter	U_a	I_a	\dot{m}_a	IMR	OMR	Sum
T	0.015	0.084	0.050	0.018	0.072	0.239
η_t	0.007	0.051	0.026	0.042	0.153	0.279
I_{sp}	0.009	0.097	0.034	0.036	0.167	0.343

Table 4 Total-effect sensitivity indices

Parameter	U_a	I_a	\dot{m}_a	IMR	OMR	Sum
T	0.111	0.597	0.430	0.433	0.565	2.136
η_t	0.165	0.549	0.328	0.363	0.702	2.107
I_{sp}	0.089	0.644	0.308	0.409	0.600	2.050

For the mass utilization efficiency, the study assumes to allow for the presence of 20% doubly charged ions, resulting in a correction factor of $\alpha_m = 0.9$, based on Eq. (14) [4]. The plume divergence efficiency is based on an assumed divergence angle of 60° [4]. The acceleration efficiency requires significant measurement of the CFT, which is beyond the scope of this study. Keller et al. presents a combined acceleration and divergence efficiency of 40.7% (*i.e.*, $\eta = \eta_{acc} \cdot \eta_{div} = 0.407$) by extrapolating the acceleration efficiency from the Faraday measurement values [4]. This produces a more conservative estimation of the objective parameters. The adjusted performance taking into account these efficiencies and multiply charged ions is shown in Table 5 for the selected designs.

Table 5 Adjusted performance of selected designs

Solution	T [mN]	η_t [%]	I_{sp} [s]
S ₁	102.7	36.5	2131
S ₂	100.5	36.6	2098
S ₃	50.2	21.9	2313

B. Particle-in-Cell simulation

PIC simulations are performed to scrutinize the characteristics and performance of the proposed thruster design obtained by the MDO study. In this work the S_1 (Table 5) has been selected as a representative configuration for the most promising thruster design. The magnetic field has been obtained by magnetostatic analysis using ANSYS Maxwell and applied to the computational domain.

A time step of $\Delta t = 8.9 \times 10^{-14}$ s and a cell unit length of $\Delta r = 1.8 \times 10^{-3}$ mm are used. The dimensions of the simulation plane are $20.0 \text{ mm} \times 50.0 \text{ mm}$, with a similarity scaling factor of 40, resulting in 283 cells in radial and 709 cells in axial direction for the simulation domain. The propellant gas influx is placed at the anode with a Xenon flow rate of 50 sccm. A voltage of 1000 V is applied at the anode. The total simulation time is in the range of $10 \mu\text{s}$ to $100 \mu\text{s}$ so as to cover all relevant transport times of electrons, ions and neutrals. All of the results of the simulation are presented in the real system, not in the self similar scaled system.

At the left boundary of the simulation domain, a constant potential boundary condition at anode voltage U_a is applied, the top boundary is at ground potential while the electric field is fixed to zero at the right boundary. A dielectric is used for the channel wall, including secondary electron emission and ion/neutral recycling.

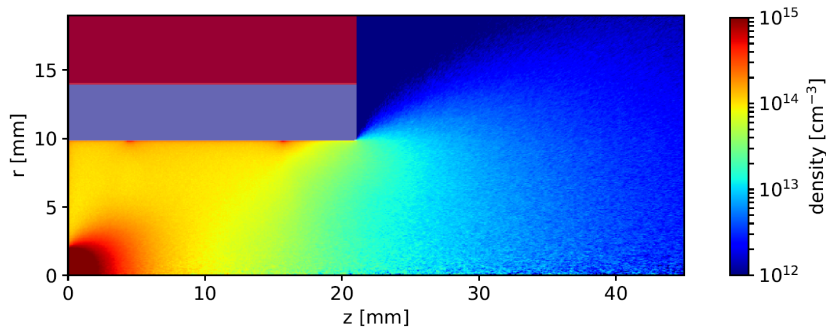


Fig. 6 Neutral density field

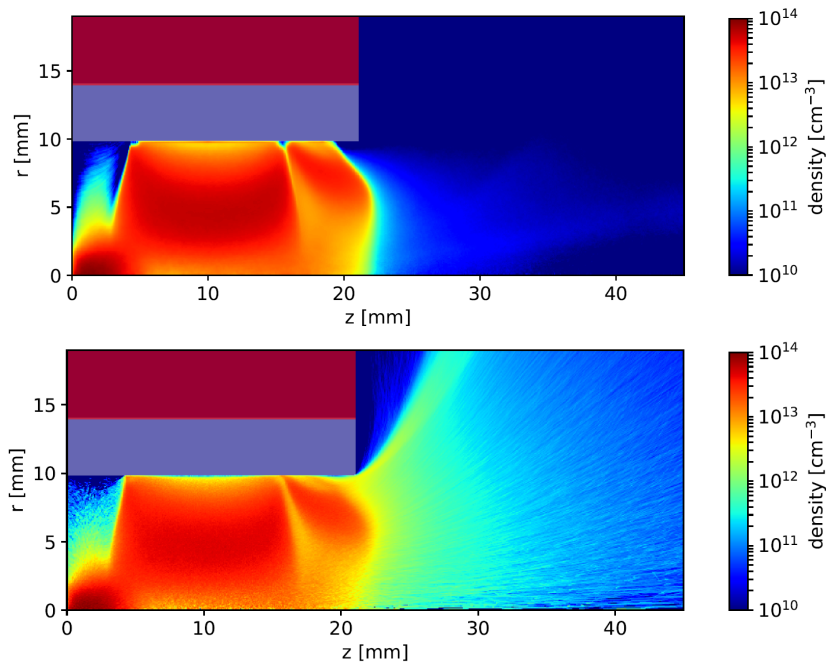


Fig. 7 Electron (top) and Xe^+ ion (bottom) density distributions

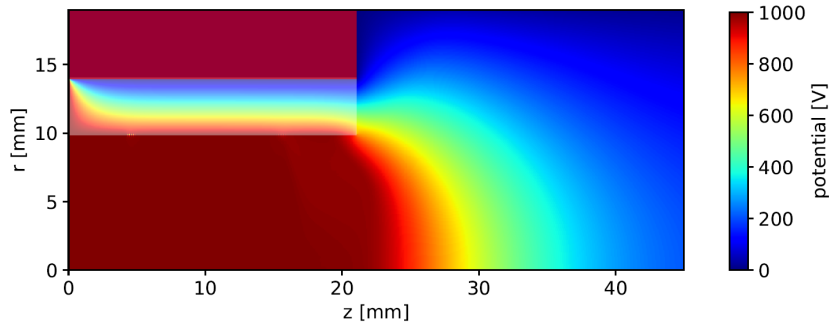


Fig. 8 Potential field

At the start of the simulation the channel is filled with neutrals at the desired neutral flow rate and then ignited to create a plasma. After ignition an external electron source is applied in the plume, working like an artificial cathode to neutralize the plume and to feed the thruster discharge. The neutral density profile within the system for a mass flow rate \dot{m}_f of 50 sccm, a cathode source current of 800 mA and an anode potential of 1000 V is shown in Fig. 6.

The cathode source is located at the right domain boundary at $z = 45$ mm. The base injection current is not determined by the MDO but variable, and can be adjusted to fit the anode current proposed for different thruster designs.

The cathode electrons are propelled towards the thruster channel, where they start to ionize the neutral gas and build up the plasma. The resulting electron and ion density distribution can be seen in Fig. 7. Inside the channel the electrons follow the magnetic field lines and get reflected in the cusp regions leading to a long lifetime of the electrons and therefore for a higher collision probability. This results in high plasma densities $\approx 10^{14}$ cm $^{-3}$ in the channel.

The potential field is displayed in Fig. 8, which shows the flat potential inside the channel and the steep potential drop at the thruster exit and further drop to vacuum potential out in the plume. The produced ions drift through the channel, until they are accelerated by the potential drop at the thruster exit. At the domain boundary the accelerated ions are tracked for further diagnostics such as thrust calculation and angular current distributions.

IV. Discussion

The PIC simulation of the S_1 configuration has shown a typical behavior of CFT thrusters as discussed in the preceding section. With the full kinetic description from the PIC results it is now possible to calculate performance parameters considered in the MDO in a self consistent manner. Table 6 compares the values for performance parameters as well as the anode and beam currents between the modeling used in MDO and the calculations from the PIC simulation.

The higher beam current of MDO displayed in Table 6 in comparison to that of PIC is attributed to the theoretical prediction based on Eq. (11). It has subsequently led to higher performance values that have resulted from MDO than PIC with respect to thrust, total efficiency, and specific impulse.

Table 6 Comparison of operation parameters of the S_1 design between MDO prediction and PIC simulation

	I_a [A]	I_b [A]	T [mN]	η_t [%]	I_{sp} [s]
MDO	2.94	3.61	102.7	36.5	2131
PIC	2.66	2.30	62.8	15.2	1333

Table 7 presents the design and performance of the selected points from experimental studies reported in available literature to compares with those from the present study presented in Table 6. These experimental data are used as the reference models for validation. The maximum thrust from MDO has been found to be approximately 102 mN, which is considerably larger than all data from the experimental studies, while the thrust value from PIC (63 mN) is at a similar level to the experimental results from Ma et al.. Qualitative agreement can be seen between the MDO and experimental results in efficiency, specific impulse, anode potential, and anode current. The predicted efficiency and specific impulse from MDO studies are comparable to those from Ma et al. [5], while the efficiency and specific impulse obtained from PIC are reasonably correlated with the experimental results by Young et al. [28]. The anode potentials

Table 7 Comparison of performance and design parameters

Performance parameters	Ma et al. [5]	Young et al. [28]	Courtney et al. [39]	Keller et al. [7]	Kornfeld et al. [6]	Keller et al. [4]
Efficiency η_t (%)	35.4	21.7	44.5	40.7	45	-
Anode Potential U_a (V)	500	300	550	1100	1000	700
Anode Current I_a (A)	4.1	0.37	0.44	-	1.5	-
Mass flow rate \dot{m}_a (scm)	30	8.2	8.5	0.48	17.5	0.59
Thrust T (mN)	66	4.9	13.4	0.36	50	0.19
Specific impulse I_{sp} (s)	2287	1239	1640	860	3000	360
Design parameters						
Number of magnets	3	3	3	3	3	4
IMR (mm)	20	8.75	-	2.2	-	2.2
OMR (mm)	32	23.9	32	15	-	15
Chamber length (mm)	96	39.7	40	-	-	-
Magnet material	2Sm17Co	SmCo	3212SmCo	SmCo	SmCo	SmCo
Propellant	Xe	Kr	Xe	Xe	Xe	Xe
Chamber wall material	BN	BN	BN	BN	BN	BN

from MDO and PIC correlate reasonably to those of Refs. [4, 7]. The anode currents from MDO and PIC are in a range between 1.5 A [7] and 4.1 A [5], while the other experimental studies used much lower anode currents. The mass flow rate is considerably higher in this study due in part to the objective of the research in line with that of Keller et al. [4], who aimed to minimize thrust for precision station keeping applications. However, the experimental evidence did not fully explore the design space, and thus the highly nonlinear relationships between the performance objectives and the decision variables were not understood adequately in previous studies[7]. The design parameters presented in Table 2 are comparable to Young et al. [28] but represent an overall reduction comparable to Ma et al. [5] with improved performance in thrust, consequently leading to reduction in thruster weight.

V. Conclusions and Future Work

An MDO study has been conducted to investigate the characteristics and behavior of the CFT design, aiming to maximize three performance measures, namely, thrust, efficiency, and specific impulse simultaneously. Surrogate models have been built, based on the results from an initial MDO study performed by incorporating magnetic field analysis with power distribution calculation based on the magnetic mirror condition into evolutionary algorithms, and then employed to perform a large-scale, surrogate-based MDO.

Variance-based sensitivity analysis of the MDO results has yielded new insights into the key design factors and underlying physics that play a crucial role in downscaling of CFT models while maintaining high performance. A representative point has been selected from the resultant Pareto optimal front, identified as a candidate for optimal CFT design to achieve most desirable performance metrics. Kinetic analysis has been performed by means of PIC simulation for the selected design in order to verify the results from the MDO study by accurately accounting for the performance losses associated with the uncertainties and complexities of the CFT design and phenomena. Qualitative coherence has been observed between the PIC solution and MDO result for the performance metrics and other key parameters, while considerable differences have been found quantitatively, suggesting the presence of room for improvement left in the modeling of CFT performance to enhance prediction accuracy.

Further investigation is currently underway by probing into the solution from PIC simulation so as to scrutinize the physical characteristics and phenomena that are responsible for the differences including the influence of beam current on thruster performance. The insights to be gained from this collaborative research will be reflected to improve the modeling for performance prediction to enable physics-based MDO considering key physical characteristics that need to be taken into account to realise CFT downscaling for microsatellite platforms.

Acknowledgements

The work of Paul Matthias, Daniel Kahnfeld and Ralf Schneider was funded by the German Space Agency DLR through project 50RS1510.

References

- [1] Goebel, D. M., and Katz, I., “Fundamentals of electric propulsion: ion and Hall thrusters,” , Vol. 1, John Wiley & Sons, 2008.
- [2] Van Noord, J., “Lifetime assessment of the NEXT ion thruster,” AIAA 2007-5274, 43rd AIAA/ASME/SAE/ASEE Joint Propulsion Conference & Exhibit, Cincinnati, OH, Jul 2007, p. 5274. doi:10.2514/6.2007-5274, URL <https://doi.org/10.2514/6.2007-5274>.
- [3] Boyd, I. D., “Simulation of electric propulsion thrusters,” Tech. rep., University of Michigan, Ann Arbor, 2011.
- [4] Keller, A., Köhler, P., Hey, F. G., Berger, M., Braxmaier, C., Feili, D., Weise, D., and Johann, U., “Parametric Study of HEMP-Thruster Downscaling to μ N Thrust Levels,” *IEEE Transactions on Plasma Science*, Vol. 43, No. 1, 2015, pp. 45–53. doi:10.1109/TPS.2014.2321095.
- [5] Ma, C., Liu, H., Hu, Y., Yu, D., Chen, P., Sun, G., and Zhao, Y., “Experimental study on a variable magnet length cusped field thruster,” *Vacuum*, Vol. 115, 2015, pp. 101–107.
- [6] Keller, A., Kohler, P., Feili, D., Berger, M., Braxmaier, C., Weise, D., and Johann, U., “Feasibility of a down-scaled HEMP Thruster,” , Verlag Dr. Hut, 2014.
- [7] Kornfeld, G., Koch, N., and Harmann, H.-P., “Physics and evolution of HEMP-thrusters,” *Proceedings of the 30th International Electric Propulsion Conference*, Florence, Sep 2007, pp. 17–20.
- [8] Eichmeier, J. A., and Thumm, M., “Vacuum electronics: components and devices,” , Springer Science & Business Media, 2008.
- [9] Koch, N., Schirra, M., Weis, S., Lazurenko, A., van Reijen, B., Haderspeck, J., Genovese, A., Holtmann, P., Schneider, R., Matyash, K., et al., “The HEMPT concept-A survey on theoretical considerations and experimental evidences,” 32nd International Electric Propulsion Conference, Vol. 11, Wiesbaden, Sep 2011, p. 15.
- [10] Schneider, R., Matyash, K., Kalentev, O., Taccogna, F., Koch, N., and Schirra, M., “Particle-in-Cell Simulations for Ion Thrusters,” *Contributions to Plasma Physics*, Vol. 49, No. 9, 2009, pp. 655–661.
- [11] Genovese, A., Lazurenko, A., Koch, N., Weis, S., Schirra, M., van Reijen, B., Haderspeck, J., and Holtmann, P., “Endurance testing of HEMPT-based ion propulsion modules for smallGEO,” 32nd International Electric Propulsion Conference, Vol. 11, Wiesbaden, Sep 2011, p. 15.
- [12] Hofer, R., and Gallimore, A., “Efficiency analysis of a high-specific impulse Hall thruster,” AIAA 2004-3602, 40th AIAA/ASME/SAE/ASEE Joint Propulsion Conference and Exhibit, Fort Lauderdale, FL, Jul 2004, p. 3602. doi:10.2514/6.2004-3602, URL <https://doi.org/10.2514/6.2004-3602>.
- [13] Matlock, T. S., “An exploration of prominent cusped-field thruster phenomena: the hollow conical plume and anode current bifurcation,” Ph.D. thesis, Massachusetts Institute of Technology, 2012.
- [14] Howard, J., “Introduction to Plasma Physics C17 Lecture Notes,” 2002, Available online: people.physics.anu.edu.au/~jnh112/AIIM/c17/chap04.pdf [retrieved 15 Apr 2018].
- [15] Gallimore, A., “The Physics of Spacecraft Hall-Effect Thrusters,” APS Division of Fluid Dynamics Meeting Abstracts, 2008.
- [16] Fahey, T., Muffatti, A., and Ogawa, H., “High Fidelity Multi-Objective Design Optimization of a Downscaled Cusped Field Thruster,” *Aerospace*, Vol. 4, No. 4, 2017, p. 55.
- [17] ANSYS Inc, *ANSYS Electronics Desktop Suite ver.17.2 Users’ Guide*, 2016.
- [18] Deb, K., Pratap, A., Agarwal, S., and Meyarivan, T., “A fast and elitist multiobjective genetic algorithm: NSGA-II,” *IEEE transactions on evolutionary computation*, Vol. 6, No. 2, 2002, pp. 182–197.
- [19] Ray, T., Isaacs, A., and Smith, W., “Multi-objective optimization using surrogate assisted evolutionary algorithm,” *Introduction (G.P. Rangaiah), Multi-objective Optimization: Techniques and Applications in Chemical Engineering*, 2008, pp. 131–151.

- [20] Lloyd, S., "Least squares quantization in PCM," *IEEE transactions on information theory*, Vol. 28, No. 2, 1982, pp. 129–137.
- [21] Box, G. E., and Wilson, K. B., "On the experimental attainment of optimum conditions," *Breakthroughs in statistics*, Springer, 1992, pp. 270–310.
- [22] Buhmann, M. D., "Radial basis functions: theory and implementations," , Vol. 12, Cambridge university press, 2003.
- [23] Rosenblatt, F., "Principles of neurodynamics. perceptrons and the theory of brain mechanisms," Tech. rep., Cornell Aeronautical Laboratory, Inc., Buffalo, NY, 1961.
- [24] Krige, D. G., "A statistical approach to some mine valuation and allied problems on the Witwatersrand: By DG Krige," Ph.D. thesis, University of the Witwatersrand, 1951.
- [25] Queipo, N. V., Haftka, R. T., Shyy, W., Goel, T., Vaidyanathan, R., and Tucker, P. K., "Surrogate-based analysis and optimization," *Progress in Aerospace Sciences*, Vol. 41, No. 1, 2005, pp. 1–28.
- [26] Sobol', I., "Uniformly distributed sequences with additional uniformity properties," *USSR Computational mathematics and mathematical physics*, Vol. 16, 1976, pp. 1332–1337.
- [27] Saltelli, A., Ratto, M., Andres, T., Campolongo, F., Cariboni, J., Gatelli, D., Saisana, M., and Tarantola, S., "Global sensitivity analysis: the primer," , John Wiley & Sons, 2008.
- [28] Young, C. V., Smith, A. W., and Cappelli, M. A., "Preliminary characterization of a diverging cusped field (DCF) thruster," *Proceeding of 31st International Electric Propulsion Conference*, Ann Arbor, MI, 2009.
- [29] Courtney, D. G., "Development and characterization of a diverging cusped field thruster and a lanthanum hexaboride hollow cathode," Ph.D. thesis, Massachusetts Institute of Technology, 2008.
- [30] NASA CubeSat Launch Initiative, "CubeSat 101 Basic Concepts and Processes for First-Time CubeSat Developers," 2017.
- [31] Matyash, O. K., Schneider, R., Taccogna, F., Koch, N., and Schirra, M., "Kinetic simulation of the stationary HEMP thruster including the near-field plume region," *Proceedings of the 31st International Electric Propulsion Conference*, 2009, pp. 20–24.
- [32] Kalentev, O., Matyash, K., Duras, J., Luskow, K. F., Schneider, R. E., Koch, N., and Schirra, M., "Electrostatic Ion Thrusters - Towards Predictive Modeling," *Contributions to Plasma Physics*, Vol. 54, No. 2, 2014, pp. 235–248. doi:10.1002/ctpp.201300038.
- [33] Kornfeld, G., Koch, N., and Coustou, G., "FIRST TEST RESULTS OF THE HEMP THRUSTER CONCEPT," The 28th International Electric Propulsion Conference, 2003.
- [34] Boris, J. P., "Relativistic plasma simulation-optimization of a hybrid code," *Proceeding of 4th Conference on Numerical Simulations of Plasmas*, 1970.
- [35] Tskhakaya, D., Matyash, K., Schneider, R., and Taccogna, F., "The Particle-In-Cell Method," *Contributions to Plasma Physics*, Vol. 47, No. 8-9, 2007, pp. 563–594.
- [36] Hayashi, M., "Bibliography of Electron and Photon Cross Sections with Atoms and Molecules Published in the 20th Century - Xenon," Tech. Rep. NIFS-DATA-79, NIFS, 2003. URL <http://www.nifs.ac.jp/report/NIFS-DATA-079.pdf>.
- [37] Komurasaki, K., Hirakawa, M., and Arakawa, Y., "Plasma acceleration process in a Hall-current thruster," 22nd International Electric Propulsion Conference, Viareggio, Italy, 1991.
- [38] Martinez-Sanchez, M., and Lozano, P., "16.522 Space Propulsion," , Spring 2015. URL <https://ocw.mit.edu>.
- [39] Courtney, D., Lozano, P., and Martinez-Sanchez, M., "Continued investigation of diverging cusped field thruster," AIAA 2008-4631, 44th AIAA/ASME/SAE/ASEE Joint Propulsion Conference & Exhibit, Hartford, CT, Jul 2008, p. 4631. doi: 10.2514/6.2008-4631, URL <https://doi.org/10.2514/6.2008-4631>.

ORIGINAL ARTICLE

Particle-in-cell simulation of an optimized high-efficiency multistage plasma thruster

Paul Matthias¹  | Daniel Kahnfeld¹ | Ralf Schneider¹ | Suk Hyun Yeo² | Hideaki Ogawa^{2,3}¹Institute of Physics, University of Greifswald, Greifswald, Germany²School of Engineering, RMIT University, Melbourne, Victoria, Australia³Department of Aeronautics and Astronautics, Graduate School of Engineering, Kyushu University, Fukuoka, Japan**Correspondence**Paul Matthias, Institute of Physics, University of Greifswald, Felix-Hausdorff-Str. 6, Greifswald D-17489, Germany.
Email: pm101481@uni-greifswald.de**Present address**

Paul Matthias, ABS gGmbH Seniorenberatungsstelle, Trelleborger Weg 17, 17493 Greifswald, Germany.

Funding information

Australian Government Research Training Program; Deutsches Zentrum für Luft- und Raumfahrt, 50RS1510

Abstract

Electric propulsion attracts increasing attention in contemporary space missions as an interesting alternative to chemical propulsion because of the high efficiency it offers. The High-Efficiency Multistage Plasma thruster, a class of cusped field thruster, is able to operate at different anode voltages and operation points and thereby generate different levels of thrust in a stable and efficient way. Since experiments of such thrusters are inherently expensive, multi-objective design optimization (MDO) is of great interest. Several optimized thruster designs have resulted from a MDO model based on a zero-dimensional (0D) power balance model. However, the MDO solutions do not warrant self-consistency due to their dependency on estimation from empirical modelling based on former experimental studies. In this study, one of the optimized thruster designs is investigated by means of particle-in-cell (PIC) analysis to examine the predicted performance characteristics with self-consistent simulations. The 0D power balance model is used to develop additional diagnostics for the PIC simulations to improve the physics analysis. Using input parameters for the 0D power balance model from the PIC simulations allows further improvement for the design optimization.

KEYWORDS

cusped field thruster, electric propulsion, multi-objective design optimization, particle-in-cell, plasma simulation

1 | INTRODUCTION TO HEMP THRUSTERS

The high efficiency multistage plasma thruster (HEMP-T)^[1] is a class of ion propulsion devices for space systems contrived by Thales Deutschland GmbH.

The HEMP-T thrusters are composed of a cylindrical discharge channel with a dielectric material at the walls. The dielectric has a high sputtering threshold, such as Boron Nitride. The source of the neutral gas is positioned at the centre of the metal anode at the channel bottom.^[2] A number of ring magnets with pairwise opposite magnetization directions, force a cusp structure of the magnetic field in the discharge channel. It consists of a flat magnetic field at the symmetry axis of the channel and magnetic bottles (cusps) between the ring magnets. The general design concept of a HEMP-T is shown in Figure 1.

The discharge is fed by a cathode neutralizer, which emits electrons in the plume area outside the discharge channel. The positive anode and plasma potential create an electric field, which accelerates the electrons towards the channel. The electrons are magnetized in the channel. In the direction parallel to the symmetry axis the electron transport is strong, because of the axial magnetic field between the cusps, leading to a flat electrostatic potential stretching from the anode to the exit of the thruster.

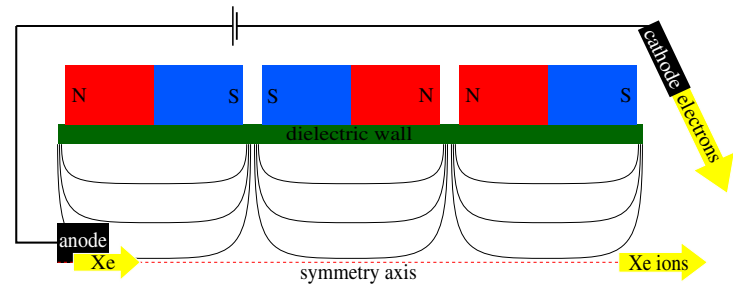


FIGURE 1 Schematic of a HEMP thruster

The radial magnetic field at the cusps acts like a magnetic bottle. This ensures the reflection of the electrons, while keeping the wall losses to a minimum. As a consequence of the reflection of electrons, the electron temperature in the cusp rises. Only the electrons with very high energies can reach the wall, reducing in the total wall losses by the cusp. Additionally the secondary electrons emitted from the dielectric get accelerated in the sheath, resulting in a rise in electron temperature in the cusps. The confinement of the electrons results in high ionization rates. The heavier ions are non-magnetized. In the discharge channel they follow the electrons and have low energies, keeping the wall contact and therefore sputtering rates small. Only further downstream in the exit region, where the plasma potential drops to vacuum potential, the ions are accelerated and emitted. This generates the thrust. As a whole, HEMP-Ts are efficient electric propulsion devices generating thrust in a wide range of $1 \mu\text{N} - 100 \text{mN}$ and high specific impulses of 2000s , while reducing sputtering erosion and wall losses. This makes the HEMP-T an appealing concept for long-term space missions.^[3]

Xenon is commonly used as a propellant and considered in this work. It is usually injected with influx rates in the range of $1-50 \text{sccm}$ at the anode. The applied anode voltage is in the range of $100-2000 \text{V}$. More information on HEMP-Ts can be found in Koch et al.^[2]

Since the general design concept was established, several studies have been conducted on the scaling of the systems, aiming to serve a wide variety of space mission profiles.^[3,4] These preceding studies were based on experiments, which are an inherently expensive design optimization process. Simulation serves as an affordable method for this and are used increasingly, for example, in car industry.^[5,6] Kinetic simulations such as particle-in-cell (PIC) are commonly used to simulate low temperature plasmas, like they are used in ion thrusters.^[7-9] The advantage of this microscopic method is the rather complete inclusion of physics, albeit considerably long run time are required for simulations. To ensure physical accuracy the smallest length and time scales of the discharge have to be resolved, which are the electron Debye length and the plasma frequency in thruster physics. The necessary scales are comparably small considering the large length and time scales, which have to be covered by the simulation. Therefore, PIC simulations are too time consuming to explore a wide variety of thruster designs and other methods are used to optimize thruster designs. Multi-objective design optimization (MDO) represents a new design approach that enables effective search in the design space to optimize the system for performance parameters of primary interest, namely thrust, specific impulse, and total efficiency. The variation parameters used as a basis for the calculation of these performance parameters are the anode voltage, the anode current, the neutral gas mass flow rate, and the inner and outer magnet radii. Each set of these basic parameters defines a different thruster design with a different performance. An MDO study was successfully conducted by coupling evolutionary algorithms with performance analysis incorporating magnetic field simulation, achieving robust global optimization to identify key design parameters and mechanism for HEMP-T scaling.^[10] The performance was estimated by using a zero-dimensional (0D) power balance equation system for particles, energy, and momentum,^[3] but some parameters inevitably had to rely on empirical assumptions, rendering it difficult to ensure self-consistency in the system. Empirical assumptions in this case include constant power transfer coefficients, which were originally assumed for a different HEMP-T geometry. In addition other important effects are neglected in the 0D power balance model, especially the influence of neutral gas distribution, ionization efficiency, doubly charged ions, and the details of the ion beam structure. This does not lead to self-consistent solutions of the MDO, but with the application of empiric correction terms, which take into account the neglected effects, the MDO derived several thruster designs, among which a most promising design, called the S_1 thruster,^[10] is considered in the present study.

In this work this optimized MDO thruster design S_1 is studied with PIC simulations. Firstly, PIC is introduced, followed by the setup of the simulation for the S_1 . The resulting physics characteristics of the S_1 are then compared to other HEMP designs and evaluated. The 0D power balance model is employed to develop additional diagnostics modules to gain further insights to the underlying physics in the S_1 . These diagnostics results are used to compare the estimated MDO input parameters to the ones obtained with the PIC simulation. Finally, the results and key findings are summarized.

2 | PARTICLE-IN-CELL MODEL

2.1 | Modelling approach

The electron mean-free paths in HEMP-Ts are of the same range as the system size and kinetic effects in the magnetic cusps create non-Maxwellian perturbations of the electron distribution function.^[11] Hence, a kinetic simulation of the system is necessary for accurate analysis.^[12,13] In this work an electrostatic 2D3v PIC method with a Monte Carlo Collision model^[14] is applied. The simulation is electrostatic, because the internal thruster currents induce negligible magnetic fields compared to the field applied by the ring magnets. As a result of the cylindrical symmetry of the thruster the simulation uses cylindrical coordinates (r, z) . The simulation domain covers the channel and the near exit region. The velocity space is three dimensional for energy and momentum conservation of the collisions.^[14] The dynamics of electrons e^- , neutrals Xe, singly charged ions Xe^+ , and doubly charged ions Xe^{2+} are resolved. The density of doubly charged ions is only a small fraction ($\approx 10\%$) of the singly charged ions. In typical measurements of the HEMP-T the density of higher charged xenon ions is even lower than doubly charged ions ($<1\%$).^[11] Therefore, higher charged xenon ions are neglected in the simulation. Because of the large number of plasma particles, super particles are introduced, each representing a large number of real particles with the same charge-to-mass ratio as the real particles, which results in identical trajectories. This reduces the computation time, owing to significant reduction of particles to be followed.

The PIC model resolves the dynamics of the particles by following the algorithm schematically shown in Figure 2.

For the PIC model a grid has to be applied to the domain. The charge density of the super particles is weighted onto the grid points with a Cloud-In-Cell (CIC) scheme.^[15] Afterwards, the Poisson equation is solved on the grid using the weighted charge density with the *SuperLU* package,^[16] calculating the electric potential. The Lorentz force acting on the particles is computed by weighting the fields on the particles in the cells by using the same CIC scheme to conserve energy and momentum. The particles are then moved using the Boris algorithm.^[17] In comparison to the electrons, heavier particle species have much lower velocities. In this case, sub-cycling can be applied for the ions and neutrals,^[14] which means that they are only moved every n th timestep. For the charged particle species the electric field is averaged between the sub-cycling steps. This leads to a decrease in computing time. Particle boundary effects are also considered in the particle mover.

After the movement the collisions are simulated using Monte Carlo Collisions. In this model direct single and double e^- -Xe impact ionization, single e^- - Xe^+ impact ionization, integral elastic Xe^+ -Xe collisions (including charge exchange and momentum transfer), and integral elastic and inelastic e^- -Xe collisions^[11] are included. Integral collisions here refer to a combined cross section for the possible elastic collisions which can occur.

The PIC algorithm guarantees a physically correct solution if the Debye length and the plasma frequency are resolved,^[18] while satisfying the Courant-Friedrichs-Lewy condition.^[19] Further information about the PIC method applied in this work can be found in the works of Tskhakaya et al and Kahnfeld et al.^[14,20]

A way to reduce computation time for large systems is similarity scaling.^[21] For kinetic systems like low temperature plasma it is derived from the Boltzmann equation, which describes the distribution function of all plasma species, and the Maxwell equations. Two systems are similar, if the physical parameters scale linearly from one system to the other, for example, the system size. Taking into account the Boltzmann and Maxwell equations, six invariants emerge. The most important invariants for the application on electrostatic systems like ion thrusters are the Hall parameter and the Knudsen number. The first one describes the effect of magnetization on the charged particles, the second one the effect of collisions, in particular ionization. For PIC simulations the system size is a limiting factor, due to higher particle numbers and larger grids. Therefore, a scaling of the system size is introduced, where the velocities and densities remain non-scaled, but the system size and the time scale down linearly. This leads to fewer cells and particles which have to be traced in comparison to the unscaled system, resulting in lower

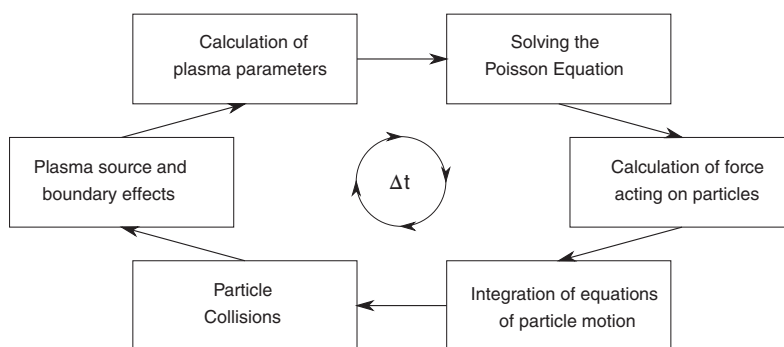


FIGURE 2 Schematic diagram of the PIC cycle

TABLE 1 Most important quantities in the self-similarity scaling scheme. The scaling factor is ξ

Quantity	Scaling law
Length scale	$x = \tilde{x} \xi$
Time scale	$t = \tilde{t} \xi$
Velocity	$v = \tilde{v}$
Collision cross section	$\sigma = \tilde{\sigma} \xi^{-1}$
Magnetic field	$B = \tilde{B} \xi^{-1}$
Number density	$n = \tilde{n}$

computation time. In Table 1 the most important scalings are shown as applied in the PIC simulation. With the chosen similarity scaling, all volume processes and wall fluxes are conserved, leading to exact solutions in the plasma volume. The limit of the application is the sheath to plasma volume ratio, since the plasma sheath does not scale. If the influence of the sheath is too big, lower scaling factors have to be chosen. An detailed study of the similarity scaling, its application and limits to ion thrusters can be found in works of Lacina and Matthias et al.^[22,23]

2.2 | Simulation setup

The S_1 thruster design has an inner magnet radius of 9.91 mm, an outer magnet radius of 25.1 mm, and a channel length of 21 mm. The ring magnets lead to three cusps at the axial positions $z = 4.5$ mm and $z = 17$ mm and one cusp downstream from the exit plane. An electron density of $n_e = 1 \times 10^{14} \text{ cm}^{-3}$ and a mean electron temperature of $T_e = 10$ eV in the channel are used as reference parameters for the calculation of the Debye length and the plasma frequency which are used to calculate the grid spacing and time step, respectively. The resulting spatial resolution of the grid is $dr = 1.76 \times 10^{-4}$ cm with a time step of $dt = 8.9 \times 10^{-14}$ s. Taking into account the system size of the S_1 design, the domain size is chosen as $r = 20$ mm and $z = 50$ mm to resolve the channel and the near exit region, resulting in a computational grid of 283×709 cells (r, z) with an applied self-similarity scaling factor of $S_F = 40$. The chosen similarity scaling factor ensures solutions, where the influence of the non-scaling plasma sheath is still low, so that the plasma volume solution remains close to the non-scaled system.^[21] In the scaled system one super particle represents 573 real particles resulting in 8×10^6 charged and 20×10^6 neutral simulated particles. The anode voltage is set at $U_a = 1000$ V at the left domain boundary according to the optimal operating parameters of S_1 . The top domain boundary and the metal coating around the thruster is grounded and the right-hand side domain boundary at $z = 50$ mm is set to a constant axial electric field $E_z = 0$ simulating a vacuum boundary.

Particle boundary conditions are applied, including secondary electron emission with a secondary electron emission yield of 0.5 and thermal ion/neutral recycling at the dielectric, thermal ion/neutral recycling at metal boundaries and the deletion of particles leaving the computational domain. The neutral xenon propellant source is located at the center of the anode, where the neutral particles are injected into the thruster channel with a half-Maxwellian velocity distribution and a mass flow rate of $\dot{m}_a = 50$ sccm. A neutralizer as a primary source of electrons is applied in the simulation to maintain the plasma in the channel. In the real system the mass flow rate is given as a control parameter for the system, which results in a specific anode current. The neutralizer current adapts accordingly to the same strength as the anode current to avoid electrostatic charging of the thruster. This adaption of the neutraliser current is a non-linear process and happens on a large timescale, compared to the time resolution of PIC. In the simulation it is therefore more feasible to set the electron source current of the neutralizer to match the wanted anode current. In this case, a constant electron current of 800 mA is injected over the right domain boundary. The anode current with the chosen neutralizer strength is slightly lower than the predicted current from the MDO, but with a deviation of $<10\%$ the PIC simulation is a valid representation of the chosen operating mode. With this setup the PIC simulation is now used to investigate the physical properties of the S_1 .

3 | RESULTS

3.1 | PIC analysis

Using the PIC code described before, the S_1 design has been analysed and its main characteristics is discussed in this section. The electron density distribution is shown in Figure 3, which drops quickly in the plume because of the loss of confinement

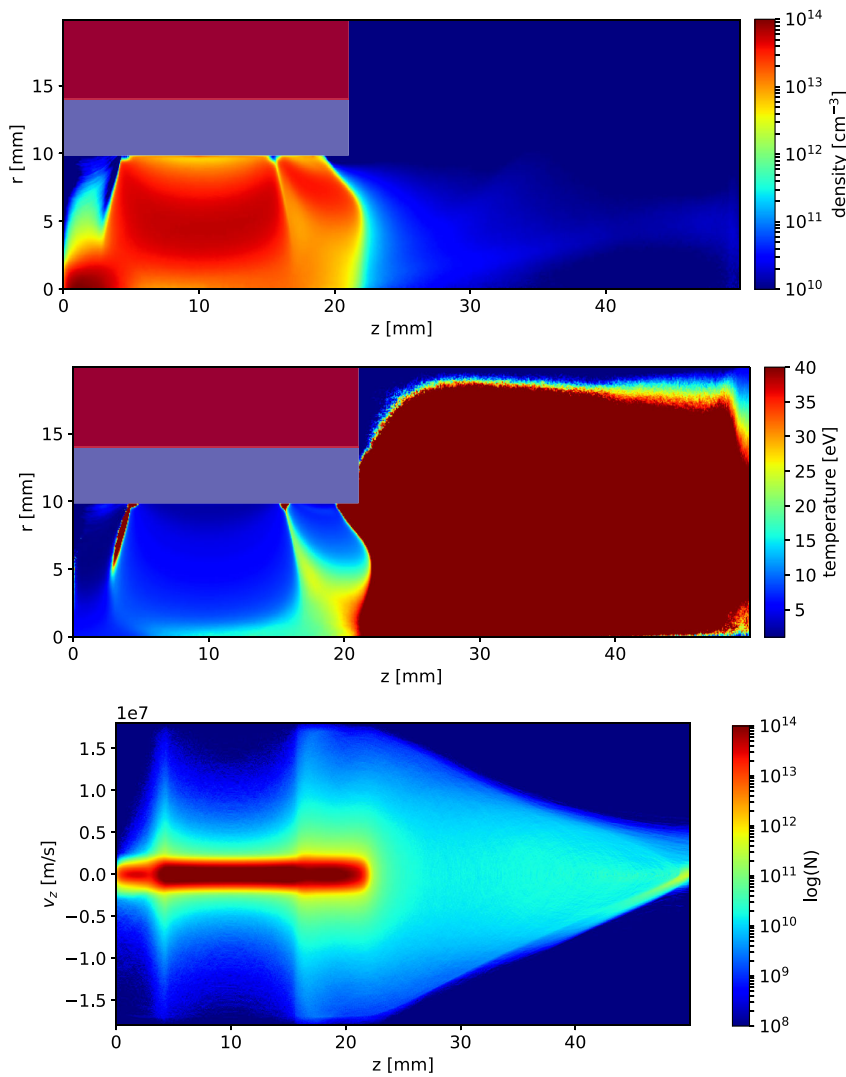


FIGURE 3 The electron density (top), temperature (middle) and axial velocity (bottom) distribution of the S_1 thruster. The electron source is located at the right domain boundary providing a constant current of electrons of $I_e = 800$ mA. The grey box at $r = 9.91\text{--}14$ mm represents the dielectric covering the magnets and is in direct contact to the channel plasma. The red box at the top left of the domain represents the grounded metal surrounding the thruster

for electrons and ions there. The plume electrons drift slowly from the primary source towards the channel exit and become magnetized in the magnetic field. Close to the exit the electrons are accelerated into the channel by the strong axial electric field.

By scattering collisions and anomalous diffusion, transport across magnetic field lines occurs. The anomalous transport is a 3D effect and to apply it in the 2d3v PIC-MCC model an effective anomalous transport coefficient is used for a random walk model in the velocity space.^[11] This model is similar to a Bohm-like diffusion, with the transport coefficient D scaling with the electron temperature T_e and the inverse of the magnetic field $D \propto T_e/B$. With self-consistent 3D simulations the value of the diffusion coefficient was deduced.^[11] The resulting electron energy diffusion perpendicular to the magnetic field lines increases, leading to a transport of the electrons from the outer to the inner magnetic bottle. Accordingly the anomalous transport is important in the cusp regions, where it is responsible for filling the thruster channel, since it increases the probability of electrons traversing the cusp and stream towards the anode.

Inside the thruster channel collisions lead to a decrease of the mean energy with increasing distance to the thruster exit. At the cusps, low energy electrons are reflected and the electron mean energy rises towards the channel wall. With rising mean energy of the electrons, the electron temperature rises in the cusps. Few of the high energy electrons, which are not reflected by the magnetic bottle, hit the wall and lead to secondary electron emission. By the small potential drop at the sheath of approximately 10 V the secondary electrons are accelerated towards the channel plasma, leading to an additional increase of the electron temperature in the cusp region. The total effect of the cusp heating can be seen in the electron temperature distribution in Figure 3. Figure 3 also shows the hot electrons in the plume, where they are accelerated by the strong electric field in front of the thruster exit. Additionally the cool channel area can be seen, where electrons cool down due to collisions with the neutrals and also the local heating effect at the cusp, which is a result of the magnetic mirror effect, is visible.

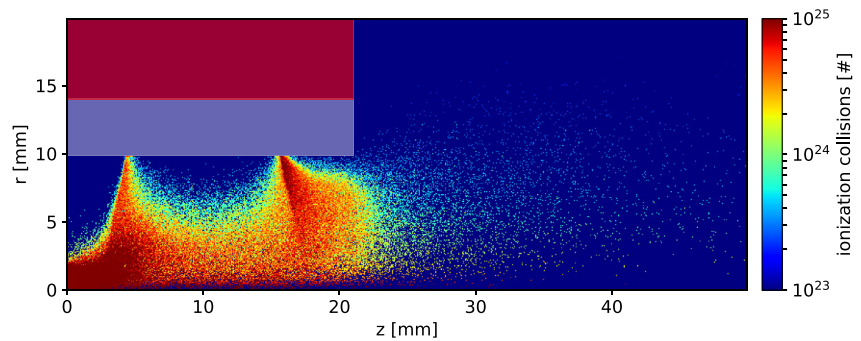


FIGURE 4 Ionization collisions of the S1 thruster

As in other laboratory low temperature plasmas, the mean electron energy (Figure 3) in the thruster channel is in the same range of 1–10 eV, while also populating the higher energy states above 10 eV. In the electron axial velocity distribution EVD in Figure 3, one can see the high energy tail of the electrons in the channel, which is mainly responsible for ionization. The mean electron energies are below the single impact ionization collision threshold energy $E_{\text{ionize}} = 12.13$ eV of xenon.^[24] It follows that only the high energy electrons of the hot tail of the energy distribution function contribute to the ionization. This can be seen when comparing the electron energy distribution in Figure 3 and the ionization collisions in Figure 4. From the data it is evident, that the ionization of xenon mainly occurs at the axis and in the cusp region, where the electrons with the highest energies are located. Additionally strong ionization occurs close to the neutral source at the anode, due to the very high neutral gas density and the therefore increased collision probability.

Because of their high energy the mean free path of the electrons is high and losses occur at the intersection of the magnetic field lines and the channel wall, that is, at the cusps. Only at the cusps in the channel the plasma connects to the wall. However, wall losses are small because the electrons are reflected by the magnetic mirror there. This results in a pendulum motion of the electrons between the cusps, where they are trapped and move along the magnetic field lines, which are mostly parallel to the symmetry axis. The symmetric axial EVD in the channel is a consequence of the electron trapping. The good electron confinement leads to an increased ionization efficiency and high ionization rates in the plasma channel.

As a result of quasi-neutrality in the plasma the ion density distribution is similar to the electrons, as seen in Figure 5. The ions drift slowly in the thruster channel and are accelerated at the exit leaving the thruster with a certain angular distribution. The low energies of the ions in the channel lead to very low sputtering rates.^[2] The generated thrust strongly depends on this angular ion current distribution, which will be discussed later in detail. The strong electric field at the thruster exit accelerates the ions towards the anode potential. Because of the grounded coating of the thruster the ions in the plume with high emission angles get accelerated towards the metal coating of the thruster. This is shown by the ions in the IVD with negative axial velocities downstream, as observed in the region ranging from $z = 21$ – 26 mm, as shown in Figure 5. The particle number of the doubly charged xenon ions is only 10.8% of that of the singly charged ions. They are emitted with the same angular profile as the singly charged ions, while they receive double the energy through the electric field at the exit. Otherwise they behave like the singly charged ions and are not considered further in the following discussions, except their contribution to the thrust.

Figure 6 displays the electric potential in the simulation of the S_1 . The flat potential in the channel and the steep potential drop close to the exit region ($z \approx 25$ mm) are present. The dominant axial transport of the electrons near the axis with a strong axial magnetic field leads to a flat potential in the thruster channel. The contact of the plasma to the wall is limited to the intersection of the magnetic field lines with the dielectric wall. In the other regions the wall contact of electrons is significantly reduced. As a result, a positive surface charge is building up at the wall contact regions from the impinging ions, which leads to a potential at the wall in the same range as the plasma potential. The applied dielectric extends to the exit of the S_1 and even covers the outside surface of the thruster. Due to the magnetization and the geometry of the magnetic field lines, the electrons do not impinge on the outer surface of the dielectric. Therefore, mostly exiting ions impinge on the outer dielectric surface, lead to a positive surface charge and to an increase of the potential in the near exit region. The influence of the grounded metal coating of the thruster is rather weak, because of the larger distance away from the plasma and the compensation of the influence due to the surface charge building up at the dielectric. As a consequence the potential expands into the plume and results in a nearly isotropic potential drop outside of the thruster. At the exit the potential drops as a result of lower plasma densities until it reaches vacuum potential, which is typical of HEMP-Ts.^[2] This is similar to gridded ion thrusters but without a grid at the thruster exit.

The resulting electric field accelerates the neutralizer electrons towards the thruster channel and leads to strong ionization in the exit region. The neutral density distribution drops accordingly close to the thruster exit (see Figure 7). Additionally, a higher local neutral density at the cusps in the channel can be observed. Here, the plasma wall contact produces thermal neutral xenon particles by recycling of impinging ions.

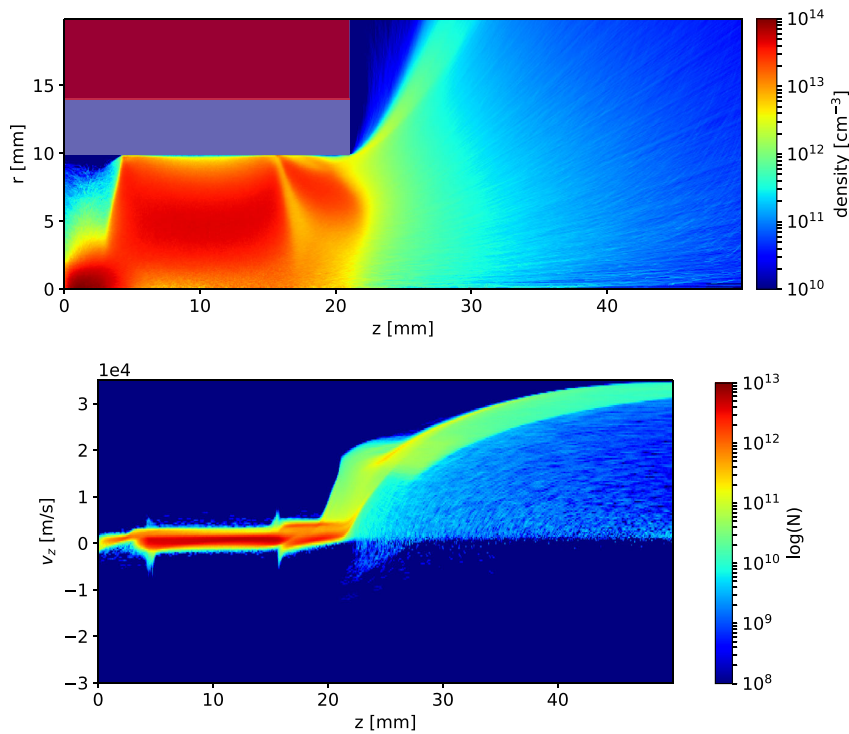


FIGURE 5 Xe⁺ density (top) and axial velocity (bottom) distribution of the S₁ thruster

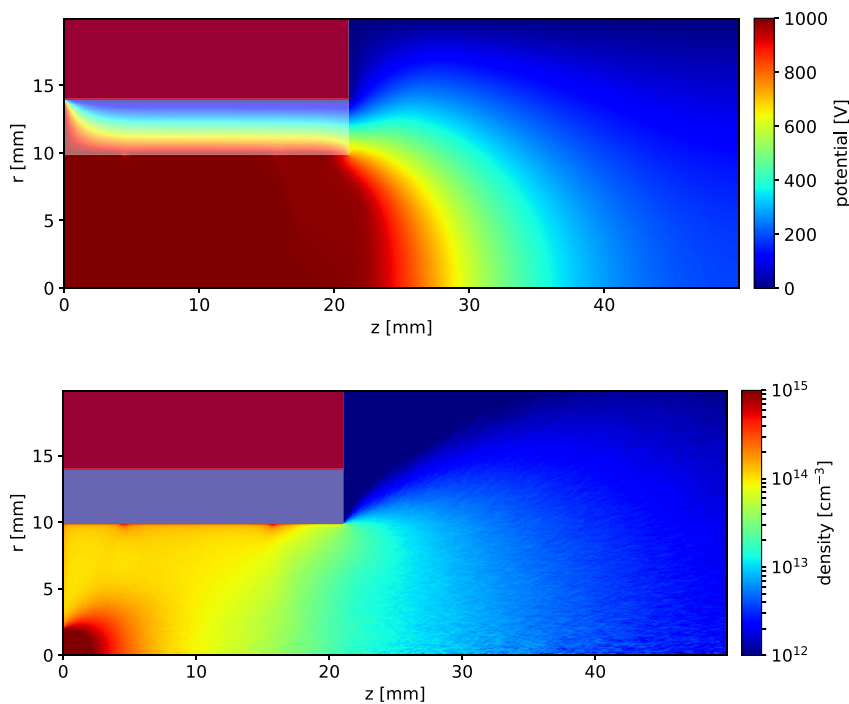


FIGURE 6 The electric potential in the channel and the near plume region in the S₁ thruster. The anode is located at $z = 0$ mm and reaches from $r = 0$ –9.91 mm

FIGURE 7 Neutral xenon density distribution in the S₁ thruster. The gas inlet is located at $r = z = 0$ mm and releases 50 sccm of neutral xenon gas in the channel with a half-Maxwellian velocity distribution

One of the most important characteristics of ion thrusters is the angular ion current distribution in Figure 8. It shows the ion current expelled by the thruster as a function of the different emission angles. Low emission angles improve the efficiency of a thruster, since they result in higher axial to radial energy ratios and minimize interaction with the satellite components. The angular current slowly rises with higher angles and peaks at 65°, which is similar to other HEMP-Ts with mean exit angles of $\approx 60^\circ$.^[2]

To understand the composition of the angular ion current distribution, the dependency of the ion origins and emission angles must be considered. This is achieved by storing each particle's location at creation and registering the particle in the angle bin when it leaves the domain.^[8] The results are visualized in Figure 8. For angle bins of 10° in the range of 0–90°, the main areas of origin per angle bin are shown with a confidence interval from 30 to 70%. The ions produced in the channel and near the

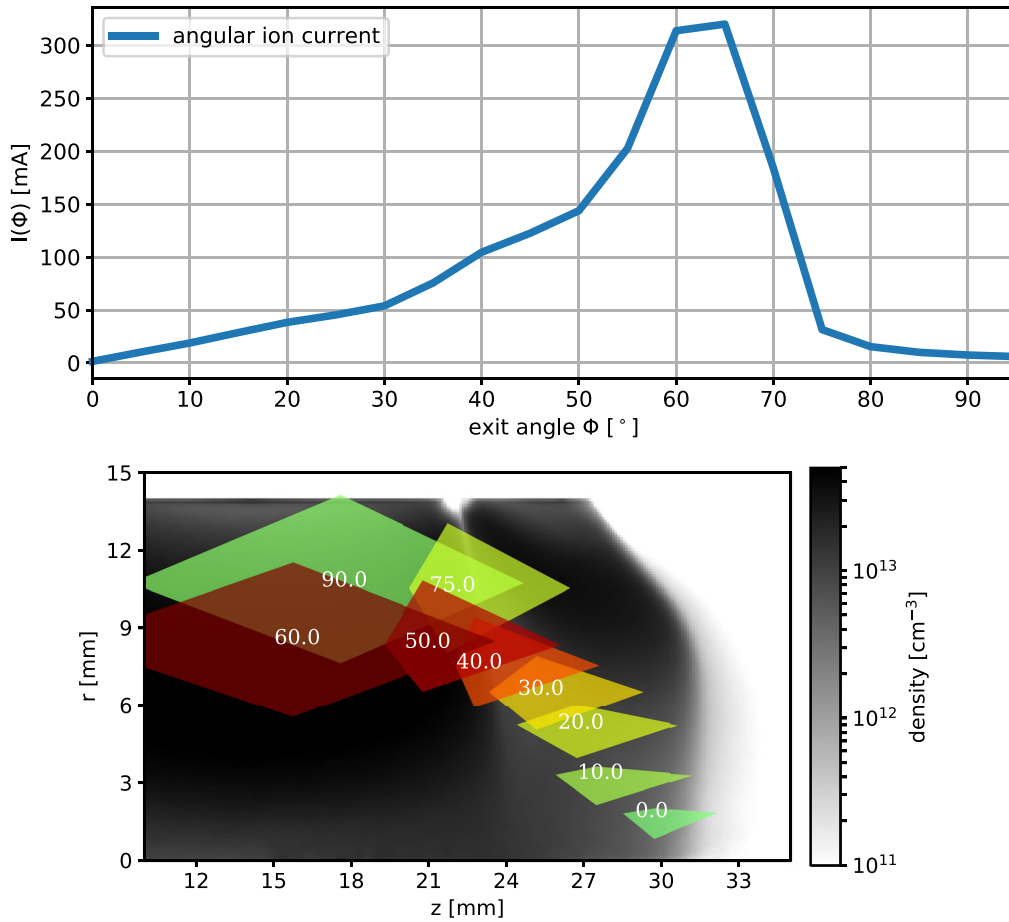


FIGURE 8 Angular ion current distribution of the S_1 thruster (top) and the mean Xe^+ ionization origins for specific angles of the angular current distribution (bottom). The colour of the patches indicate the ratio from the specific angle to the total beam current, from low (green) to high (red). In the background the electron density distribution at the channel exit is shown in grayscale

symmetry axis undergo a higher axial electric field contributing to lower angles, while ions created away from the axis near the exit region experience a more radially oriented electric field (see Figure 8) populating the higher angle bins. Because of the high mass flow rate of 50 sccm leading to a high neutral density in the channel the plasma extends towards the exit, leading to an increased potential at the exit. This results in a higher ion mean emission angle and thus, as already discussed, reducing the contribution to the thrust.

To improve the emission characteristics it would be better to increase the channel length. The neutral density towards the channel exit would further decrease while the mean free path of the electrons increases. The potential would shift into the channel instead of downstream from the exit. This would result in smaller emission angles, as discussed in the study of Kahnfeld et al.^[25] However, an increased channel length would result also in increased wall losses and hence in a reduction in the efficiency. Therefore, the channel length should be considered as an additional optimization parameter to identify the optimum ratio between emission angle and efficiency in the MDO.

Another way to improve the beam structure would be to opt for a lower anode current and therefore lower plasma density scenarios, while keeping the mass flow rate constant. This is realized by a lower neutralizer current in the simulation (Figure 9). Higher neutralizer currents lead to higher emission angles while increasing the beam current, too. The increased ion beam current gives higher ionization and therefore higher efficiency. The dependency of the anode current on the operating state is yet to be considered in the MDO.

To compare the PIC results to the MDO, the calculation of the performance parameters thrust T , efficiency η_t and specific impulse I_{sp} is required. For discrete angle bins i the thrust is calculated^[26] as

$$T(\Phi) = \sum_i m_i v_{i,\text{exit}} \cdot \cos(\Phi_{i,\text{exit}}), \quad (1)$$

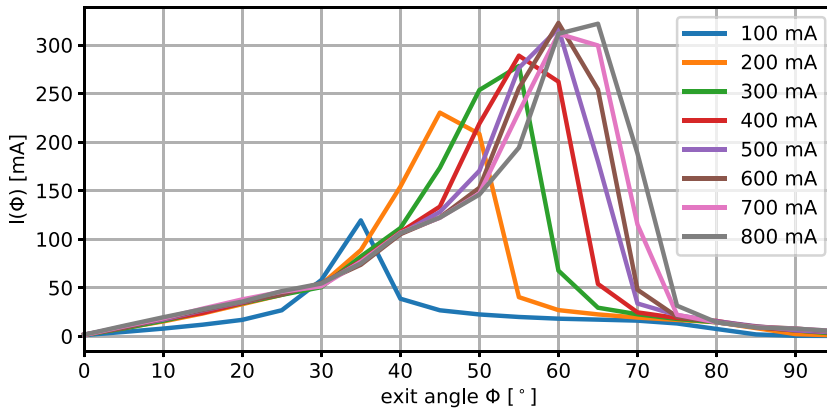


FIGURE 9 Angular Xe^+ current distribution for different neutralizer currents

with \dot{m}_i the ion mass flow leaving the the domain, $v_{i, \text{exit}}$ the emitted ion velocity and $\Phi_{i, \text{exit}}$ the emission angle of the ion. The potential at the simulation domain boundary is not at vacuum potential, leading to lower ion exit velocities when they leave the simulation domain. Using the potential at the domain boundary, an additional correction term for the ion velocities is applied in a postprocessing step. The corrected ion velocities are used in the calculation of the thrust. The specific impulse

$$I_{\text{sp}} = \frac{T}{\dot{m}_{\text{Xe}} g} \quad (2)$$

with \dot{m}_{Xe} the mass flow of the neutral source and $g = 9.81 \text{ m/s}^2$, can be calculated directly from the obtained thrust. The efficiency η_t in the MDO is the anode efficiency.^[10]

$$\eta_t = \frac{T^2}{2\dot{m}_{\text{Xe}} U_a I_a}, \quad (3)$$

with the anode voltage U_a and the anode current I_a .

The calculated performance parameter of PIC in Table 2 show significant differences from the MDO values, even in consideration of the 10% deviation of the anode current.

In the MDO the mean ion emission angle, energy transfer coefficients and cusp arrival probabilities of the electrons, were treated as constant input parameters obtained from experimental measurements of a different HEMP-T model.^[3,10] The different thruster geometry and operating conditions makes the validity of this approach uncertain. This is confirmed by the differences between the predicted performance parameters from the MDO and PIC, seen in Table 2. To investigate these differences, the input parameters from the MDO are reproduced using the kinetic information of the PIC simulation. For this reason new diagnostic routines are implemented in the PIC simulations based on the 0D power balance model.^[3] Afterwards the parameters obtained are compared to the input values used in the MDO.

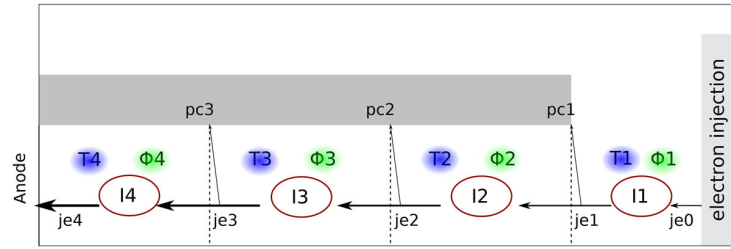
3.2 | 0D power balance diagnostic in PIC

The equations of the 0D power balance model, given by Kornfeld et al.^[3] are outlined below. The parameters used in these equations are sketched in Figure 10. The channel of the thruster is divided into four regions between the cusps for a three ring magnet system. In these regions, constant local properties such as electron temperature T , potential Φ , and ionization I are assumed. A constant current of electrons j_e and the probability for electrons to impinge on the wall pc are assumed at the interfaces of these regions.

TABLE 2 Comparison of performance parameters between the MDO and the results based on the PIC simulation

	I_a (A)	T (mN)	η_t (%)	I_{sp} (s)
MDO	2.94	102.7	36.5	2131
PIC	2.66	62.8	15.2	1333

FIGURE 10 Schematic of a HEMP thruster with the most important quantities of the power balance model as found in Kornfeld et al.^[3] The dashed lines mark the cusp positions. je_i denotes the electron current, which increases closer to the anode because of ionization. The ionization current I_i , the electron temperature T_i and the potential Φ_i are given between the cusps



Using the anode voltage U_a , anode current I_a and an electron current from the neutralizer je_0 as input parameters one can solve for the remaining properties including the cusp arrival probabilities pc_i for electrons. The following equations are derived from the power balance equations for the different cusp arrival probabilities pc_i

$$pc_i = 1 - \frac{je_i - I_i}{je_{i+1}} \quad \text{for } i = 1, 2, 3. \quad (4)$$

These are the probabilities of electrons reaching the dielectric at the cusp by comparing the incoming and outgoing electron current je_i and je_{i+1} and considering the ionization current I_i as an additional electron source. These currents can be directly extracted from the PIC results by integrating electron currents and ionization rates in each region. From the PIC results the cusp arrival probabilities can be calculated and are listed in Table 3.

Of particular importance in the power balance model are empirical estimates for the global energy transfers in the system. They are given by the relative proportion of the gained electron power transferred to excitation CE and the proportions for ionization CI and thermalization CT . These transfer parameters again can be calculated self-consistently using the PIC results. From the power balance model one obtains

$$CE_i = 1 - \frac{(je_{i-1}(1 - pc_i) + I_i)T_i + I_iIE}{je_{i-1}(1 - pc_i)(\Phi_i - \Phi_{i-1} + T_{i-1})}, \quad (5)$$

$$CT_i = \frac{T_i je_i}{je_{i-1}(1 - pc_i)(\Phi_i - \Phi_{i-1} + T_{i-1})}, \quad (6)$$

$$CI_i = \frac{I_i IE}{je_{i-1}(1 - pc_i)(\Phi_i - \Phi_{i-1} + T_{i-1})}, \quad (7)$$

$$1 = CE_i + CT_i + CI_i, \quad (8)$$

for the relative energy transfer proportions, with the ionization energy of xenon $IE = 12.1$ eV and the parameters from Figure 10. These coefficients represent the fractions of the total electron energy loss. CT is the ratio of the electron heat flux in one cell compared to the incoming total electron energy into the cell. CI is the ratio of electron energy transferred into ionization processes by multiplying the ionization number with the ionization energy. At last CE is considered as the rest of the energy losses of the electrons, coming from the excitation collisions with neutrals. For easier comparison the different proportions are summed up over the areas of the thruster and then averaged, as only global energy transfer coefficients are assumed in the MDO. The results for the proportions and calculated cusp arrival probabilities are given in Table 3.

The results in Table 3 show a significant difference in cusp arrival probabilities and in the energy transfer coefficients between the MDO input parameters^[3] and the PIC simulations. The power transfer to excitation CE and ionization CI was overestimated in the MDO, whereas the thermalization CT was underestimated. The calculated cusp arrival probabilities, especially of the

TABLE 3 Comparison of the input parameters between the MDO and self-consistently calculated coefficients based on PIC simulation

Case	CE	CI	CT	pc_1	pc_2	pc_3	pc_4
MDO	0.25	0.07	0.68	0.06	0.119	0.160	0.254
PIC	0.40	0.18	0.42	0.23	0.56	0.07	0.014

exit and the first cusps, are four to five times higher than in the empirical data while the arrival probability at the anode cusp is significantly lower. These differences can be explained by the different assumptions made for the S_1 thruster in comparison to the considered thrusters used for the original 0D power balance model. There, the anode current was fixed at $I_a = 1$ A, because no ionization cross sections and no neutral gas flow assumptions were made in the model. However, the resulting anode current of the MDO is three times higher, which extrapolated the model outside its validation range. As already discussed, the operating state, defined by the anode current, strongly influences the solution of the thruster. This changes the values of the cusp arrival probabilities and transfer coefficients.

The strong axial electric field at the exit accelerates the electrons towards the thruster channel up to anode potential. The electric fields and the magnetic field lines are nearly parallel at the exit leading to a strong magnetization of the electrons. Because of the low plasma and neutral density there, the electrons follow the magnetic field mostly undisturbed. The high parallel velocity of the electrons to the magnetic field leads to a higher probability of reaching the wall at the exit cusp pc_1 and the first cusp in the channel pc_2 . These cusp arrival probabilities reflect the discussion of the plasma properties from above.

In the process of this work, PIC simulations were carried out for different points of operation with constant anode voltage of 1000 V and mass flow rate of 50 sccm by varying the neutralizer and consequently the anode current. The transfer coefficients (CE, CI, and CT) from PIC simulations show little variations for different anode currents, which implies that the energy transfer coefficients can be considered nearly constant for one thruster design and different anode currents (Table A1).

Table 3 indicates that the excitation and ionization energy transfer coefficients were underestimated in the MDO model, while the thermalization was overestimated. Taking into account the higher probability of hot electrons reaching the channel wall, as the higher cusp arrival probabilities imply, it follows immediately that the coefficient of energy transfer to thermalization CT of the PIC simulation is lower.

The model from Kornfeld et al.^[3] does not account for the influence of neutral gas density distribution, ionization efficiency, doubly charged ions or the details of the ion beam structure and assumes constant temperature in the considered cells. Nonetheless the 0D power balance model is a robust tool, which usefully enabled the MDO, resulting in a working HEMP-T design. The present study suggests that the approach is valid within one design where interpolation can be used across existing operational points, but it becomes inaccurate for different designs or in extrapolation mode, which therefore needs independent assessment.

4 | CONCLUSIONS AND OUTLOOK

In this work an optimized thruster design, the S_1 thruster derived by the MDO, was investigated using the PIC method. The results of the simulation were discussed and it was found that the S_1 thruster is characterized by comparable physical properties to other HEMP-Ts. With the charged particle distributions the performance parameters were calculated and compared to the predictions of the MDO, revealing considerable difference. To understand the deviation between PIC and the MDO, the fully kinetic results from PIC were used to investigate the 0D power balance model, used in the MDO. Substantial difference was found in the energy transfer properties and cusp arrival properties. Using the new physical parameters obtained with PIC, the MDO results could be improved. Further, new strategies and parameters for optimization were proposed. The results from this enhancement will be published in the future. This collaboration between PIC and the MDO paves the way for design optimization, combining optimization algorithms and fully kinetic models in conjunction with surrogate modelling.

ACKNOWLEDGMENTS

The work of P.M. and D.K. was funded by the German Space Agency DLR through Project 50RS1510. The work of S.H.Y. was supported by the Australian Government Research Training Program (RTP) Scholarship. The authors are thankful to Angus Muffatti and Thomas Fahey for the original development of the optimization process chain incorporating the performance analysis and magnetic field simulation.

ORCID

Paul Matthias  <https://orcid.org/0000-0002-5968-6647>

REFERENCES

- [1] G. Kornfeld, N. Koch, G. Coustou, in *28th IEPC Electric Rocket Propulsion Society*, Toulouse, France **2003**, 1–18.

- [2] N. Koch, M. Schirra, S. Weis, A. Lazurenko, B. van Reijen, J. Haderspeck, A. Genovese, P. Holtmann, R. Schneider, K. Matyash, O. Kalentev, in *32nd IEPC*, Electric Rocket Propulsion Society, Wiesbaden, Germany **2011**, 1–8.
- [3] G. Kornfeld, N. Koch, H. Harmann, in *30th IEPC*, Vol. 108, Electric Rocket Propulsion Society, Florence, Italy **2007**, 17–20.
- [4] A. Keller, P. Köhler, F.G. Hey, M. Berger, C. Braxmaier, D. Feili, D. Weise, U. Johann, in *33rd IEPC*, IEEE, Washington, DC **2013**, 45–53.
- [5] R. Allen, D. Lee, D. Klyde, G. Howe, J. P. Christos, T. Rosenthal, in *1st Hum. Center. Transport. Simul. Conf.*, Iowa-City, IA **2001**, 1–14.
- [6] D. E. Smith, J. O. M. Starkey, *Veh. Syst. Dyn.* **1995**, *24*(2), 163.
- [7] D. Kahnfeld, R. Schneider, F. Cichocki, M. Merino, E. Ahedo, J. Duras, N. Koch, in *35th IEPC*, Electric Rocket Propulsion Society, Atlanta, Georgia **2017**, 1–10.
- [8] J. Duras, D. Kahnfeld, G. Bandelow, S. Kemnitz, K. Lüsow, P. Matthias, N. Koch, R. Schneider, *J. Plasma Phys.* **2017**, *83*, 595830107.
- [9] P. Matthias, R. Schneider, R. Heidemann, F. Holtmann, D. Kahnfeld, K.-F. Lüsow, in *35th IEPC*, Electric Rocket Propulsion Society, Atlanta, Georgia **2017**, 1–8.
- [10] T. Fahey, A. Muffatti, H. Ogawa, *Aerospace*. **2017**, *2017*(4), 55.
- [11] O. Kalentev, K. Matyash, J. Duras, K.-F. Lüsow, R. Schneider, N. Koch, M. Schirra, *Contrib. Plasma Phys.* **2014**, *54*(2), 235.
- [12] C. K. Birdsall, A. B. Langdon, *Plasma Physics via Computer Simulation*, CRC Press, Boca Raton, Florida **2004**.
- [13] K. Matyash, O. Kalentev, R. Schneider, F. Taccogna, N. Koch, M. Schirra, in *31st IEPC*, Vol. 110, Electric Rocket Propulsion Society, Ann Arbor, MI **2009**, 20–24.
- [14] D. Tskhakaya, K. Matyash, R. Schneider, F. Taccogna, *Contrib. Plasma Phys.* **2007**, *47*(8–9), 563.
- [15] C. K. Birdsall, D. Fuss, *J. Comput. Phys.* **1969**, *3*(4), 494.
- [16] S. Li Xiayoe, J.R. Gilbert, J.W. Demmel **1999**. https://crd-legacy.lbl.gov/~xiaoye/SuperLU/superlu_ug.pdf.
- [17] J. P. Boris, in *Proc. Fourth Conf. Numer. Simul. Plasmas*, **1970**.
- [18] C. K. Birdsall, N. Maron, *J. Comput. Phys.* **1980**, *36*(1), 1.
- [19] R. Courant, H. Lewy, K. Friedrichs, *Math. Ann.* **1928**, *100*, 32–74.
- [20] D. Kahnfeld, J. Duras, P. Matthias, S. Kemnitz, P. Arlinghaus, G. Bandelow, K. Matyash, N. Koch, R. Schneider, in *t.b.p.*, **2019**.
- [21] F. Taccogna, S. Longo, M. Capitelli, R. Schneider, *Phys. Plasmas* **2005**, *12*(5), 053502.
- [22] J. Lacina, *Plasma Phys.* **1971**, *13*(4), 303.
- [23] P. Matthias, D. Kahnfeld, S. Kemnitz, J. Duras, N. Koch, R. Schneider, Similarity scaling - application and limits for High-Efficiency-Multistage-Plasma-Thruster PIC modeling, IOP Publishing **2019**.
- [24] M. Hayashi, in *NIFS-DATA-79*, NIFS, **2003**. <http://www.nifs.ac.jp/report/NIFS-DATA-079.pdf> (accessed: October 2018).
- [25] D. Kahnfeld, R. Heidemann, J. Duras, P. Matthias, G. Bandelow, K. Lüsow, S. Kemnitz, K. Matyash, R. Schneider, *Plasma Sourc. Sci. Technol.* **2018**, *27*(12), 124002.
- [26] D. M. Goebel, I. Katz, *Fundamentals of Electric Propulsion: Ion and Hall Thrusters, of JPL Space Science and Technology Series*, Wiley, Hoboken, New Jersey **2008**.

How to cite this article: Matthias P, Kahnfeld D, Schneider R, Yeo SH, Ogawa H. Particle-in-cell simulation of an optimized high-efficiency multistage plasma thruster. *Contributions to Plasma Physics*. 2019;59:e201900028. <https://doi.org/10.1002/ctpp.201900028>

APPENDIX: A POWER BALANCE MODEL COEFFICIENTS AT DIFFERENT OPERATION STATES

TABLE A1 Comparison of the input parameters between the MDO and self-consistently calculated coefficients based on the PIC simulation at different points of operation

Case	CE	CI	CT	pc_1	pc_2	pc_3	pc_4
MDO	0.25	0.07	0.68	0.06	0.119	0.160	0.254
200 mA	0.37	0.23	0.40	0.28	0.54	0.10	0.010
300 mA	0.33	0.22	0.45	0.31	0.64	0.10	0.010
400 mA	0.37	0.18	0.45	0.32	0.44	0.09	0.015
500 mA	0.33	0.20	0.47	0.31	0.50	0.09	0.013
600 mA	0.37	0.21	0.43	0.32	0.56	0.10	0.015
700 mA	0.39	0.18	0.43	0.21	0.50	0.09	0.012
800 mA	0.40	0.18	0.42	0.23	0.56	0.07	0.014

9 Erklärung

Hiermit erkläre ich, dass diese Arbeit bisher von mir weder an der Mathematisch - Naturwissenschaftlichen Fakultät der Ernst-Moritz-Arndt-Universität Greifswald noch einer anderen wissenschaftlichen Einrichtung zum Zwecke der Promotion eingereicht wurde. Ferner erkläre ich, dass ich diese Arbeit selbständig verfasst und keine anderen als die darin angegebenen Hilfsmittel und Hilfen benutzt und keine Textabschnitte eines Dritten ohne Kennzeichnung übernommen habe.

(Paul Matthias)

Greifswald, _____, 2021

10 Curriculum vitae

Personal Information

Name	Paul Matthias
Address	Eppendorfer Weg 104, 20259 Hamburg, Germany
Telephone	49 +(0)176 / 55 98 89 24
E-Mail	pau.matthias@gmx.de
Nationality	German
Date and place of birth	15.05.1990, Greifswald, Germany

Professional experience

01.08.2019 – current	Software Developer CGI, Hamburg Project: Simlab
01.04.2016 – 31.5.2019	Wissenschaftlicher Mitarbeiter Ernst-Moritz-Arndt Universität Greifswald, Germany Project: PIC Simulation of satellite thrusters

Education

- 01.04.2016 – current PhD student
Ernst-Moritz-Arndt Universität Greifswald, Germany
Supervisor Prof. Dr. Ralf Schneider
- 01.10.2013 – 30.09.2015 Degree: **Master of Science in Physics**
Ernst-Moritz-Arndt Universität Greifswald, Greifswald, Germany
Thesis: “PIC simulations of capacitively coupled oxygen rf discharges”
supervisor Prof. Dr. Ralf Schneider
- 01.10.2010 – 30.09.2013 Degree: **Bachelor of Science in Physics**
Ernst-Moritz-Arndt Universität Greifswald, Greifswald, Germany
Thesis: “Quantenkavitäten nahe der Resonanz”
supervisor Dr. Andreas Alvermann
- 01.08.2001 – 04.06.2009 Degree: **Allgemeine Hochschulreife**
Gymnasium Schenefeld, Schenefeld, Germany

Scientific Contributions

Reviewed publications

- D. Kahnfeld, J. Duras, P. Matthias, *et al.*, “Numerical modeling of high efficiency multistage plasma thrusters for space applications”, *Reviews of Modern Plasma Physics*, vol. 3, no. 1, 2019
- P. Matthias, G. Bandelow, K. Matyash, *et al.*, “Pic simulations of capacitively coupled oxygen rf discharges”, *The European Physical Journal D*, vol. 72, no. 5, p. 86, May 2018, ISSN: 1434-6079. [Online]. Available: <https://doi.org/10.1140/epjd/e2017-80565-y>
- D. Kahnfeld, R. Heidemann, J. Duras, *et al.*, “Breathing modes in HEMP thrusters”, *Plasma Sources Science and Technology*, vol. 27, no. 12, p. 124002, Dec. 2018. DOI: 10.1088/1361-6595/aaf29a. [Online]. Available: <https://doi.org/10.1088/1361-6595/aaf29a>
- J. Duras, D. Kahnfeld, G. Bandelow, *et al.*, “Ion angular distribution simulation of the highly efficient multistage plasma thruster”, *Journal of Plasma Physics*, vol. 83, 2017. DOI: {10.1017/S0022377817000125}
- P. Matthias, D. Kahnfeld, R. Schneider, *et al.*, “Particle-in-cell simulation of an optimized high-efficiency multistage plasma thruster”, *Contributions to Plasma Physics*, vol. 59, no. 9, e201900028, DOI: 10.1002/ctpp.201900028. [Online]. Available: <https://onlinelibrary.wiley.com/doi/abs/10.1002/ctpp.201900028>
- S. Yeo, T. Fahey, H. Ogawa, *et al.*, “Multi-objective optimization and particle-in-cell simulation of cusped field thruster for micro-satellites platform”, *AIAA*, 2019
- P. Matthias, D. Kahnfeld, S. Kemnitz, *et al.*, “Similarity scaling-application and limits for high-efficiency-multistage-plasma-thruster particle-in-cell modelling”, *Contributions to Plasma Physics*, vol. n/a, no. n/a, e201900199, DOI: 10.1002/ctpp.201900199. eprint: <https://onlinelibrary.wiley.com/doi/pdf/10.1002/ctpp.201900199>. [Online]. Available: <https://onlinelibrary.wiley.com/doi/abs/10.1002/ctpp.201900199>

Non-reviewed Conference proceedings

- P. Matthias, R. Schneider, R. Heidemann, *et al.*, “Influence of different anode voltages on the hempt”, *35th IEPC*, no. 310, Oct. 2017

Teaching Experience

- Sommersemester 2017 - Computerpraktikum für Umweltwissenschaftler
- Sommersemester 2018 - Computerpraktikum für Umweltwissenschaftler

(Paul Matthias)

Greifswald, _____, 2021

11 Acknowledgement

At the end I want to thank all the people, who helped me during the compilation of this thesis.

I want to express my gratitude to my supervisor Prof. Dr. Ralf Schneider for his great support throughout this whole journey. Without him, this thesis might only be an idea, far from ever seeing the light of the world.

Furthermore, I want to thank all members of the CompuS, especially Dani, my companion on this long and challenging, but also rewarding, trip. We have been together from the beginning and in the end, we both were finally able to finish (and looking at others, this is quite an achievement ;)).

I also want to thank the German Space Agency whose funding allowed me to work on this interesting topic and brought me to some great places at international conferences.

I like to thank my parents for their endless trust and support during my whole study time. Last but not least I want to thank my former girlfriend (now caring wife and mother of my lovely first child) Tabea. You have kicked my ass for the last two years to finish what I started and without this encouragement, who knows if I would have had the power to push through.

There are of course a lot more people involved, which deserve their individual thanks. So, representative at this point: Thank you! Yes, I am pointing my finger at you. You and all of the people who will ever make it this far into my thesis.